



CENTER FOR INFRASTRUCTURE ENGINEERING STUDIES

STRENGTHENING OF RC STRUCTURES WITH NEAR SURFACE MOUNTED FRP RODS

by

Laura De Lorenzis

Antonio Nanni

University of Missouri-Rolla

**CIES
99-10**

Disclaimer

The contents of this report reflect the views of the author(s), who are responsible for the facts and the accuracy of information presented herein. This document is disseminated under the sponsorship of the Center for Infrastructure Engineering Studies (CIES), University of Missouri -Rolla, in the interest of information exchange. CIES assumes no liability for the contents or use thereof.

The mission of CIES is to provide leadership in research and education for solving society's problems affecting the nation's infrastructure systems. CIES is the primary conduit for communication among those on the UMR campus interested in infrastructure studies and provides coordination for collaborative efforts. CIES activities include interdisciplinary research and development with projects tailored to address needs of federal agencies, state agencies, and private industry as well as technology transfer and continuing/distance education to the engineering community and industry.

Center for Infrastructure Engineering Studies (CIES)

University of Missouri-Rolla
223 Engineering Research Lab
1870 Miner Circle
Rolla, MO 65409-0710
Tel: (573) 341-6223; fax -6215
E-mail: cies@umr.edu
www.umr.edu/~cies

ABSTRACT

The use of Fiber Reinforced Polymer (FRP) materials has proved to be one of the most exciting and effective technologies for external strengthening of reinforced concrete (RC) and masonry structures. In this context, Near Surface Mounted (NSM) FRP rods are now emerging as a promising technique in addition to externally bonded FRP laminates. Embedment of the rods is achieved by grooving the surface of the member and placing the rods in the epoxy-filled grooves.

The overall objective of this research project was to investigate the effectiveness of NSM FRP rods as a strengthening system for RC and masonry structures. The research protocol started from the characterization of the tensile properties of the FRP rods (material level). Then, the mechanics of the bond of NSM FRP rods embedded in concrete and concrete masonry units was experimentally investigated by using coupon-size specimens (sub-system level). Finally, testing of eight full-size RC beams strengthened in shear with this technique was performed (structural member level). Results showed that NSM FRP rods can significantly increase the shear capacity of RC members. A simple shear design approach was developed and, when applied to the tested beams, appeared to give a reasonable and conservative estimate of the ultimate load.

ACKNOWLEDGEMENTS

This project was funded by the National Science Foundation (NSF) under grant No. EEC9905711 and the member corporations of the NSF Industry/University Cooperative Research Center on Repair of Building and Bridges with Composites.

TABLE OF CONTENTS

	Page
ABSTRACT	iv
ACKNOWLEDGEMENTS	v
LIST OF FIGURES	x
LIST OF TABLES	xv
SECTION	
1. INTRODUCTION AND BACKGROUND	1
1.1. STRENGTHENING OF STRUCTURES WITH FRP LAMINATES	1
1.2. NEAR SURFACE MOUNTED FRP RODS	1
1.3. PREVIOUS WORK ON NSM FRP RODS	3
1.3.1. Laboratory Projects	3
1.3.2. Field Projects.....	5
1.4. OBJECTIVES	11
1.5. DOCUMENT LAYOUT.....	12
2. MATERIALS USED IN THE EXPERIMENTAL PROGRAM.....	13
2.1. INTRODUCTION.....	13
2.2. CONCRETE.....	13
2.3. REINFORCING STEEL.....	14
2.4. FRP RODS	15
2.4.1. CFRP Deformed Rods.....	15
2.4.1.1. Specimens for Tensile Testing	15
2.4.1.2. Tensile Test Procedure	17
2.4.1.3. Tensile Test Results.....	18
2.4.2. GFRP Deformed Rods	19
2.4.3. CFRP Smooth Rods	20
2.5. EPOXY PASTE	20
2.6. CONCRETE BLOCKS.....	21
3. BOND OF NSM FRP RODS IN CONCRETE	22
3.1. INTRODUCTION.....	22

3.1.1. Background and Problem Statement	22
3.1.2. Objective	23
3.2. DESCRIPTION OF THE SPECIMENS	23
3.3. SPECIMEN PREPARATION.....	27
3.3.1. Cutting of the Groove.....	27
3.3.2. Choice of the Position of the Bonded Length.....	28
3.3.3. Application of Strain Gages	28
3.3.4. Application of the NSM Rod	31
3.4. TEST PROCEDURE.....	31
3.5. EXPERIMENTAL RESULTS FOR SPECIMENS WITH GFRP No. 4	
DEFORMED RODS	33
3.5.1. Introduction.....	33
3.5.2. General Results	34
3.5.3. Failure Modes.....	35
3.5.4. Free-End Slip Data.....	38
3.5.5. Strain Data	41
3.6. EXPERIMENTAL RESULTS FOR SPECIMENS WITH CFRP No. 3	
DEFORMED RODS	42
3.6.1. Introduction.....	43
3.6.2. General Results	44
3.6.3. Failure Modes.....	44
3.6.4. Free-End Slip Data.....	46
3.6.5. Strain Data	47
3.7. EXPERIMENTAL RESULTS FOR SPECIMENS WITH CFRP	
SANDBLASTED RODS	48
3.7.1. Introduction.....	48
3.7.2. General Results	4
3.7.3. Failure Modes.....	52
3.7.4. Free-End Slip Data.....	53
3.7.5. Strain Data	54
3.8. DISCUSSION OF TEST RESULTS	55
3.8.1. Failure Modes.....	55
3.8.2. Crack Pattern.....	56

3.8.3. Effect of the Surface Configuration.....	58
3.8.4. Effect of the Groove Size.....	58
3.8.5. Effect of the Bonded Length.....	59
3.9. CONCLUSIONS.....	61
4. BOND OF NSM FRP RODS IN MASONRY	63
4.1. INTRODUCTION.....	63
4.1.1. Background and Problem Statement.....	63
4.1.2. Objective	63
4.2. DESCRIPTION OF THE SPECIMENS	64
4.3. SPECIMEN PREPARATION.....	65
4.3.1. Application of Strain Gages	65
4.3.2. Cutting of the Grooves	66
4.3.3. Application of the Grout	67
4.3.4. Application of the NSM Rods.....	67
4.4. TEST PROCEDURE.....	67
4.5. EXPERIMENTAL RESULTS	70
4.5.1. General Results	70
4.5.2. Modes of Failure	71
4.5.3. Free-End Slip Data.....	72
4.5.4. Strain Data.....	73
4.6. DISCUSSION OF TEST RESULTS	75
4.7. CONCLUSIONS.....	75
5. SHEAR STRENGTHENING OF RC BEAMS WITH NSM FRP RODS	77
5.1. INTRODUCTION.....	77
5.1.1. Background and Problem Statement.....	77
5.1.2. Objective	78
5.2. DESCRIPTION OF THE SPECIMENS	78
5.3. SPECIMEN PREPARATION.....	80
5.3.1. Cutting of the Grooves	80
5.3.2. Application of Strain Gages	81
5.3.3. Application of the NSM Rods.....	81

5.4. TEST PROCEDURE.....	81
5.5. EXPERIMENTAL RESULTS	85
5.5.1. Beams Without Steel Stirrups	88
5.5.2. Beams With Steel Stirrups	97
5.6. DISCUSSION OF TEST RESULTS	101
5.7. PROPOSED DESIGN APPROACH	103
5.7.1. Background	105
5.7.2. Shear Strength of RC Beams Strengthened with FRP	106
5.7.3. Contribution of NSM FRP Rods to Shear Capacity.....	107
5.7.4. Calculation of V_{1F}	108
5.7.5. Calculation of V_{2F}	113
5.7.6. Summary of the Proposed Design Procedure.....	115
5.7.7. Comparison with the Experimental Results.....	115
5.8. CONCLUSIONS.....	116
6. CONCLUSIONS AND RECOMMENDATIONS FOR FURTHER RESEARCH.....	117
6.1. CONCLUSIONS.....	117
6.2. RECOMMENDATIONS FOR FURTHER RESEARCH	119
REFERENCES	120

LIST OF FIGURES

Figure	Page
1.1. NSM Rods	3
1.2. Vertical Grooves for Shear Strengthening with NSM FRP Rods (Hogue et al., 1999)	6
1.3. Grooves on the Surface of the Structure (Nanni, 1998)	6
1.4. Filling of Grooves with Epoxy Paste (Nanni, 1998)	7
1.5. Embedding CFRP Rods in the Top Surface of the Deck (Warren, 1998)	8
1.6. Installation of NSM CFRP Rods in the Bridge Deck (Alkhrdaji et al., 1999).....	9
1.7. Columns Strengthened with NSM Rods (Alkhrdaji et al., 1999).....	10
1.8. Installation of NSM FRP Rods on Masonry Walls (Tumialan et al., 1999).....	11
2.1. FRP Rods Used in the Experimental Program	16
2.2. Specimens of CFRP Deformed Rods Ready for Testing.....	17
2.3. Tensile Test Setup	17
2.4. Stress – Strain Relationship of CFRP No. 3 Deformed Rods.....	18
2.5. Tensile Failure of CFRP No. 3 Deformed Rods	19
2.6. Standard Concrete Blocks.....	22
3.1. Test Specimen.....	26
3.2. Free-Body Diagram	26
3.3. Position of the Strain Gages (Rods No. 3, Bonded Length 12 d_b).....	30
3.4. Position of the Strain Gages (Rods No. 3, Bonded Length 18 d_b).....	30
3.5. Position of the Strain Gages (Rods No. 3, Bonded Length 24 d_b).....	30
3.6. Position of the Strain Gages (Rods No. 4, Bonded Length 12 d_b).....	31
3.7. Position of the Strain Gages (Rods No. 4, Bonded Length 18 d_b).....	31
3.8. Position of the Strain Gages (Rods No. 4, Bonded Length 24 d_b).....	31
3.9. Specimens Before Preparation.....	32
3.10. Specimen Preparation.....	33
3.11. Test Setup	34
3.12. Load vs. Mid-Span Deflection for Specimen G4D12a (Failure by Epoxy Splitting)	36

3.13.	Specimen G4D12a After Failure	37
3.14.	Specimen G4D18a After Failure	38
3.15.	Specimen G4D12c After Failure	38
3.16.	Specimen G4D24c After Failure	39
3.17.	Pull-Out Load vs. Free-End Slip for Specimens G4D6a, G4D12a and G4D18a	40
3.18.	Average Bond Stress vs. Free-End Slip for Specimens G4D6a, G4D12a and G4D18a	41
3.19.	Average Bond Stress vs. Free-End Slip for Specimens G4D12a, G4D12b and G4D12c	41
3.20.	Pull-Out Load vs. Strain for Specimen G4D12c	42
3.21.	Strain vs. Location Diagram for Specimen G4D18a	43
3.22.	Load vs. Mid-Span Deflection for Specimen C3D12c (Failure by Concrete Cracking)	45
3.23.	Specimen C3D6a After Failure	46
3.24.	Specimen C3D18a After Failure	46
3.25.	Specimen C3D12b After Failure	47
3.26.	Specimen C3D24b After Failure	47
3.27.	Specimen C3D12c After Failure	48
3.28.	Average Bond Stress vs. Free-End Slip for Specimens C3D6a, C3D12a, C3D18a and C3D24b	48
3.29.	Average Bond Stress vs. Free-End Slip for Specimens C3D12a, C3D12b and C3D12c	49
3.30.	Strain vs. Location Diagram for Specimen C3D18a	49
3.31.	Load vs. Mid-Span Deflection for Specimen C3S12a (Failure by Pull-Out)	51
3.32.	Specimen C3S6a After Failure	52
3.33.	Specimen C4S6a After Failure	53
3.34.	Specimen C3S12a After Failure	53
3.35.	Specimen C3S18a After Failure	53
3.36.	Specimen C4S12a After Failure	54
3.37.	Specimen C4S18a After Failure	54
3.38.	Average Bond Stress vs. Free-End Slip for Specimens C3S6a, C3S12a, C3S18a and C3S24a	55

3.39.	Average Bond Stress vs. Free-End Slip for Specimens C3S12a, C3S12b and C3S12c	55
3.40.	Average Bond Stress vs. Free-End Slip for Specimens C4S6a, C4S12a, C4S18a and C4S24a	56
3.41.	Strain vs. Location Diagram for Specimen C4S12a	56
3.42.	Internal Cracks in Specimen C3S6a	59
3.43.	Crack Pattern in Specimen G4D24c After Failure	59
3.44.	Crack Pattern in Specimen C3D24b After Failure	60
4.1.	Position of the Strain Gages (Rods No. 3, Bonded Length 12 d_b).....	67
4.2.	Position of the Strain Gages (Rods No. 3, Bonded Length 18 d_b).....	68
4.3.	Cutting of the Grooves on the Concrete Blocks	68
4.4.	Concrete Blocks Before Preparation	69
4.5.	Specimen Preparation.....	70
4.6.	Scheme of the Test Setup	71
4.7.	Test Setup	71
4.8.	Detail of Hydraulic Jack and Pressure Transducer	72
4.9.	Detail of the LVDTs	72
4.10.	Specimen After Splitting Failure	74
4.11.	Specimen After Pull-Out Failure	74
4.12.	Average Bond Stress vs. Free-End Slip for Specimen GD6	75
4.13.	Pull-Out Load vs. Strain for Specimen GD12	76
4.14.	Strain vs. Location Diagram for Specimen GD12	76
5.1.	Cross-Section of the Beams	82
5.2.	Specimen Preparation.....	84
5.3.	Location of Strain Gages	85
5.4.	Test Setup	87
5.5.	Test Setup of Beam B90-7.....	87
5.6.	Failure of Beam BV	88
5.7.	Failure of Beam B90-7	89
5.8.	Crack Pattern of Beam B90-7.....	89
5.9.	Load vs. Strain Diagram of Beam B90-7	90
5.10.	Failure of Beam B90-5	91

5.11.	Crack Pattern of Beam B90-5.....	91
5.12.	Load vs. Strain Diagram of Beam B90-5	91
5.13.	Failure of Beam B90-5A	93
5.14.	Crack Pattern of Beam B90-5A.....	94
5.15.	Load vs. Strain Diagram of Beam B90-5A	94
5.16.	Failure of Beam B45-7	95
5.17.	Crack Pattern of Beam B45-7.....	95
5.18.	Load vs. Strain Diagram of Beam B45-7	95
5.19.	Failure of Beam B45-5	96
5.20.	Load vs. Mid-Span Deflection of the Beams Without Steel Stirrups	98
5.21.	Failure of Beam BSV.....	98
5.22.	Crack Pattern of Beam BSV	99
5.23.	Load vs. Strain Diagram of Beam BSV.....	100
5.24.	Failure of Beam BS90-7A	100
5.25.	Crack Pattern of Beam BS90-7A	101
5.26.	Load vs. Strain Diagram of Beam BS90-7A (Steel Stirrups).....	102
5.27.	Load vs. Strain Diagram of Beam BS90-7A (CFRP Rods).....	102
5.28.	Load vs. Mid-Span Deflection of the Beams With Steel Stirrups	103
5.29.	Case 1 ($\frac{d_{net}}{2} < s < d_{net}$).....	110
5.30.	Case 2 ($\frac{d_{net}}{3} < s < \frac{d_{net}}{2}$).....	110
5.31.	Case 3 ($\frac{d_{net}}{4} < s < \frac{d_{net}}{3}$).....	111
5.32.	Calculation of L_{totmin} for Case 1	111
5.33.	Calculation of L_{totmin} for Case 2	112
5.34.	Calculation of L_{totmin} for Case 3	113
5.35.	Comparison of Experimental and Theoretical V_{FRP}	117
5.36.	Comparison of Experimental and Theoretical V_n	118
A.1.	Test Region of the Specimen.....	125
A.2.	Region 1	126
A.3.	Region 3	126

A.4.	Internal Forces in the Generic Concrete Cross-Section (Region 3).....	128
A.5.	Stresses in the Concrete – Region 1 ($P = 5000$ lbs).....	129
A.6.	Stresses in the Concrete – Region 3 ($P = 5000$ lbs).....	130

LIST OF TABLES

Table	Page
2.1. Concrete Compressive Strength	14
2.2. Yield Strength of Reinforcing Steel in the Full-Size Beams	15
2.3. Results of Tensile Testing on CFRP No. 3 Deformed Rods	19
2.4. Properties of C-Bar (Marshall, 1998)	20
2.5. Properties of DFI Pultruded CFRP Rods (Warren, 1998)	20
2.6. Properties of Concreive Paste LPL (Master Builders, 1996)	21
3.1. Description of the Specimens	28
3.2. Position of the Bonded Length.....	29
3.3. Test Results for Specimens with GFRP No. 4 Deformed Rods	35
3.4. Test Results for Specimens with CFRP No. 3 Deformed Rods	44
3.5. Test Results for Specimens with CFRP Sandblasted Rods	51
4.1. Description of the Specimens	66
4.2. Test Results.....	73
5.1. Description of the Specimens	81
5.2. Summary of Test Results	97
5.3. Summary of Experimental and Theoretical Results	116

1. INTRODUCTION AND BACKGROUND

1.1. STRENGTHENING OF STRUCTURES WITH FRP LAMINATES

Strengthening of existing reinforced concrete (RC) and prestressed concrete (PC) structures may become necessary as a result of many possible factors, such as inadequate design or construction, deterioration due to corrosion of the embedded reinforcement, need for increase in structural capacity, and seismic retrofit. Aging and consequent deterioration of the infrastructure is nowadays a major challenge for the civil engineering community.

The use of Fiber Reinforced Polymer (FRP) materials for external strengthening of RC, PC, and masonry structures has emerged as one of the most exciting and promising technologies in materials and structural engineering (Nanni, 1993). The key properties that make these materials suitable for structural strengthening are excellent resistance to corrosion and high strength-to-weight ratio. As a result, their use in repair/rehabilitation can present many significant advantages with respect to the conventional methods.

Externally bonded FRP laminates have been successfully used to increase the flexural and/or the shear capacity (sometimes also the stiffness) of RC beams, to provide confinement to RC columns, to strengthen masonry walls subjected to out-of-plane as well as in-plane loading. A notable amount of experimental research has been carried out and is currently ongoing towards the characterization of RC and masonry structures strengthened with this technique (Dolan et al., 1999). At the same time, many successful installations have covered the industrial, commercial, and public markets all over the world (Thomas, 1998), so that strengthening with externally bonded FRP laminates can be considered close to achieve the status of mainstream technology.

1.2. NEAR-SURFACE MOUNTED FRP RODS

A new FRP-based strengthening technique is now emerging as a valid alternative to externally bonded FRP laminates. From this point forward, it will be referred to as Near-Surface Mounted (NSM) FRP rods. Embedment of the rods is achieved by grooving the surface of the member to be strengthened along the desired direction. The groove is filled half-way with epoxy paste, the FRP rod is then placed in the groove and lightly pressed, so forcing the paste to flow

around the bar and fill completely between the bar and the sides of the groove. The groove is then filled with more paste and the surface is leveled. Details of the final product are shown in Figure 1.1.

Although the use of FRP rods for this application is very recent, NSM steel rods have been used in Europe for strengthening of RC structures since the early 50's. The earliest reference that could be found in the literature dates back to 1949 (Asplund, 1949). In 1948, an RC bridge in Sweden experienced an excessive settlement of the negative moment reinforcement during construction, so that the negative moment capacity needed to be increased. This was accomplished by grooving the surface, filling the grooves with cement mortar and embedding steel rebars in them. Since no previous experience was available, different possible ways to obtain the grooves were examined in order to choose the most convenient one. All the technological and design problems and considerations are reported in (Asplund, 1949).

Nowadays, FRP rods can be used in place of steel and epoxy paste can replace cement mortar. The advantage is primarily the resistance of FRP to corrosion. This property is particularly important in this case due to the position of the rods very close to the surface, which exposes them to the environmental attacks.

The use of NSM FRP rods is an attractive method for increasing the flexural and the shear strength of deficient RC members and masonry walls and, in certain cases, can be more convenient than using FRP laminates. Application of NSM FRP rods does not require surface preparation work (other than grooving) and requires minimal installation time compared to FRP laminates. Another advantage is the feasibility of anchoring these rods into members adjacent to the one to be strengthened. Furthermore, this technique becomes particularly attractive for strengthening in the negative moment regions of slabs and decks, where external reinforcement would be subjected to mechanical and environmental damage and would require protective cover which could interfere with the presence of floor finishes.

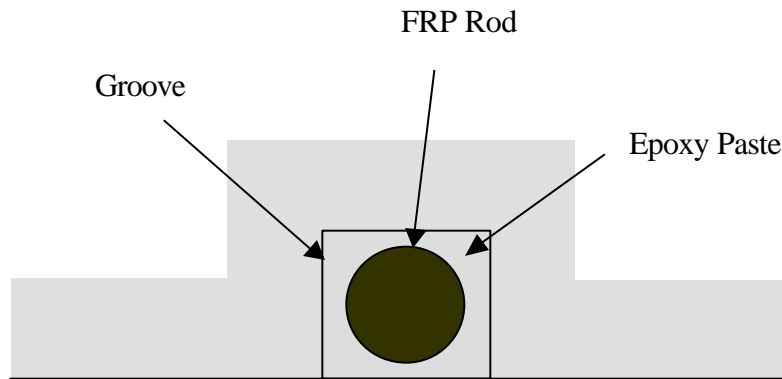


Figure 1.1. NSM Rods

1.3. PREVIOUS WORK ON NSM FRP RODS

Very limited literature is currently available on NSM FRP rods. Although only a few experimental studies are documented to date, some significant field applications of this technique have already been carried out in the United States during the past two years. Laboratory studies and field projects will be outlined in the following.

It is worth mentioning that what is herein called "NSM rods" has been given different names in the previous literature, such as "grouted reinforcement" (Asplund, 1949), or "embedded reinforcement" (Warren, 1998).

1.3.1. Laboratory Projects. Experimental data on the bond between Carbon FRP (CFRP) rods and epoxy paste is reported in the Navy Special Publication SP-2046-SHR (Warren, 1998). Direct pull-out tests were conducted using smooth CFRP rods No. 3 (nominal diameter 3/8 in.) manufactured by DFI Pultruded Composites, Inc. embedded in two different types of Sika epoxies. The surface of some of the rods was slightly sanded to improve the bond characteristics. The rods were embedded 4 in. (corresponding to 11 times the diameter) in an epoxy-filled pipe with a diameter of 2 in. The test parameters were surface condition of the rods, type of epoxy and addition of sand to extend the epoxy volume. Failure occurred at the rod-epoxy interface (pull-out). The ultimate load and, therefore, the average bond strength over the 4-in. embedment was reported. The maximum average bond strength was obtained using sanded rods embedded in Sika 32 epoxy with

no sand, manufactured by Sika. The addition of sand was found to provide less variation in test results but also to slightly reduce the bond strength and the watability of the epoxy.

Yan et al. (1999) performed experimental tests to characterize the bond strength of NSM FRP rods. The specimen used for this test consisted of two concrete blocks, two CFRP bars, and epoxy paste. The concrete strength was 5000 psi. The smooth CFRP rods had a diameter of 7/16 in. and were sandblasted prior to the test to improve the bond characteristics. The epoxy paste used was Concrete Paste LPL by Master Builders Technologies. The specimens differed for the value of the bonded length, which was equal to 2 in. (4.6 diameters), 4 in. (9.2 diameters) and 6 in. (13.7 diameters). The specimens were prepared by filling the grooves with the epoxy paste and then placing the rods in the paste. The paste was allowed to cure for 14 days at room temperature before testing. The type of test performed was direct pull-out of the NSM FRP rods. Two types of failure mode occurred: the specimens with the two shorter bonded lengths failed by rupture of the concrete at the edge of the block, those with the 6-in. bonded length experienced failure at the rod-epoxy interface (pull-out). Load at onset of slip, ultimate load and free-end slip at ultimate were recorded.

Crasto et al. (1999) conducted experimental research on flexural strengthening of RC beams with NSM FRP rods. The materials used were CFRP rods manufactured by DFI Pultruded Composites, Inc. and a two-part epoxy by Dexter Hysol, Inc. The experimental program included the evaluation of the technique on 8.5-ft. RC beams, the scale-up to full-size (28-ft.) beams and the final application to deteriorated 34-ft. RC beams removed from a vehicular bridge after more than 80 years of service.

A number of tests was conducted on beams with varying ratios of steel/composite cross-sectional area. Rectangular grooves were machined into the tensile face of the beams to various depths, cleaned and dried. The CFRP rods were sanded, wiped clean with acetone and embedded in the epoxy within the grooves. The adhesive was then allowed to cure overnight under ambient conditions before the beams were tested under four-point bending.

All tests showed that the NSM composite reinforcement improved the flexural stiffness, the value of bending moment at which the steel yields and the ultimate moment of the beams. Performance of the 8.5-ft. beams was compared with that of identical beams strengthened with an

equivalent amount of externally bonded FRP laminates and tested as part of a previous experimental program. While the ultimate moment was very close, the failure modes were different. Failure initiated in both cases with compression crushing of the concrete. In the plate-reinforced beam, however, secondary, catastrophic failure occurred almost instantaneously through composite fracture or composite/composite lap failure. In the rod-reinforced beam, secondary failure was non-catastrophic, with limited debonding and partial fracture of the embedded rods, allowing the beam to sustain the applied load with gradual deformation up to the limits of the test fixture. Similar results were obtained from testing of the longer beams.

1.3.2. Field Projects. A strengthening project was carried out at the structural street level floor of Myriad Convention Center, Oklahoma City, OK (USA) in 1997-1998 (Hogue et al., 1999). The PC floor required strengthening in order to increase its live load bearing capacity. The strengthening system implemented included a combination of externally bonded steel plates, CFRP sheets and NSM CFRP rods. The strengthening system sought to address both flexural and shear deficiencies. NSM rods were used in this case for shear strengthening of one of the RC joists. Vertical grooves 1/2-in. wide and 3/4-in. deep with a total length of 20 in. were saw-cut along the side surfaces of the joist at such positions that existing stirrups were avoided (Figure 1.2). CFRP No. 3 rods were then inserted in the epoxy-filled grooves.

NSM CFRP rods were used for strengthening of two RC circular structures in the United States in 1998 (Nanni, 1998). Longitudinal and transverse grooves 1/2-in. wide and 1/2-in. deep were cut on the surface of the structures (Figure 1.3) and CFRP sandblasted rods with a nominal diameter of 5/16 in. were embedded in the epoxy-filled grooves (Figure 1.4).



Figure 1.2. Vertical Grooves for Shear Strengthening with NSM FRP Rods (Hogue et al., 1999)



Figure 1.3. Grooves on the Surface of the Structure (Nanni, 1998)

Pier 12 at the Naval Station San Diego, CA (USA) was strengthened in November 1998 to meet demand of operational changes accompanied by higher vertical loads (Warren, 1998). NSM CFRP rods were used to increase the capacity of the deck slab in the negative moment regions. The surface area was primed with penetrating epoxy sealer/primer and allowed to cure overnight. Slots were saw-cut in the deck in the range of 7/8-in. deep and 5/8-in. to 3/4-in. wide. The slots were

abrasive blasted to roughen the surface, air blasted to clean the concrete and primed before filling with epoxy encapsulate. Carbon pultruded No. 3 rods were placed in sequence into the epoxy-filled slots and pressed to the bottom (Figure 1.5). The slots were then filled up to within $\frac{1}{4}$ in. of the original concrete surface. After the epoxy was cured, the surface was abrasive blasted and a UV protective layer was added to the top of the slot. The surface was ready for use 24 hours after the installation.

After completion of the upgrade, some spans of the deck were tested using simulated outrigger loads. Strain gages attached to the CFRP rods allowed to monitor the performance of the strengthening system, which proved to be satisfactory. Half-scale tests of the upgrade systems were also conducted. RC slabs strengthened with NSM CFRP rods were tested under three-point bending. The strengthened slabs exhibited significant gains in strength and ductility over the baseline slab, the failure mode being punching shear. Prior to ultimate load, some rods had begun to separate from the slab surface. There were no rod failures prior to ultimate load.



Figure 1.4. Filling of Grooves with Epoxy Paste (Nanni, 1998)



Figure 1.5. Embedding CFRP Rods in the Top Surface of the Deck (Warren, 1998)

Bridge J-857 was located on Route 72 in Phelps County, MO (USA). It consisted of three solid RC decks simply supported by two bents. Each bent consisted of two piers connected at the top by an RC cap beam. Due to the realignment of Route 72, the bridge was decommissioned and scheduled for demolition. Therefore, it presented an excellent opportunity for in-situ testing to failure after strengthening with FRP composites (Alkhrdaji et al., 1999).

The bridge was strengthened in August of 1998 while in service. Two of the three decks were strengthened using two different FRP systems, namely, externally bonded FRP laminates and NSM FRP rods, while the third deck was left as a benchmark. The NSM reinforcement consisted of CFRP rods with 7/16-in. diameter and surface roughened by sandblasting to improve bond properties. Strengthening to approximately 30% of the nominal moment capacity was desirable to upgrade the bridge decks for HS20-modified truck loading. The design called for 20 NSM CFRP rods spaced at 15 in. on-center. The rods were embedded in 20-ft long, 3/4-in. deep, and 9/16-in. wide grooves cut onto the soffit of the bridge deck parallel to its longitudinal axis, as illustrated in Figure 1.6. The grooves were sand blasted to remove dust and any loose materials that could interfere with the bond between epoxy paste and concrete. Strain gages and fiber optics sensors

were applied to concrete, steel reinforcement and FRP reinforcement to monitor strain during testing.

Each of the three decks was tested to failure by applying quasi-static load cycles. For the deck with NSM rods, failure was initiated by the rupture of some CFRP rods at the location of the widest crack. This deck exhibited the highest capacity with a failure load of 596 kips, corresponding to an increase in the moment capacity of 27% over the unstrengthened deck. At service levels (i.e., before yielding of the steel reinforcement), both decks strengthened with FRP composites exhibited higher stiffness than the unstrengthened control deck.

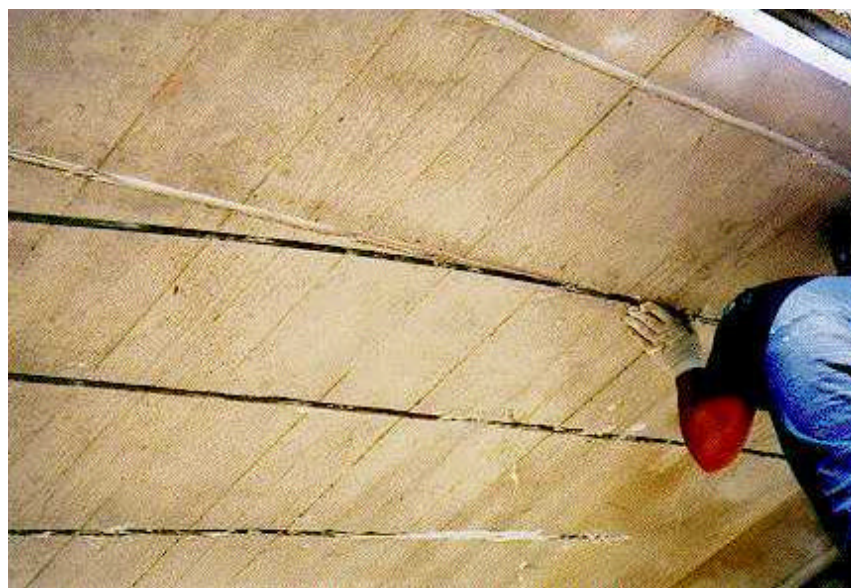


Figure 1.6. Installation of NSM CFRP Rods in the Bridge Deck (Alkhrdaji et al., 1999)

Two columns were also strengthened with NSM CFRP rods to increase their flexural capacity (Figure 1.7). The intended levels of flexural strengthening were such that two different failure modes would be achieved, one controlled by rupture of the CFRP reinforcement (6 rods, 3 on each face of the column) and one by crushing of concrete (14 rods, 7 on each face of the column). The rods were mounted on two opposite faces of the columns and fully anchored (minimum 15 in.) into the footings to ensure that the full capacity of the strengthened section would

be attained at the base of the column. The grooves and the drilled holes were filled with a viscous epoxy grout.



Figure 1.7. Columns Strengthened with NSM Rods (Alkhrdaji et al., 1999)

A strengthening and load-testing program at the decommissioned Malcolm Bliss Hospital in St. Louis, MO (USA) was conducted in 1999 (Tumialan et al., 1999). The building, a five-story RC-frame addition built in 1964, offered a unique opportunity for performing in-situ experimentation. Static load tests up to failure were carried out in order to validate strengthening of masonry walls and RC joists using externally bonded FRP laminates and NSM FRP rods.

The program on masonry walls strengthened with FRP composites included testing of unreinforced masonry walls subjected to out-of-plane loading and reinforced masonry walls under in-plane loading. Parameters such as the type of composite system, strip width, and FRP installation methods were evaluated. Figure 1.8 shows the installation of NSM FRP rods on a masonry wall to be strengthened for out-of-plane loading.



**Figure 1.8. Installation of NSM FRP Rods on Masonry Walls
(Tumialan et al., 1999)**

1.4. OBJECTIVES

As the technology of NSM FRP rods emerges, a complete investigation on the structural behavior of RC and masonry members externally strengthened with this technique is needed. In order to achieve a comprehensive understanding of the structural behavior, the research protocol should start from the characterization of the material properties, investigate the mechanics of the strengthening system and finally analyze the performance of the structural members.

The overall objective of the present study was to carry out a preliminary investigation on NSM rods as a strengthening system for RC and masonry structures. In more detail, the objectives of the investigation were as follows:

- characterize the tensile properties of the FRP materials when data from the manufacturer was not available (material level);
- characterize the bond behavior of NSM FRP rods embedded in concrete or in masonry units, using coupon-size specimens (sub-system level);
- investigate the structural behavior of RC beams strengthened in shear with NSM FRP rods using full-size specimens (structural member level);

- develop a simplified design approach for shear strengthening of RC beams with NSM rods.

1.5. DOCUMENT LAYOUT

Section 2 of this document details the materials used in the experimental program. Their properties, either taken from the technical literature or experimentally determined, are reported.

Section 3 is about the experimental characterization of bond of NSM FRP rods in concrete. The experimental tests conducted on a total of 22 coupon-size specimens are described and the results presented and discussed.

Section 4 illustrates the experimental characterization of bond of NSM FRP rods in concrete masonry units. The experimental tests of 6 coupon-size specimens and their results are presented.

In Section 5, shear strengthening of RC beams with NSM CFRP rods is investigated. Results of tests conducted on 8 full-size beams with T-shaped cross-section are presented. Finally, a simple design approach is proposed and applied to predict the experimental results.

Section 6 outlines overall conclusions and recommendations for further research.

2. MATERIALS USED IN THE EXPERIMENTAL PROGRAM

2.1. INTRODUCTION

This section presents the properties of the materials used in the experimental program. These materials included concrete, reinforcing steel rebars, FRP rods, epoxy paste and concrete masonry blocks. Standard tests were performed to determine the concrete compressive strength and the yield strength of the reinforcing steel. Tensile characterization through laboratory testing was performed for the FRP rods when data from the manufacturer or the technical literature was unavailable. Tensile testing was conducted in accordance with a protocol which is already a standard test method in Japan (JSCE, 1997) and is currently under consideration to become a standard in North America (Benmokrane, 1998). For the epoxy paste, the material properties were provided by the manufacturer.

2.2. CONCRETE

The coupon-size and the full-size concrete beams tested in this experimental study were all prepared by a local contractor, with a ready-mix concrete company supplying the concrete. Concrete compression cylinders were made according to ASTM C31-95 every time a set of beams was poured, in order to determine the concrete compressive strength. Cylinders with 4-in. diameter and 8-in. length were prepared for the coupon-size specimens, while the cylinders for the full-size beams had 6-in. diameter and 12-in. length. All cylinders were tested in accordance with ASTM C39-94, within two days of testing of the corresponding specimens. A minimum of three cylinders were tested for each batch of concrete produced, and the compressive strength of the concrete was taken as the average of the obtained values of the representative samples.

Results are reported in Table 2.1. Specimens are identified with the designation codes to be used in the following sections of this document.

Table 2.1. Concrete Compressive Strength

Specimen	Batch	Size of Concrete Cylinders	No. of	Average	Standard
----------	-------	----------------------------	--------	---------	----------

Code	No.	(Diameter, in., x Length, in.)	Cylinders	Compressive Strength (psi)	Deviation (psi)
G4D6a	1	4 x 8	3	3960	92
G4D12a					
G4D12b	3			4080	108
G4D12c					
G4D18a	1			3960	92
G4D24c	4			3880	105
C3D6a	2			4100	96
C3D12a					
C3D12b	3			4080	108
C3D12c					
C3D18a	2			4100	96
C3D24b	4			3880	105
C3S6a	2			4100	96
C3S12a					
C3S12b	3			4080	108
C3S12c					
C3S18a	2			4100	96
C3S24a	4			3880	105
C4S6a	1			3960	92
C4S12a	4			3880	105
C4S18a					
C4S24a					
BV	5	6 x 12	4	4560	110
B90-7					
B90-5					
B90-5A					
B45-7					
B45-5					
BSV					
BS90-7A					

2.3. REINFORCING STEEL

ASTM standard steel rebars were used as tension, compression and shear reinforcement in the full-size beams. No. 9 rebars were used as tension reinforcement, No. 4 and No. 3 rebars were used as compression and shear reinforcement, respectively. Tensile testing was performed in accordance with ASTM A370-97. Three coupon specimens were tested for each set of rebars. The yield strength was taken as the average of the three values. Results are presented in Table 2.2.

Table 2.2. Yield Strength of Reinforcing Steel in the Full-Size Beams

Rebar Size (No.)	No. of Coupon Specimens	Average Yield Strength (ksi)	Standard Deviation (ksi)
9	3	62.7	0.5
4		51.8	0.6
3		50.0	0.6

2.4. FRP RODS

The mechanical properties of FRP rods are influenced by factors such as fiber type and content, matrix type, and manufacturing method. A characterization of their tensile performance is necessary for their application as NSM reinforcement.

Three different types of FRP rods were used in this experimental program, namely, Glass FRP (GFRP) deformed, CFRP smooth and CFRP deformed rods (Figure 2.1). Rods of two different diameters (No. 3 and No. 4) were used, except for CFRP deformed, of which only No. 3 rebars were available on the market. The tensile properties of these rods, either provided by the manufacturer or available in the technical literature or determined by laboratory testing, are reported in the following.

2.4.1. CFRP Deformed Rods. CFRP deformed No. 3 rods manufactured through the hybrid pultrusion process and commercially known with the name of Carbon C-Bar were supplied by Marshall Industries Composites Inc. For this type of FRP rebar, tensile characterization was performed in the laboratory.

2.4.1.1. Specimens for Tensile Testing. An essential requirement for conducting tensile tests is a suitable anchor device to grip the specimens without causing slippage or premature local failure during the test (Yan et al., 1999). The conventional method for tensile testing of steel rebars consisting of steel grip jaws is not suitable for tensile testing of FRP rods. The reason is that FRP rods are sensitive to compressive forces in the transverse direction. The transverse compressive strength, controlled by the resin properties, is usually less than 10% of the longitudinal tensile strength, controlled by the fibers. The stress concentration due to gripping can easily crush the specimen and result in premature failure. A grouted anchor consisting of a steel pipe filled with expansive grout was utilized for the test (Dye et al., 1998). The internal pressure due to expansion of the grout prevents the rod from slipping out of the pipe when direct tension is applied. This type of anchorage device distributes the gripping force to a much larger area of rod surface and may

prevent premature failure. The dimensions of the pipes were: length 18 in., outside diameter 1.66 in, wall thickness 0.14 in.

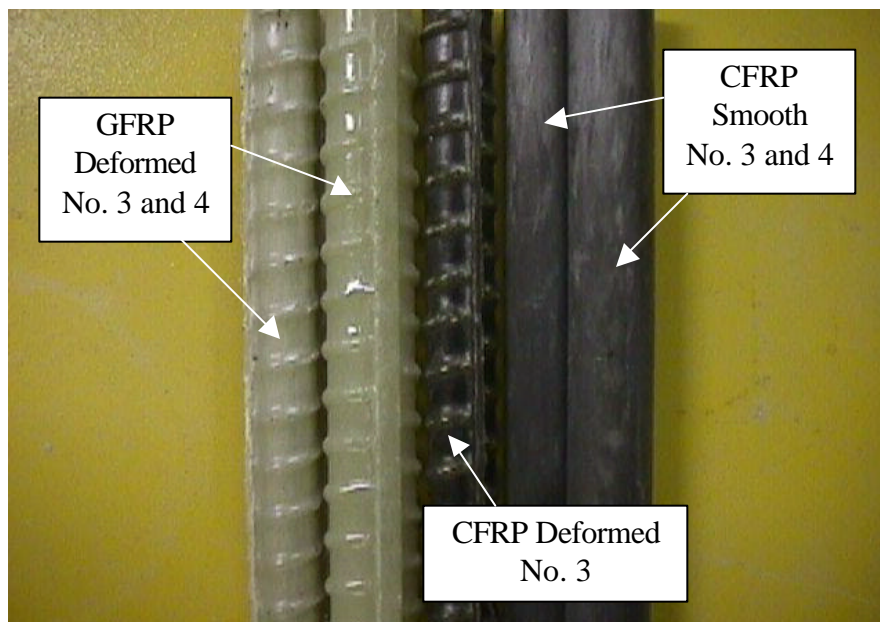


Figure 2.1. FRP Rods Used in the Experimental Program

BRISTAR 100 expansive cement manufactured by Onoda Cement Corporation was used as grout. It was mixed according to manufacturer's specifications with a water-to-cement ratio by weight of 0.29. After pouring, the specimens were allowed to set for 72 hours before testing.

The total length of the test specimens was 5 ft., which included test section and anchoring section. The length of the test section was larger than the minimum suggested value: the greater of 4 in. and 40 times the nominal diameter of the FRP rod (JSCE, 1997; Benmokrane, 1998).

Three specimens were prepared. Figure 2.2 illustrates the specimens ready for testing.

2.4.1.2. Tensile Test Procedure. Tensile tests were performed using a Tinius-Olsen Universal Testing Machine. The specimen was set up across the two cross-heads of the machine and aligned with the axis of the machine grips. The anchor at one end rested on the top cross-head. A 3/4-in. thick steel plate with a slot on it was inserted between the anchor and the cross-head to distribute the load. An identical plate was attached at the lower end of the bar for the same purpose. A strain gage with gage length of 1/2 in. was applied at the center of the test section in the direction of tensioning. Figure 2.3 illustrates the test setup.

The test was performed in displacement control mode. The loading was applied at a rate of 5 kips per minute, corresponding to 45 ksi per minute. This rate is within the suggested values of 14.5 ksi and 72.5 ksi per minute (JSCE, 1997; Benmokrane, 1998).



Figure 2.2. Specimens of CFRP Deformed Rods Ready for Testing



Figure 2.3. Tensile Test Setup

2.4.1.3. Tensile Test Results. All specimens showed a linear elastic behavior up to failure and experienced tensile failure, which indicated that the bar had developed its full tensile capacity, and the anchor was efficient. Figure 2.4 shows the stress-strain relationship of the tested specimens. Figure 2.5 is a detail of a failed specimen.

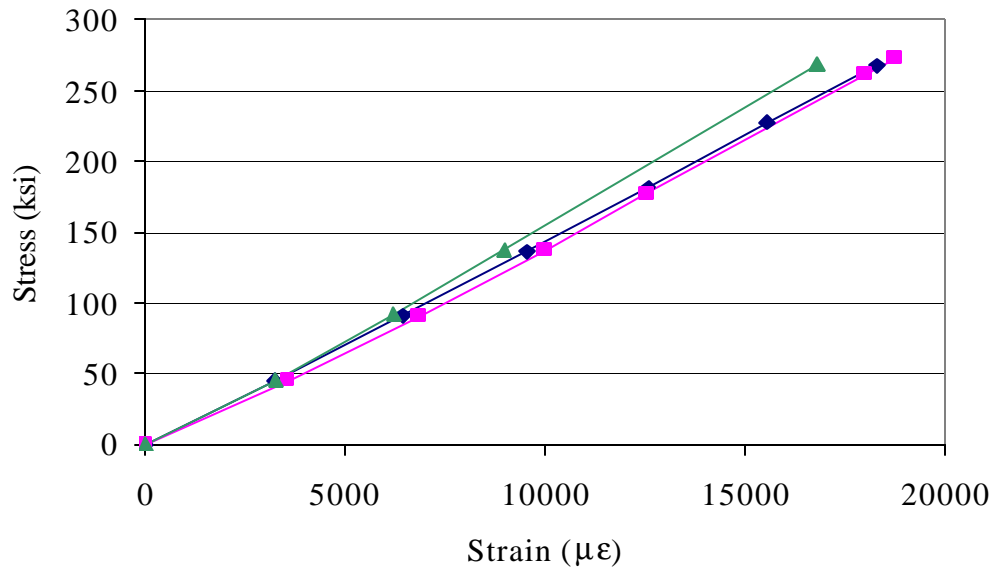


Figure 2.4. Stress – Strain Relationship of CFRP No. 3 Deformed Rods

Tensile strength, modulus of elasticity and ultimate strain were computed using load and strain data recorded during the test and the nominal cross-sectional area of the rod. Test results are summarized in Table 2.3. The modulus of elasticity was calculated from the difference between 20% and 60% of the tensile capacity according to the load-strain curve. The ultimate strain was computed dividing the ultimate stress by the calculated modulus of elasticity.



Figure 2.5. Tensile Failure of CFRP No. 3 Deformed Rods

Table 2.3. Results of Tensile Testing on CFRP No. 3 Deformed Rods

Specimen No.	Nominal Diameter (in.)	Cross-Sectional Area (in ²)	Tensile Strength (ksi)	Tensile Modulus (ksi)	Ultimate Strain (%)
1	0.375	0.110	268	14580	1.84
2			280	14980	1.87
3			268	15990	1.68
Average			272	15200	1.79
Standard Deviation			6.9	700	0.1
Coefficient of Variation			2.5%	4.6%	5.6%

2.4.2. GFRP Deformed Rods. GFRP No. 3 and No. 4 deformed rods commercially known with the name of C-Bar were supplied by Marshall Industries Composites Inc. These rebars are manufactured through the hybrid pultrusion/compression molding process. The outer core is composed of a sheet molding compound with chopped fiber mats embedded in urethane modified vinyl ester. The inner core is composed of unidirectional E-glass fibers embedded in recycled PET resin material (Marshall, 1998). Table 2.4 reports the primary properties of interest of C-Bar No. 3 and No. 4 as specified by the manufacturer.

Table 2.4. Properties of C-Bar (Marshall, 1998)

Bar Size (No.)	Nominal Diameter (in)	Cross-Sectional Area (in ²)	Tensile Strength (ksi)	Tensile Modulus (ksi)	Ultimate Strain (%)
3	0.375	0.110	121	6000	2.00
4	0.500	0.196	116	6000	1.90

2.4.3. CFRP Smooth Rods. CFRP No. 3 and No. 4 smooth pultruded rods were supplied by DFI Pultruded Composites, Inc. Prior to application, the rods were sandblasted to enhance the bond characteristics. The sandblasting machine was an ECONOLINE operated at 80 psi air pressure. The sandblasting material consisted of 50 micron glass beads manufactured by Comoco Inc.

Laboratory tensile tests on this type of FRP rods have been conducted by previous researchers (Warren, 1998). Results are reported in Table 2.5.

Table 2.5. Properties of DFI Pultruded CFRP Rods (Warren, 1998)

Bar Size (No.)	Nominal Diameter (in.)	Cross-Sectional Area (in ²)	Tensile Strength (ksi)	Tensile Modulus (ksi)	Ultimate Strain (%)
3	0.375	0.110	225	23900	0.94
4	0.500	0.196	202*	23900*	0.85*

*To be verified.

2.5. EPOXY PASTE

The material used to embed the NSM FRP reinforcement in the grooves was an epoxy-based paste commercially known as Concsive Paste LPL, manufactured by Master Builders Technologies. Table 2.6 reports the mechanical properties of the paste, as specified by the manufacturer.

Table 2.6. Properties of Concsive Paste LPL (Master Builders, 1996)

Tensile Strength (ASTM D 638) (psi)	2000
Elongation at Break (ASTM D 638) (%)	4
Compressive Yield Strength (ASTM D 695) (psi)	8000
Compressive Modulus (ASTM D 695) (ksi)	400

2.6. CONCRETE BLOCKS

Concrete masonry products are defined as solid or hollow, depending on whether they contain 75% or more net solid horizontal cross-sectional area. In practice, hollow blocks are more frequently used because of their reduced weight, ease of handling, ease of reinforcing, and overall economy. The percent solid typically is in the range from 50 to 60 %.

Concrete masonry units come in a large variety of sizes and shapes. The most common concrete block has a nominal size of 8 x 8 x 16 in; for convenience, this size is referred to as the standard block. The actual block dimensions are 3/8 in. less than the nominal values, to allow for a standard mortar joint thickness.

The compressive strength of a concrete masonry unit is important from two points of view: first, the higher the strength, the better the durability under severe weathering conditions and, second, unit strength tests with mortar strength tests can serve as the basis for satisfying the required masonry compressive strength. Hollow blocks can be manufactured in strengths, ranging from 1500 to about 4000 psi based on net area, to suit low-rise and high-rise construction.

There is no widely accepted method for determining the tensile strength of concrete blocks. Splitting tensile strength tests across the face shells have shown that the ratio of splitting tensile strength to compressive strength ranges from 0.08 to 0.16 (Drysdale et al., 1994).

Standard concrete masonry blocks were involved in one phase of the experimental program. Hollow two-cell blocks with a percent solid of 50% were selected (Figure 2.6). The net compressive strength of the blocks was experimentally determined as part of another research project (Tinazzi et al., 2000) and resulted to be 3200 psi. The tensile strength was not obtained.



Figure 2.6. Standard Concrete Blocks

3. BOND OF NSM FRP RODS IN CONCRETE

3.1. INTRODUCTION

3.1.1. Background and Problem Statement. Many researchers have studied the characteristics of bond between steel rebars and concrete, which resulted in a full understanding of the related modes of failure (Lutz & Gergely, 1967, Lutz, 1970, Goto, 1971, Tepfers, 1973, Orangun et al., 1977, Jirsa et al., 1979, Tepfers, 1979, Eligehausen et al., 1983). In general, a smooth bar embedded in concrete develops bond with concrete through two mechanisms, adhesion between the concrete and the bar, and a small amount of friction (MacGregor, 1997). Both mechanisms are lost at higher levels of tension loads, particularly because of the slight decrease in the cross-sectional area due to Poisson's ratio. Insufficient embedment length would therefore lead to the pull-out of the rod. With sufficient embedment length, the full capacity of the steel rebar can be achieved. Similar bond transfer mechanisms of adhesion and friction are present when deformed steel bars are loaded with small loads. As the load increases, these bond transfer mechanisms are lost, leaving the bond to be transferred through bearing stresses between concrete and the deformations on the bar. The bearing stresses will result in circumferential tensile stresses in the concrete around the bar. As a result, the concrete will split parallel to the bar and the crack will propagate out toward the surface of the beam. The splitting cracks tend to develop along the shortest distance between the bar and the concrete surface (Orangun et al., 1977 and Jirsa et al., 1979).

In general, steel bars are very effective and cost efficient for concrete reinforcement. However, corrosion of steel in a corrosive environment is a serious problem and results in durability problems. FRP materials, on the other hand, are not corrosive and can therefore improve the durability of concrete (Nanni, 1993). For FRP rods embedded in concrete, a notable amount of experimental work in the area of bond has already taken place (Al-Zahrani, 1995, Cosenza et al., 1997, Bakis et al., 1998, Tepfers, 1998, Tighiouart et al., 1998, Focacci, 1999, Focacci et al., 2000). Many researchers such as Al-Zahrani (1995) and Tighiouart et al. (1998) confirmed lower bond strength of FRP bars to concrete, which in turn was dependent on the diameter of the bar. Bakis et al. (1998) concluded that the bond between FRP bars and concrete is controlled by the

properties of the FRP bars. They investigated both smooth and deformed FRP bars. In the case of smooth FRP bars, they concluded that friction is the dominant bond mechanism and that the major factors that affect it are longitudinal stiffness, transverse stiffness, and the major Poisson’s ratio of the bar. For the case of lugged FRP bars, they observed that bond is governed by the sequential shearing of the FRP lugs and that the concrete strength is of much less influence on the bond behavior.

Currently, very limited literature is available on bond characteristics and modes of failure of NSM FRP rods in concrete. Two experimental studies documented to date have been briefly outlined in section 1.3.1 of this document.

As the new technology of NSM FRP rods emerges, the bond behavior is the first issue that needs to be addressed. The importance of bond is that it is the means for the transfer of stress between the concrete and the FRP reinforcement in order to develop composite action. The bond behavior has influence on the ultimate capacity of the reinforced element as well as on serviceability aspects such as crack width and crack spacing.

3.1.2. Objective. The objective of this section of the experimental program was to investigate bond between NSM FRP rods and concrete. Some of the factors expected to affect bond performance were addressed, namely: bonded length, rod diameter, type of FRP material, surface configuration of the rod, and size of the groove.

A series of specimens was tested to assess the influence of each of the above mentioned factors on the bond behavior. Concrete strength and type of epoxy were not varied, although they are significant parameters.

3.2. DESCRIPTION OF THE SPECIMENS

Among the many different types of bond tests reported in the literature, the most common are the direct pull-out test and the beam pull-out test. It is generally believed that beam pull-out tests are more representative of the behavior of flexural members and are therefore preferable to direct pull-out tests. In direct pull-out tests, the concrete surrounding the rebar is in compression. This delays the initiation of cracks and thus leads to higher bond strengths. Therefore, the decision to perform beam pull-out tests was made.

In order to collect reliable data while maintaining the simplicity of the tests, the selection of specimen shape and dimensions had to be optimized. A series of experimental tests to characterize bond between CFRP sheets and concrete had been previously performed at the University of Missouri – Rolla (Miller, 1999). The specimen used in this program was found to be suitable also to study the bond of NSM FRP rods in concrete. The specimens were unreinforced concrete beams with an inverted T-shaped cross-section. This section was chosen to provide a larger tension area for concrete while minimizing the overall weight of the beam. A larger tension area for concrete was needed to ensure that no flexural cracking would occur in the specimen before failure of the bond.

No flexural cracking occurred in the experimental program conducted by Miller (1999). However, the maximum value of applied load leading to bond failure was expected to be higher in the study presented herein. Therefore, the position of the bonded length of the rod had to be chosen appropriately in order to prevent flexural cracking before bond failure. Details about this choice will be described in Appendix A.

The dimensions of the beams are given in Figure 3.1. The specimen had a hinge at the top and a saw cut at the bottom, both located at mid-span. The purpose of the hinge and saw cut was to control the distribution of the internal forces. During loading of the specimen, the saw cut caused a crack to develop at the center of the beam and extend up to the hinge. Therefore, the compressive force in the beam at mid-span was located at the center of the hinge and the internal moment arm was known and constant for any given load level above the cracking load. This allowed to compute the tensile stress in the rod with more accuracy. Figure 3.2. illustrates a free-body diagram of the beam.

Each beam had a NSM FRP rod applied to the tension face and oriented along the longitudinal axis of the beam. One side of the beam was the test region, with the NSM FRP rod having a limited bonded length and being unbonded in the remaining part. The rod was fully bonded on the other side of the beam, to cause bond failure to occur in the test region.

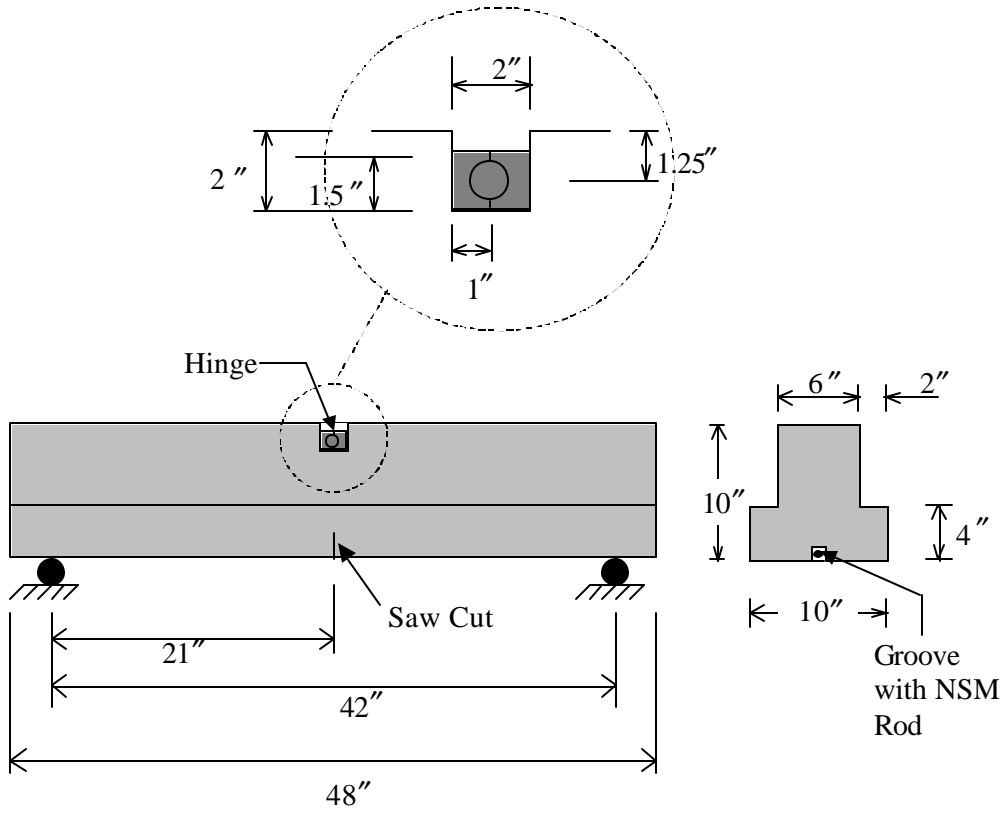


Figure 3.1. Test Specimen

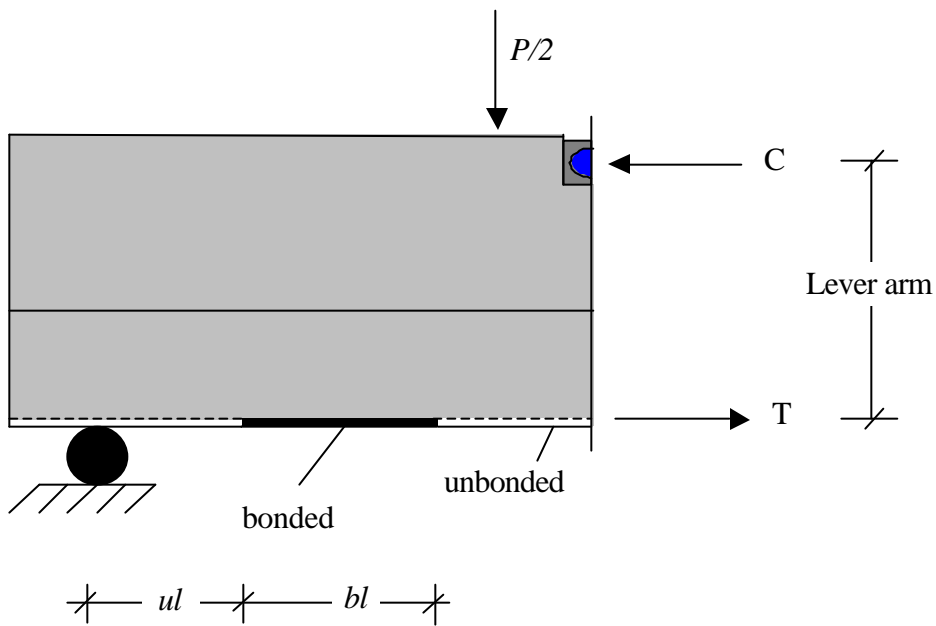


Figure 3.2. Free-Body Diagram

The variables examined in the experimental test matrix were the following:

- bonded length. Four different bonded lengths were selected, equal to 6, 12, 18 and 24 times the diameter of the rod;
- rod diameter. Rods No. 3 and No. 4, having nominal diameter 3/8 in. and 1/2 in., respectively, were examined;
- type of FRP material. Both CFRP and GFRP rods were used;
- surface configuration of the rod. For the CFRP rods, the effect of two different surface conditions, deformed and sandblasted, was examined;
- size of the groove. For some types of rods, specimens with three different sizes of the groove were tested. The groove width was maintained equal to the groove depth in all the tested specimens, so that the term “size” is used in the following to refer to either the groove depth or width.

As previously mentioned, the target concrete strength was chosen to be 4000 psi for all the specimens.

Table 3.1 summarizes all specimens that were tested together with the designation that will be used to identify them. The specimen designation refers to the following parameters: type of FRP material – rod size – rod surface configuration – bonded length – groove size. As an example, C3S18a refers to the specimen with a CFRP rod, where the rod is a No. 3 sandblasted, the bonded length is 18 times the rod diameter and the groove size is the first of the three different sizes examined for rods No. 3. G4D12b refers to the specimen with a GFRP rod No. 4 deformed, where the bonded length is 12 times the rod diameter and the groove size is the second of the three different sizes examined for rods No. 4.

Table 3.1. Description of the Specimens

Specimen Designation	Target Concrete Strength (psi)	Type of FRP Rod	Rod Size (No.)	Surface Configuration	Bonded Length (No. of d_b)	Groove Size (in)
G4D6a	4000	Glass	4	Deformed	6	5/8
G4D12a					12	5/8
G4D12b						3/4
G4D12c						1
G4D18a						18
G4D24c					24	1
C3D6a		Carbon	3	Deformed	6	1/2
C3D12a					12	1/2
C3D12b						3/4
C3D12c						1
C3D18a						18
C3D24b					24	3/4
C3S6a		Carbon	3	Sandblasted	6	1/2
C3S12a					12	1/2
C3S12b						3/4
C3S12c						1
C3S18a						18
C3S24a					24	1/2
C4S6a		Carbon	4	Sandblasted	6	5/8
C4S12a					12	
C4S18a	18					
C4S24a	24					

3.3. SPECIMEN PREPARATION

The phases of the specimen preparation were: cutting of the groove, choice of the position of the bonded length, application of strain gages on the rod and positioning of the rod.

3.3.1. Cutting of the Groove. Each of the specimens had a groove cut in the tension face and oriented along the longitudinal axis, where the FRP rod had to be mounted. After the beams had cured properly, the grooves were cut from the contractor using a concrete saw. All the grooves had square cross-section, with variable size according to the established test matrix.

3.3.2. Choice of the Position of the Bonded Length. The position of the bonded length was chosen according to the criteria presented in Appendix A. The values of ul (distance of the starting point of the bonded length from the closest support of the beam, Figure 3.2) adopted for the specimens are presented in Table 3.2.

3.3.3. Application of Strain Gages. Strain gages were applied on the surface of the FRP rods prior to their application. The purpose was to monitor the strain distribution along the rod during the test. All the strain gages had a gage length of 1/2 in. to ensure localized strain measurement. The application of strain gages on the deformed rods involved the removal of the surface deformations in the spots where the gages had to be placed. In each of these spots, two ribs were removed by means of a belt sander.

Table 3.2. Position of the Bonded Length

Rod Size (No.)	Bonded Length (No. of d_b)	ul (in)
3	6	11
	12	8
	18	5
	24	2
4	6	8
	12	6
	18	4
	24	2

Figures 3.3 through 3.8 indicate the location of the strain gages for each value of the bonded length for rods No. 3 and No. 4. Three or four strain gages were placed within the bonded length and an additional one was applied in the unbonded region.

No strain gages were applied to the specimens with a bonded length of six diameters. On a short bonded length, the presence of strain gages would have significantly influenced the bond behavior, especially in the case of deformed rods where the superficial properties had to be modified prior to their application.

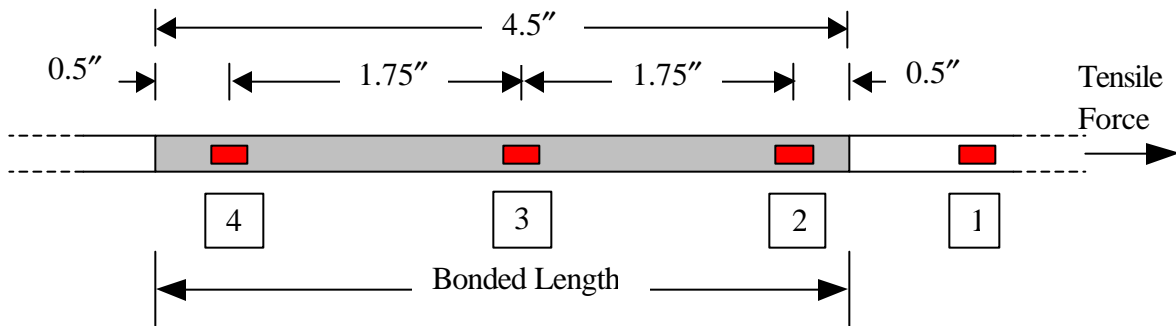


Figure 3.3. Position of the Strain Gages (Rods No. 3, Bonded Length $12 d_b$)

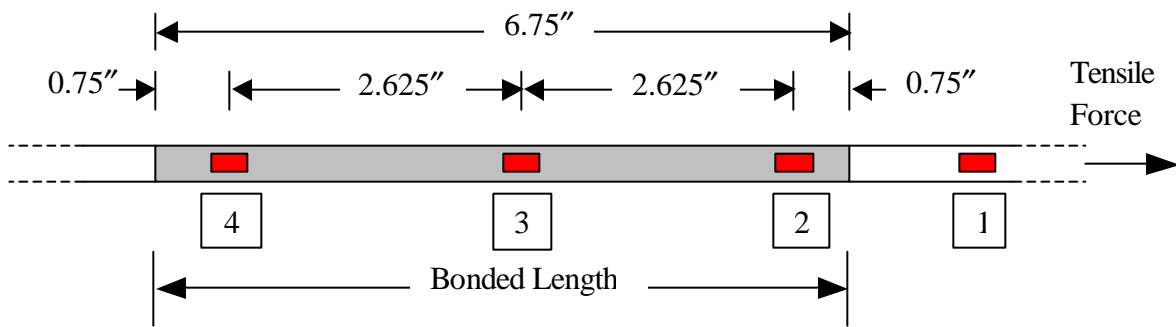


Figure 3.4. Position of the Strain Gages (Rods No. 3, Bonded Length $18 d_b$)

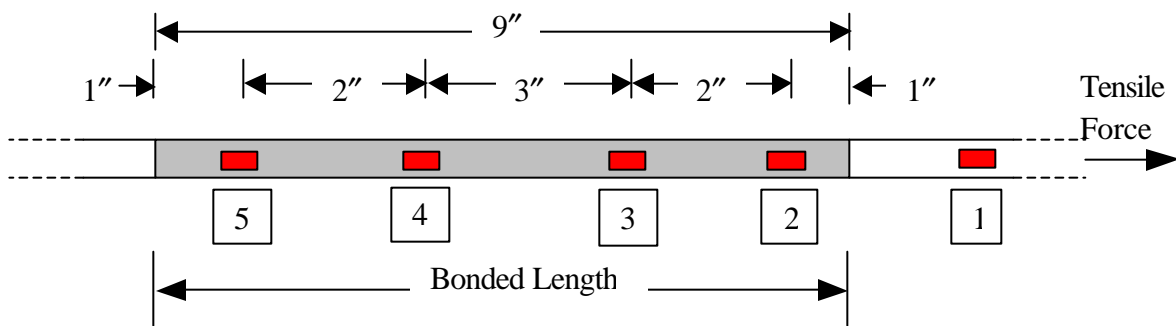


Figure 3.5. Position of the Strain Gages (Rods No. 3, Bonded Length $24 d_b$)

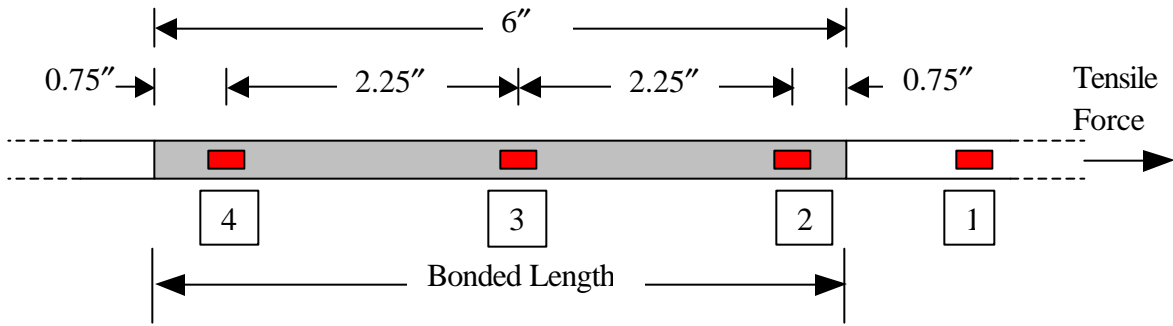


Figure 3.6. Position of the Strain Gages (Rods No. 4, Bonded Length $12 d_b$)

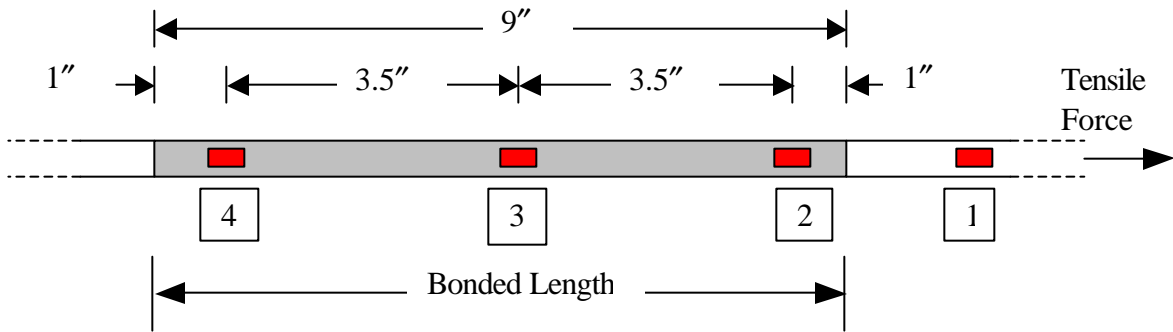


Figure 3.7. Position of the Strain Gages (Rods No. 4, Bonded Length $18 d_b$)

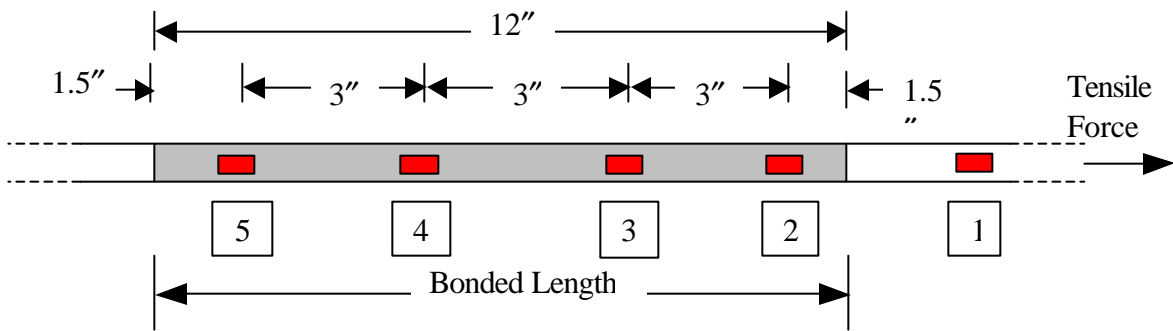


Figure 3.8. Position of the Strain Gages (Rods No. 4, Bonded Length $24 d_b$)

3.3.4. Application of the NSM Rod. Figure 3.9 shows some specimens before application of the rods. The grooves were air blasted to remove the powdered concrete produced by the cutting process and all the possible loose material. Then the epoxy paste was prepared by mixing the two components (resin and hardener) in 2:1 proportion by volume with a power mixer. The groove was filled half-way with the paste (Figure 3.10-a), the rod was then placed in the groove and lightly pressed (Figure 3.10-b). This forced the paste to flow around the bar and fill completely between the bar and the sides of the groove. The groove was then filled with more paste and the surface was leveled (Figure 3.10-c). Figure 3.10-d shows the test side of the specimen after preparation.



Figure 3.9. Specimens Before Preparation

3.4. TEST PROCEDURE

The epoxy paste was allowed to cure for at least 15 days (full cure time at room temperature) prior to testing of the beams. Testing was performed using a Tinius-Olsen Universal Testing Machine. The beams were loaded under four-point bending with a shear span of 19 in. Each beam was instrumented with two Linear Variable Differential Transducers (LVDTs). One LVDT was placed at mid-span to measure deflection of the beam. The other one was used to measure the slip of the rod at the end of the test region. Load, mid-span deflection, slip and strains were all recorded with a one-Hertz sampling

rate by a LABTECH (Laboratory Technologies Corp.) data acquisition system. Figure 3.11 is a picture of the test setup.

Testing was performed by loading the beam in displacement controlled mode until failure resulted. At a value of load much lower than the ultimate, a crack formed at mid-span of the beam, starting from the saw cut and extending up to the hinge. This allowed a more accurate calculation of the tensile force in the rod, since the lever arm of the cracked beam was known and constant for any given load level.

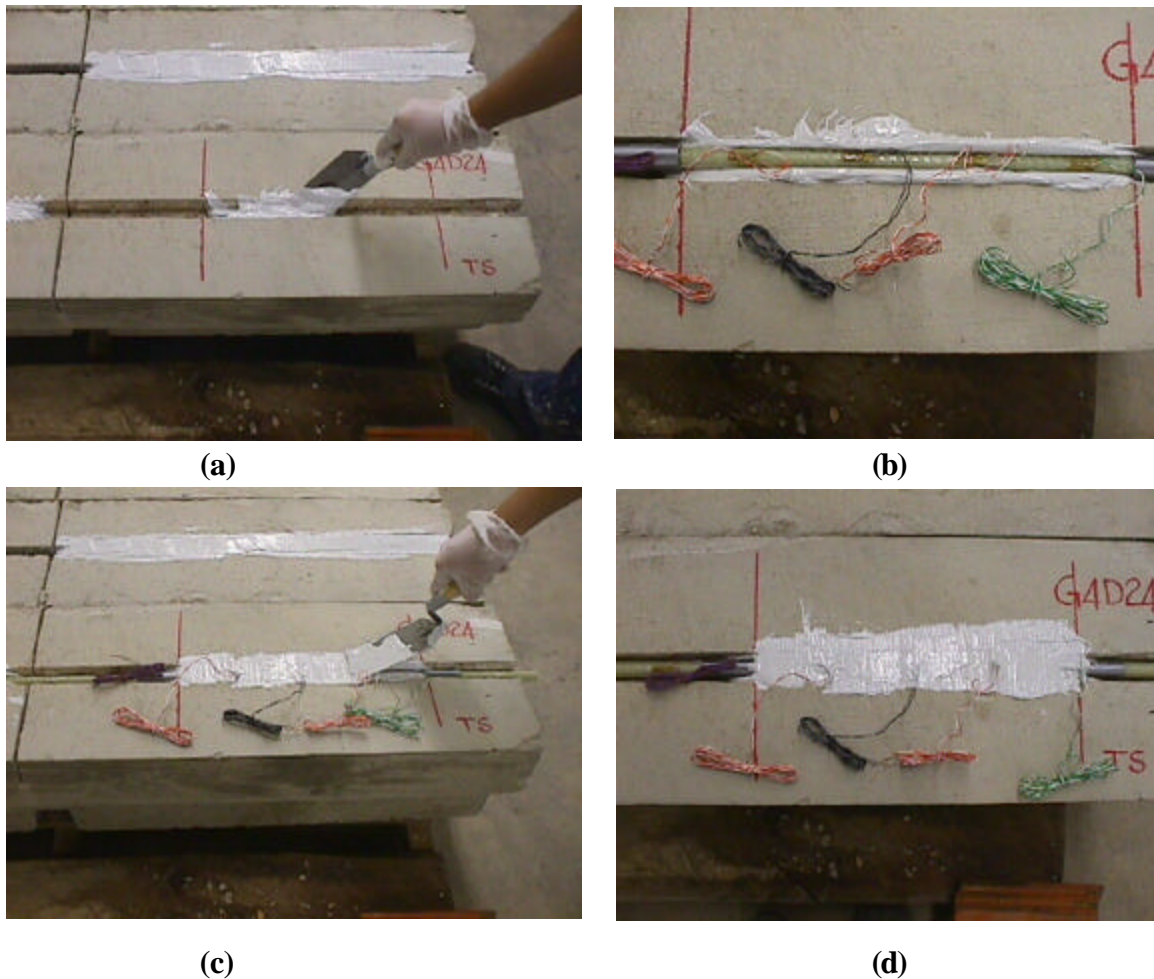


Figure 3.10. Specimen Preparation



Figure 3.11. Test Setup

3.5. EXPERIMENTAL RESULTS FOR SPECIMENS WITH GFRP No. 4 DEFORMED RODS

3.5.1. Introduction. Six specimens with GFRP No. 4 deformed rods were tested. The first series of specimens consisted of three specimens with the same groove size (5/8 in.) and three different bonded lengths ($6 d_b$, $12 d_b$, $18 d_b$). The value of the groove size was chosen as the minimum possible from a practical standpoint, that is a value such that the minimum possible clearance is left between a No. 4 deformed rod and the sides of the groove. The purpose of this series was to investigate the effect of the bonded length for this minimum value of the groove size. These three specimens were designated as G4D6a, G4D12a and G4D18a.

Subsequently, two more specimens were tested, characterized by a bonded length of $12 d_b$ and two different values of the groove size, namely, 3/4 in. and 1 in. These specimens were designated as G4D12b and G4D12c. The purpose was to examine the effect of the groove size on the test results, particularly on ultimate load and failure mode.

After testing of these two specimens, a groove size of 1 in. was identified as the recommendable size for embedment of a No. 4 GFRP deformed rod. Therefore, an additional specimen was tested, with a groove of the “optimum” size and a bonded length of $24 d_b$ (specimen G4D24c). A longer bonded length was chosen to obtain more reliable

results. In fact, it is generally recognized that, in a bond test, longer bonded lengths are more capable to represent the non-uniform interface conditions and to make negligible the unavoidable end effects.

3.5.2. General Results. Test results in terms of ultimate pull-out load, average bond strength and failure mode are summarized in Table 3.3. The expression “pull-out load” has been adopted to refer to the tensile load directly applied to the NSM rod after cracking of the beam. This load could be computed with accuracy from the value of the external applied load as a result of the specimen configuration.

The ultimate pull-out load has been also expressed as a percentage of the ultimate tensile load of the FRP rod. This can give an idea of how efficiently the rods can be used when bond is the controlling factor.

The average bond strength t_{bu} was calculated as follows:

$$t_{bu} = \frac{T_u}{p \cdot d_b \cdot l_b} \quad (3.1)$$

where T_u is the ultimate pull-out load, d_b the nominal diameter of the rod and l_b the bonded length.

Table 3.3. Test Results for Specimens with GFRP No. 4 Deformed Rods

Spec. Code	Bonded Length (No. of d_b)	Groove Size (in.)	Avg. Concrete Strength (psi)	Ultimate Pull-Out Load (lbs)	Percent. of Ultimate Tensile Load (%)	Avg. Bond Strength (psi)	Failure Mode
G4D6a	6	5/8	3960	5548	24	1177	SOE
G4D12a	12	5/8		7778	34	825	SOE
G4D12b	12	3/4	4080	8307	36	881	SOE+C
G4D12c	12	1		9628	42	1022	SOE+C
G4D18a	18	5/8	3960	9563	41	676	SOE
G4D24c	24	1	3880	13918	60	738	SOE+C

SOE = Splitting of Epoxy;

C = Concrete Cracking.

The failure mode is indicated for all specimens in the last column. A detailed description of the failure modes will be reported in Section 3.5.3.

Data recorded from the LVDTs and the strain gages was displayed graphically as shown in the following. First, the external load applied to the specimen was plotted versus the mid-span deflection recorded by means of an LVDT. This graph was used to check the overall behavior of the specimen during loading. The load vs. deflection diagram for specimen G4D12a is illustrated in Figure 3.12 as a representative example. The instant of cracking is clearly visible at a load level of 2930 lbs, after which the applied load starts increasing again until failure occurs in a sudden fashion.

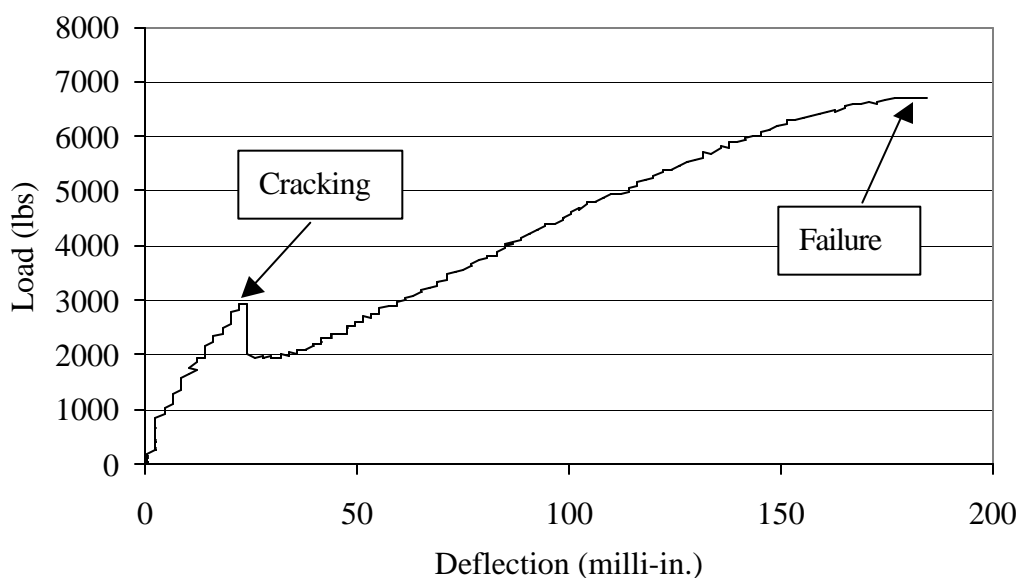


Figure 3.12. Load vs. Mid-Span Deflection for Specimen G4D12a (Failure by Epoxy Splitting)

3.5.3. Failure Modes. As previously presented in Table 3.3, failure occurred for all the specimens by splitting of the epoxy paste in which the NSM rods were embedded, accompanied or not by cracking of the concrete surrounding the groove. During testing, a crackling noise revealed the progressive cracking of the epoxy paste. Eventually, the epoxy cover was completely split and the load suddenly dropped. Although this overall behavior was common to all the specimens, some differences could be observed as bonded length and groove size were changed.

In specimens G4D6a and G4D12a, having the minimum groove size, failure occurred by splitting of the epoxy paste which disintegrated in very small pieces. The

aspect of the test side of specimen G4D12a after failure is illustrated in Figure 3.13. The epoxy cover had been totally split off and no damage was visible in the surrounding concrete. The deformations on the bar surface were also intact.



Figure 3.13. Specimen G4D12a After Failure

Very similar was the aspect of specimen G4D18a, having the minimum groove size and a bonded length of 18 bar diameters. In this case, some damage in the concrete surrounding the rod was visible (Figure 3.14-a) and the deformations on the rod surface in the region close to the loaded end had been partially sheared off (Figure 3.14-b).

In specimens G4D12b and G4D12c, due to the larger depth of the groove, a higher level of damage was observed in the concrete at the sides of the groove. This can be clearly noticed by comparing Figures 3.13 and 3.15-a, which refer to specimens having the same value of bonded length but the minimum and the maximum groove size, respectively. Also, since specimen G4D12c was able to sustain a load slightly higher than G4D18a, shearing-off of the rod lugs occurred also in specimen G4D12c (Figure 3.15-b).

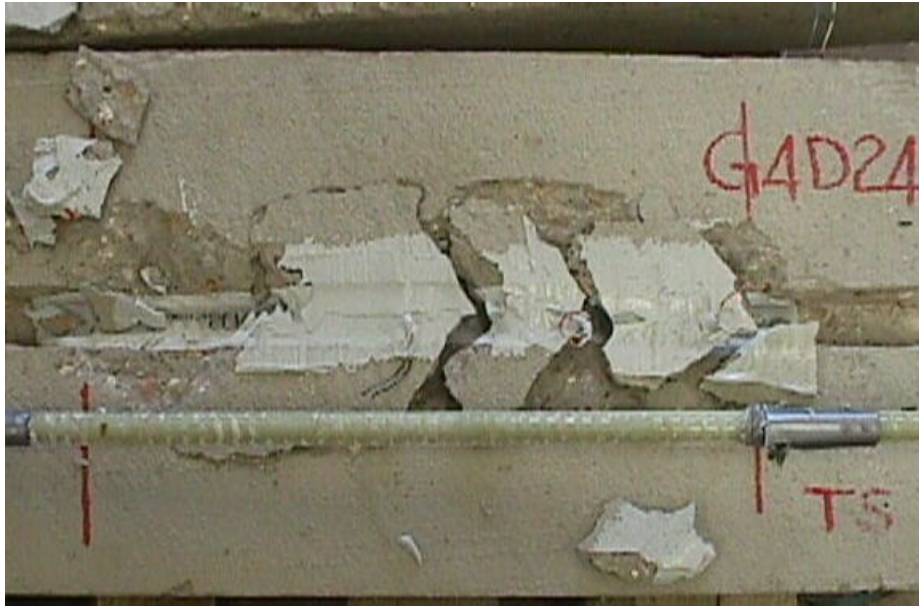


(a) (b)
Figure 3.14 . Specimen G4D18a After Failure



(a) (b)
Figure 3.15. Specimen G4D12c After Failure

Finally, the test side of specimen G4D24c after failure is presented in Figure 3.16. In this specimen, inclined cracks formed in the epoxy paste and propagated in the concrete surrounding the groove (Figures 3.16-a and 3.16-b). At a closer visual inspection, longitudinal splitting cracks were also visible in the epoxy paste and the rod deformations were extensively sheared off (Figure 3.16-c).



(a)



(b)



(c)

Figure 3.16. Specimen G4D24c After Failure

3.5.4. Free-End Slip Data. Slip at the free end of the rod in the test side was measured by means of an LVDT. The pull-out load vs. the free-end slip for three specimens is plotted in Figure 3.17.

In specimen G4D18a, no free-end slip was recorded prior to failure. It is well known that, when testing bond between rebars and concrete, a value of the bonded length exists beyond which the rod free end does not slip before failure. The same phenomenon

occurs in the case of NSM rods. An 18-diameter bonded length was enough to prevent the free end from slipping.

From the pull-out load, the average bond stress can be computed as follows:

$$t_b = \frac{T}{p \cdot d_b \cdot l_b} \quad (3.2)$$

where t_b is the average bond stress and T is the pull-out load. Therefore, average bond stress vs. free-end slip diagrams can be plotted, as in Figures 3.18 and 3.19.

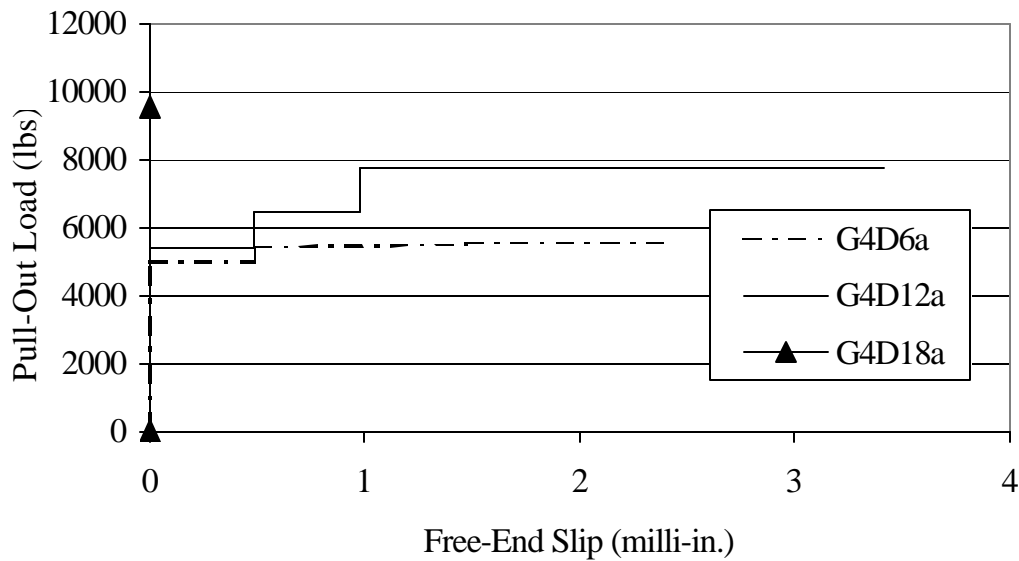


Figure 3.17. Pull-Out Load vs. Free-End Slip for Specimens G4D6a, G4D12a and G4D18a

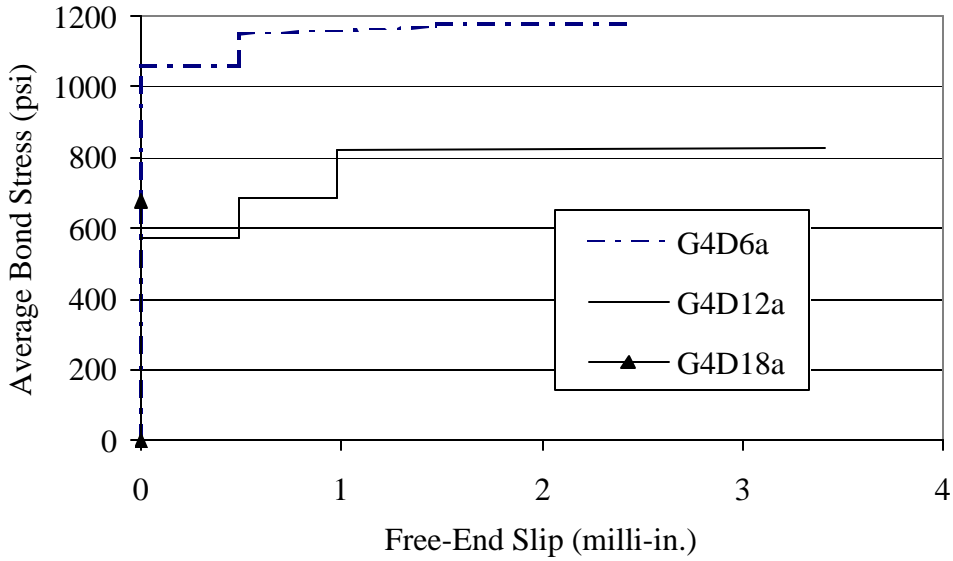


Figure 3.18. Average Bond Stress vs. Free-End Slip for Specimens G4D6a, G4D12a and G4D18a

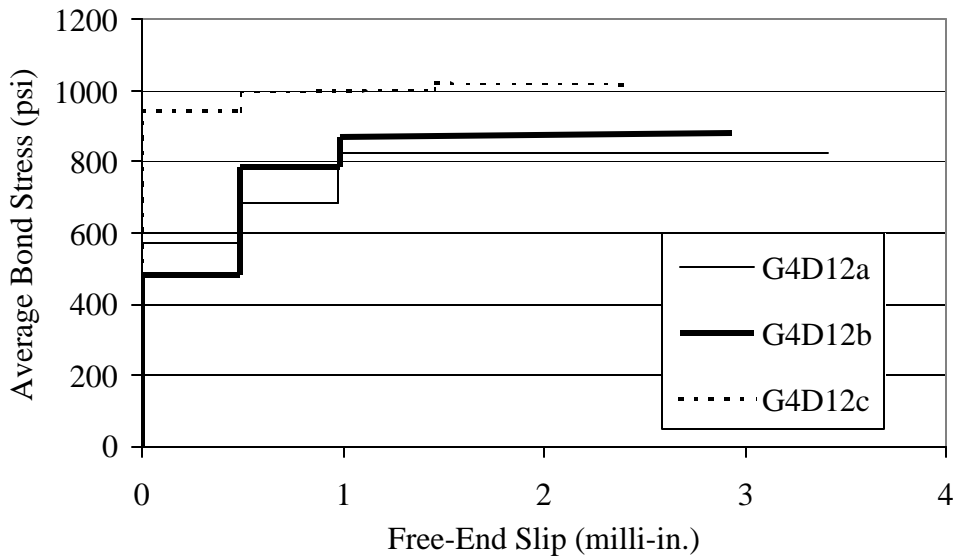


Figure 3.19. Average Bond Stress vs. Free-End Slip for Specimens G4D12a, G4D12b and G4D12c

3.5.5. Strain Data. Strain gages were applied at various locations (Figures 3.6 through 3.8) on the surface of the FRP rods to monitor the strain distribution along the rod during the test. A typical pull-out load vs. strain diagram is shown in Figure 3.20. The strain gages are numbered starting from the one in the unbonded region and proceeding toward the rod free end.

The data from the strain gages was used to plot strain vs. location graphs. In these graphs, the strain in the rod along the bonded length is plotted for different values of the pull-out load. All points were obtained from the readings of the strain gages, except for the strain at the end of the bonded length, which was assumed to be equal to zero. Figure 3.21 shows a typical strain vs. location diagram. The left end (location equal to zero) and the right end of the x axis correspond to the free end and to the loaded end of the bonded length, respectively.

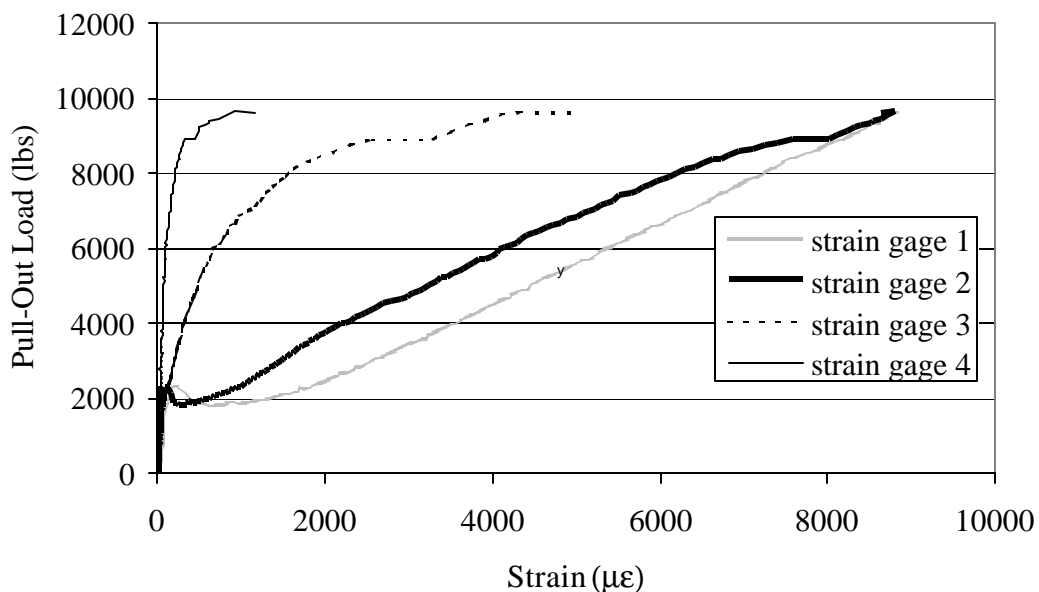


Figure 3.20. Pull-Out Load vs. Strain for Specimen G4D12c

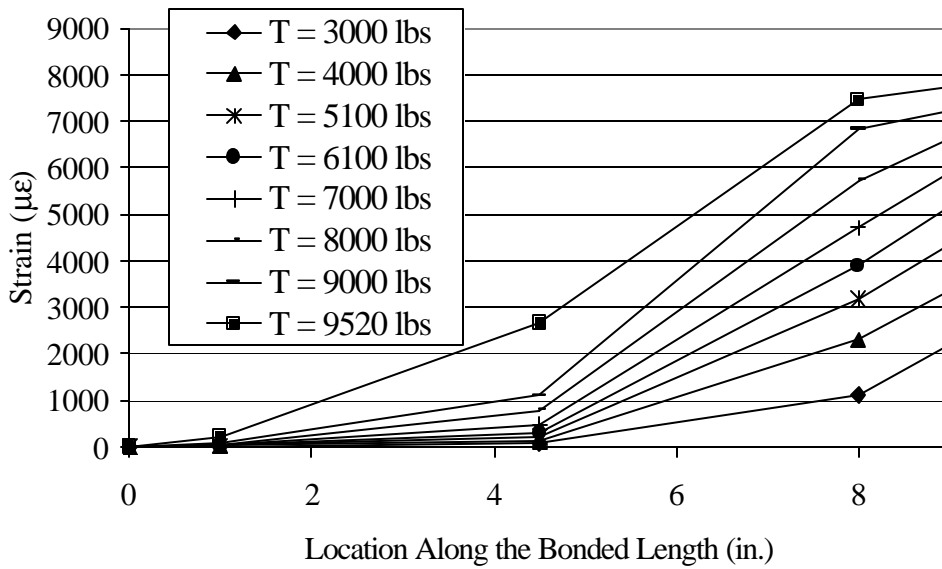


Figure 3.21. Strain vs. Location Diagram for Specimen G4D18a

3.6. EXPERIMENTAL RESULTS FOR SPECIMENS WITH CFRP No. 3 DEFORMED RODS

3.6.1. Introduction. Six specimens with CFRP No. 3 deformed rods were tested. As in the case of GFRP rods, the first series of specimens consisted of three specimens with the same groove size (1/2 in.) and three different bonded lengths ($6 d_b$, $12 d_b$, $18 d_b$). The value of the groove size was chosen as the minimum possible from a practical standpoint, that is a value such that the minimum possible clearance is left between a No. 3 deformed rod and the sides of the groove. The purpose of this series was to investigate the effect of the bonded length for this minimum value of the groove size. These three specimens were identified as C3D6a, C3D12a and C3D18a.

Then, two more specimens were tested, characterized by a bonded length of $12 d_b$ and two different values of the groove size, namely, 3/4 in. and 1 in. These specimens were identified as C3D12b and C3D12c. The purpose was to examine the effect of the groove size on the test results, particularly on ultimate load and failure mode.

After testing of these two specimens, a groove size of 3/4 in. was identified as the recommendable size for embedment of a No. 3 CFRP deformed rod. Therefore, an additional specimen was tested, with a groove of the “optimum” size and a bonded length

of 24 d_b (specimen C3D24b). A longer bonded length was chosen to obtain more reliable results. In fact, it is generally recognized that, in a bond test, longer bonded lengths are more capable to represent the non-uniform interface conditions and to make negligible the unavoidable end effects.

3.6.2. General Results. Test results in terms of ultimate pull-out load, average bond strength and failure mode are summarized in Table 3.4.

Table 3.4. Test Results for Specimens with CFRP No. 3 Deformed Rods

Spec. Code	Bonded Length (No. of d_b)	Groove Size (in.)	Avg. Concrete Strength (psi)	Ultimate Pull-Out Load (lbs)	Percent. of Ultimate Tensile Load (%)	Avg. Bond Strength (psi)	Failure Mode
C3D6a	6	1/2	4100	3523	18	1329	SOE
C3D12a	12	1/2		6006	20	1133	SOE
C3D12b	12	3/4	4080	6880	23	1298	SOE+C
C3D12c	12	1		6472	22	1221	C
C3D18a	18	1/2	4100	9452	32	1189	SOE
C3D24b	24	3/4	3880	9880	33	932	SOE+C

SOE = Splitting of Epoxy;

C = Concrete Cracking.

A detailed description of the failure modes will be reported in Section 3.6.3. Data recorded from the LVDTs and the strain gages was displayed graphically as already reported in Section 3.6 for the specimens with GFRP rods. First, the load vs. mid-span deflection graph was plotted to check the behavior of the specimen under loading. All diagrams appeared very similar to that shown in Figure 3.12. The only exception was specimen C3D12c which experienced a different failure mode that led to gradual dropping of the load, as shown in Figure 3.22.

3.6.3. Failure Modes. With the only exception of C3D12c, failure occurred for all the specimens by splitting of the epoxy paste in which the NSM rods were embedded, accompanied or not by cracking of the concrete surrounding the groove. During testing, a crackling noise revealed the progressive cracking of the epoxy paste. Eventually, the epoxy cover was completely split and the load suddenly dropped. As in the case of GFRP rods, some differences could be observed as bonded length and groove size were changed.

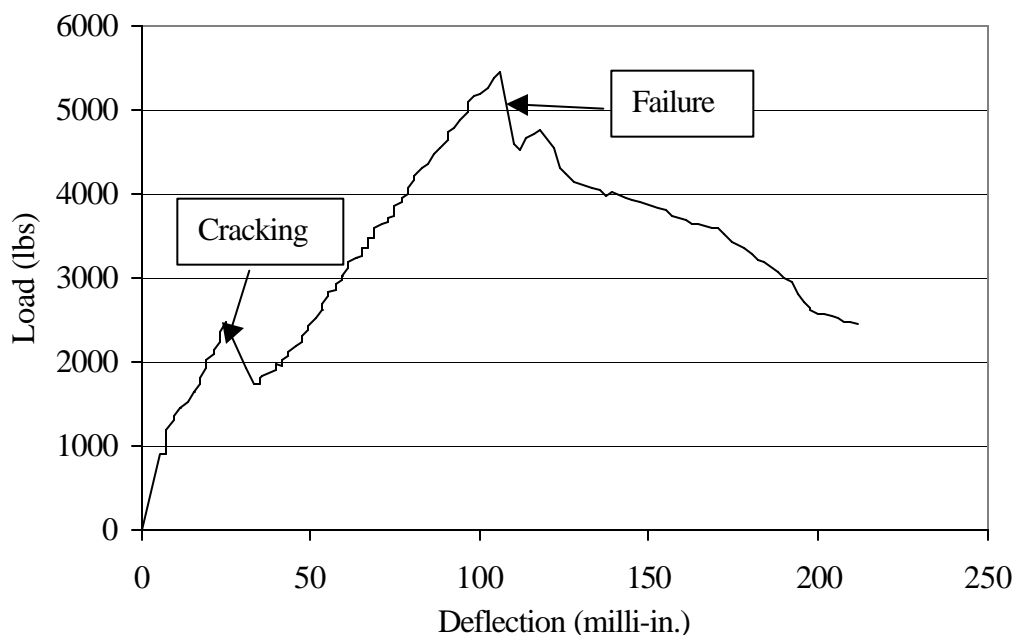


Figure 3.22. Load vs. Mid-Span Deflection for Specimen C3D12c (Failure by Concrete Cracking)

In specimens C3D6a and C3D12a, having the minimum groove size, failure occurred by splitting of the epoxy paste which disintegrated in very small pieces. The aspect of the test side of specimen C3D6a after failure is shown in Figure 3.23. The epoxy cover had been totally split off and no damage was visible in the surrounding concrete. The deformations on the bar surface were also intact.

Very similar was the aspect of specimen C3D18a, having the minimum groove size and a bonded length of 18 bar diameters. In this case, some damage in the concrete surrounding the rod was visible (Figure 3.24).

In specimens C3D12b and C3D24b, due to the larger depth of the groove, a higher level of damage was observed in the concrete at the sides of the groove (Figure 3.25a) and the epoxy cover, rather than disintegrating in very small pieces, appeared as in Figures 3.25-b. In these specimens, inclined and longitudinal splitting cracks formed in the epoxy paste and the inclined cracks propagated in the surrounding concrete (Figure 3.26-a). Also, the rod deformations were sheared off in localized areas (Figure 3.26-b). The level of damage in the rod surface was more limited than in the case of GFRP rods.



**Figure 3.23. Specimen C3D6a
After Failure**



**Figure 3.24. Specimen C3D18a
After Failure**

Only specimen C3D12c, which had the largest groove size, experienced a different mode of failure. Inclined cracks propagated in the concrete surface at one side of the groove (Figure 3.27) and led to a gradual dropping of the load. Visual inspection after failure revealed also the presence of inclined cracks in the epoxy close to the rod loaded end. In this specimen, the cover was thick enough to offer a higher resistance to splitting, so that the controlling failure mechanism shifted to cracking of the surrounding concrete

3.6.4. Free-End Slip Data. Average bond stress vs. free-end slip diagrams were plotted using the data recorded from the LVDT (Figures 3.28 and 3.29). In this case, the rod free end started slipping before failure even in the specimen with the longest bonded length.



(a) (b)
Figure 3.25. Specimen C3D12b After Failure



(a) (b)
Figure 3.26. Specimen C3D24b After Failure

3.6.5. Strain Data. Strain gages were applied at various locations (Figures 3.3 through 3.5) on the surface of the FRP rods. The data from the gages was used to plot strain vs. location graphs, as explained in Section 3.6.5. Figure 3.30 shows a typical strain vs. location diagram.

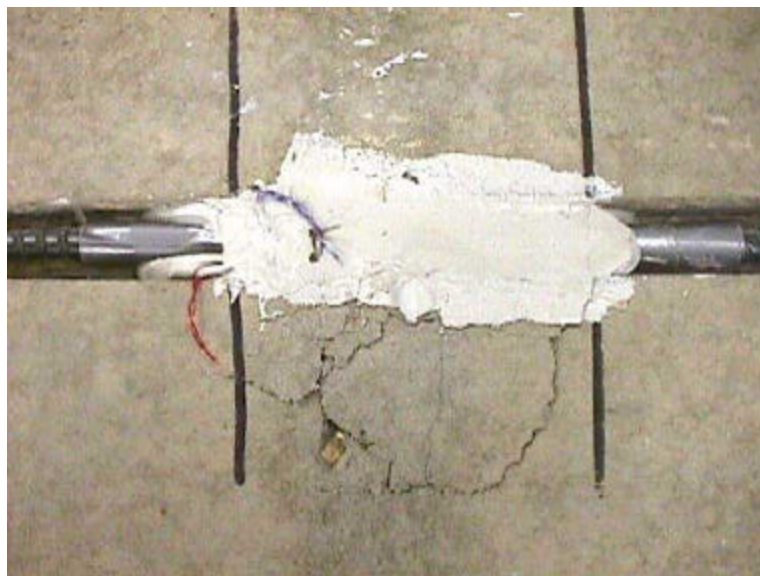


Figure 3.27. Specimen C3D12c After Failure

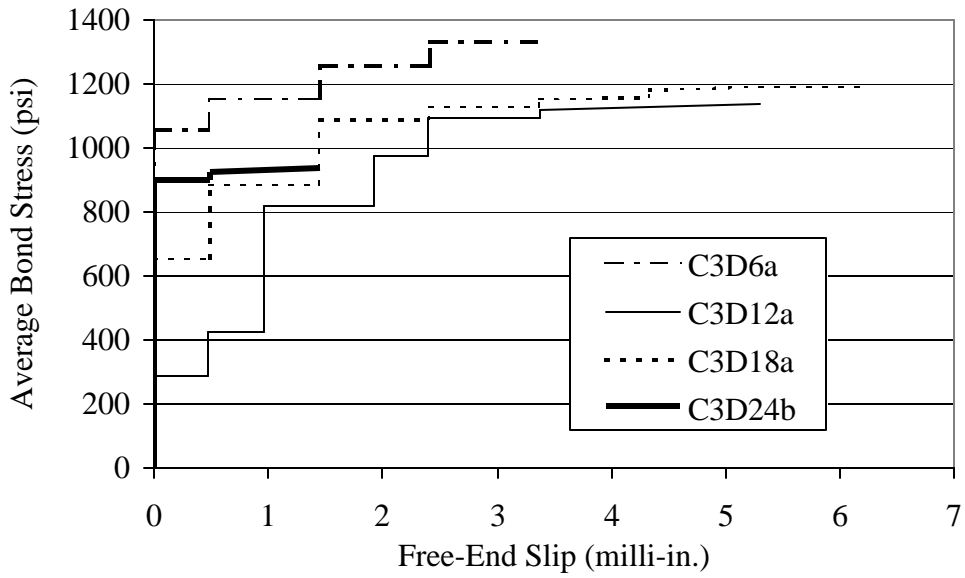


Figure 3.28. Average Bond Stress vs. Free-End Slip for Specimens C3D6a, C3D12a, C3D18a and C3D24b

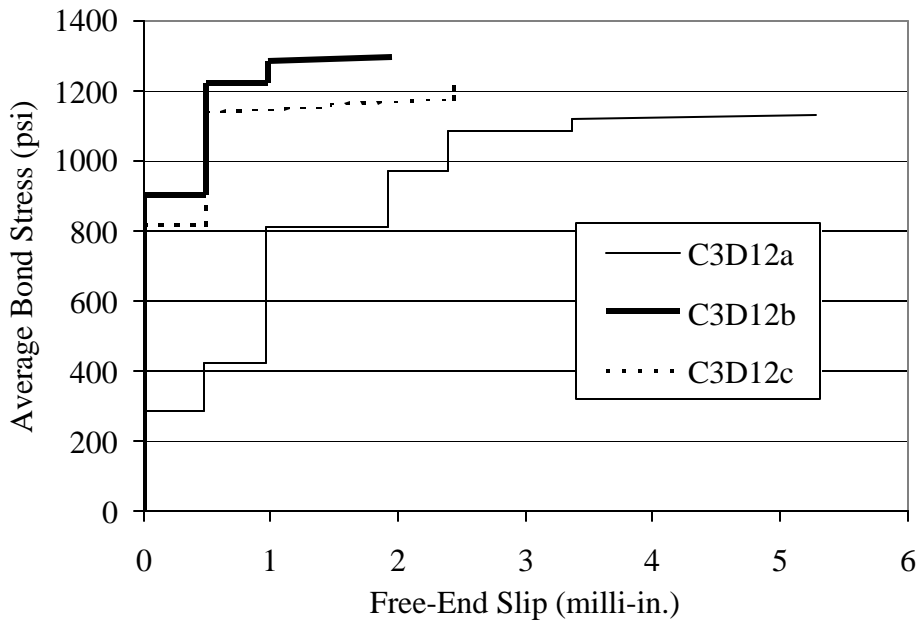


Figure 3.29. Average Bond Stress vs. Free-End Slip for Specimens C3D12a, C3D12b and C3D12c

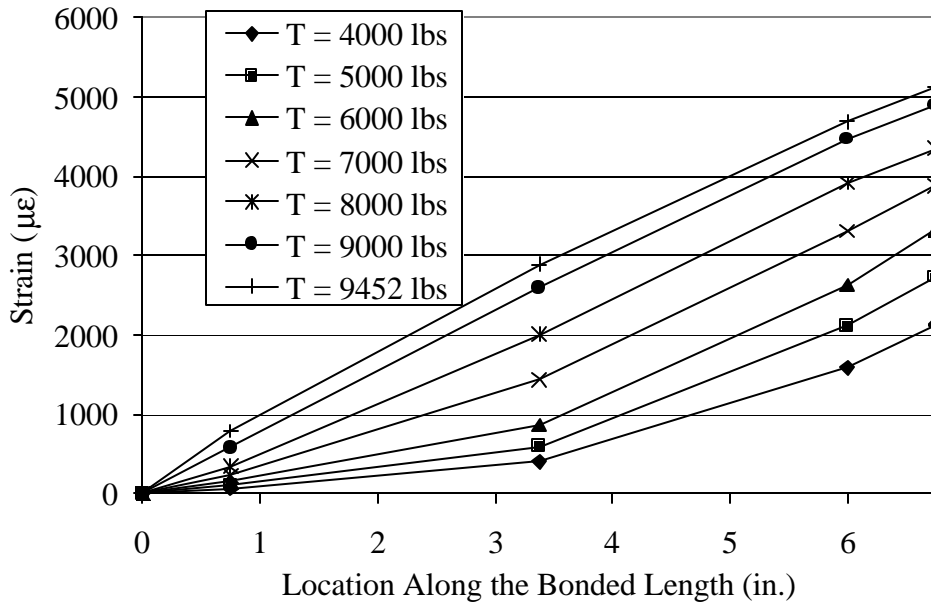


Figure 3.30. Strain vs. Location Diagram for Specimen C3D18a

3.7. EXPERIMENTAL RESULTS FOR SPECIMENS WITH CFRP SANDBLASTED RODS

3.7.1. Introduction. Six specimens with CFRP No. 3 sandblasted rods were tested. The first series consisted of three specimens with the same “minimum” groove size (1/2 in.) and three different bonded lengths (6 d_b , 12 d_b , 18 d_b). These three specimens were identified as C3S6a, C3S12a and C3S18a. Then, two more specimens were tested, with a bonded length of 12 d_b and two different values of the groove size, namely, 3/4 in. and 1 in. These specimens were designated as C3S12b and C3S12c. After testing of these two specimens, it was found that the groove size did not significantly affect results. Therefore, the last specimen, characterized by a bonded length of 24 d_b as for the previous series of tests, had a groove of the “minimum” size (specimen C3S24a).

Four specimens with CFRP No. 4 sandblasted rods were tested, with a groove size of 3/4 in. and four different bonded lengths (6, 12, 18 and 24 d_b). No different groove sizes were investigated, since testing of the specimens with No. 3 rods had shown no influence of the groove size on ultimate load and failure mode.

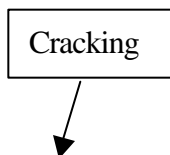
3.7.2. General Results. Test results in terms of ultimate pull-out load, average bond strength and failure mode are summarized in Table 3.5. A detailed description of the failure modes will be reported in Section 3.7.3.

Data recorded from the LVDTs and the strain gages was displayed graphically as previously reported. Two types of load vs. mid-span deflection behavior were observed, depending on the failure mode. For the specimens failed by splitting of the epoxy cover, the load vs. mid-span deflection curve appeared very similar to that shown in Figure 3.12. When failure occurred at the interface between epoxy paste and FRP rod (pull-out), the load dropped to a value smaller than the cracking load and remained constant while deflection kept on increasing until the test was stopped (Figure 3.31). This behavior is due to the presence of friction between the rod and the surrounding paste, which keeps on resisting a certain amount of load even after the other bond-resisting mechanisms are lost. This phenomenon is clearly absent when splitting leads to the total or partial loss of the epoxy cover.

Table 3.5. Test Results for Specimens with CFRP Sandblasted Rods

Spec. Code	Bonded Length (No. of d_b)	Groove Size (in.)	Ultimate Pull-Out Load (lbs)	Avg. Concrete Strength (psi)	Percent. of Ultimate Tensile Load (%)	Avg. Bond Strength (psi)	Failure Mode
C3S6a	6	1/2	2965	4100	12	1119	SOE
C3S12a	12	1/2	3927		16	741	PO
C3S12b	12	3/4	3460	4080	14	653	PO
C3S12c	12	1	3931		16	742	PO
C3S18a	18	1/2	5602	4100	23	704	PO+SOE
C3S24a	24	1/2	5025	3880	20	474	PO+SOE
C4S6a	6	3/4	5082	3960	13	1078	SOE
C4S12a	12	3/4	5839	3880	14	620	PO+SOE
C4S18a	18	3/4	6634		16	469	PO+SOE
C4S24a	24	3/4	7934		20	421	PO+SOE

SOE = Splitting of Epoxy;
PO = Pull-Out.



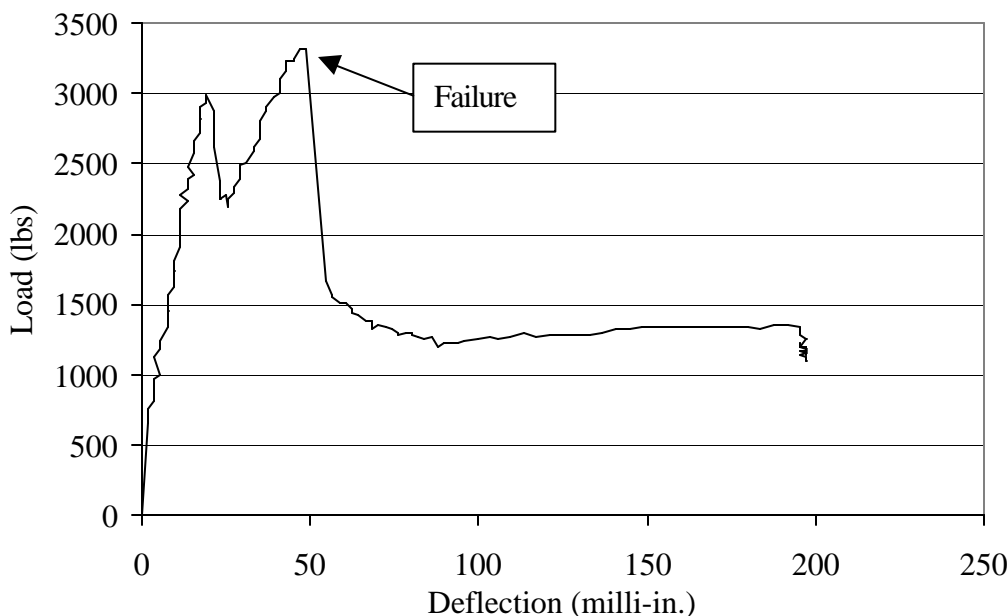


Figure 3.31. Load vs. Mid-Span Deflection for Specimen C3S12a (Failure by Pull-Out)

3.7.3. Failure Modes. Three different failure modes were observed in the specimens with CFRP sandblasted rods. Specimens C3S6a and C4S6a failed by splitting of the epoxy cover, as shown in Figures 3.32-a and 3.33-a. In specimen C3S6a, the epoxy paste disintegrated in small fragments, while the cover of specimen C4S6a broke up in two pieces along a longitudinal splitting crack. Inclined cracks in the epoxy underneath the rod and inclined white lines on the rod surface were visible tracks of the bond stresses (Figures 3.32-b and 3.33-b).

Specimens C3S12a, b and c all failed at the interface between epoxy and CFRP rod. This failure mode has been referred to as “pull-out” in Table 3.5. No sign of damage was visible in the test side of these specimens after failure (Figure 3.34).

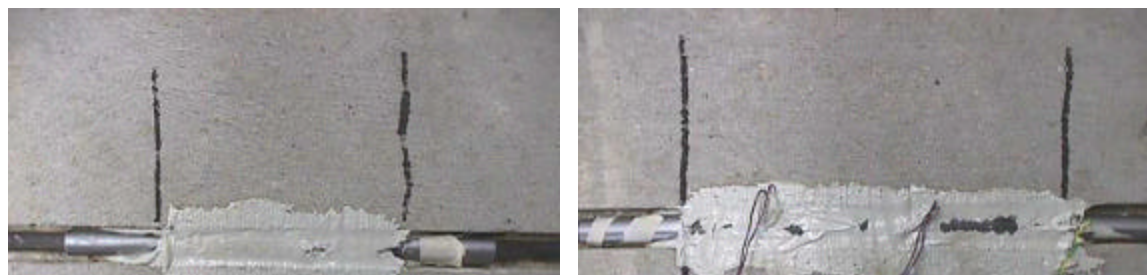
All the other specimens experienced a mixed failure mode between the previous two. After failure, either the epoxy cover appeared partially damaged (C3S18a, Figure 3.35) or a longitudinal splitting crack has developed close to the rod loaded end (C4S12a, Figure 3.36). In the only case of specimen C4S18a, some damage in the concrete was also visible (Figure 3.37).



Figure 3.32. Specimen C3S6a After Failure



Figure 3.33. Specimen C4S6a After Failure



**Figure 3.34. Specimen C3S12a
After Failure**

**Figure 3.35. Specimen C3S18a
After Failure**

3.7.4. Free-End Slip Data. Average bond stress vs. free-end slip diagrams were plotted using the data recorded from the LVDT (Figures 3.38, 3.39 and 3.40). In the specimens with 24-diameter bonded length, no free-end slip was recorded prior to failure.

3.7.5. Strain Data. The data from the strain gages was used to plot strain vs. location graphs, as previously explained. Figure 3.41 shows a typical strain vs. location diagram.

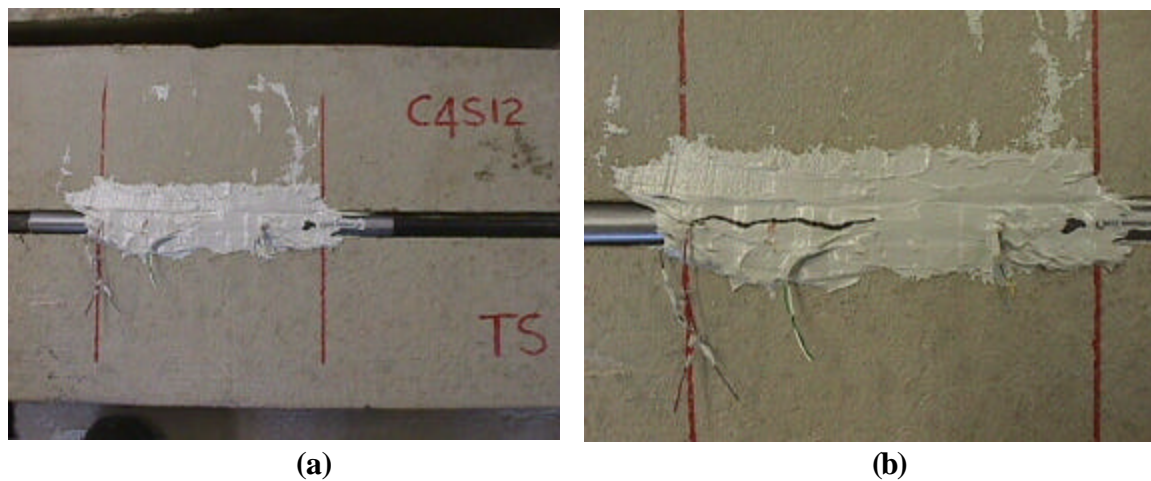


Figure 3.36. Specimen C4S12a After Failure



Figure 3.37. Specimen C4S18a After Failure

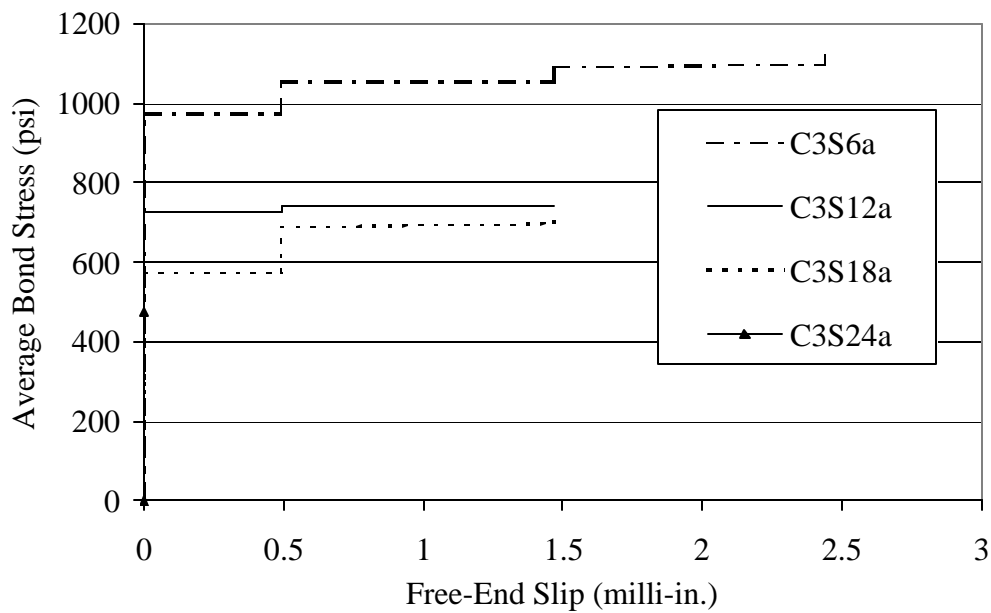


Figure 3.38. Average Bond Stress vs. Free-End Slip for Specimens C3S6a, C3S12a, C3S18a and C3S24a

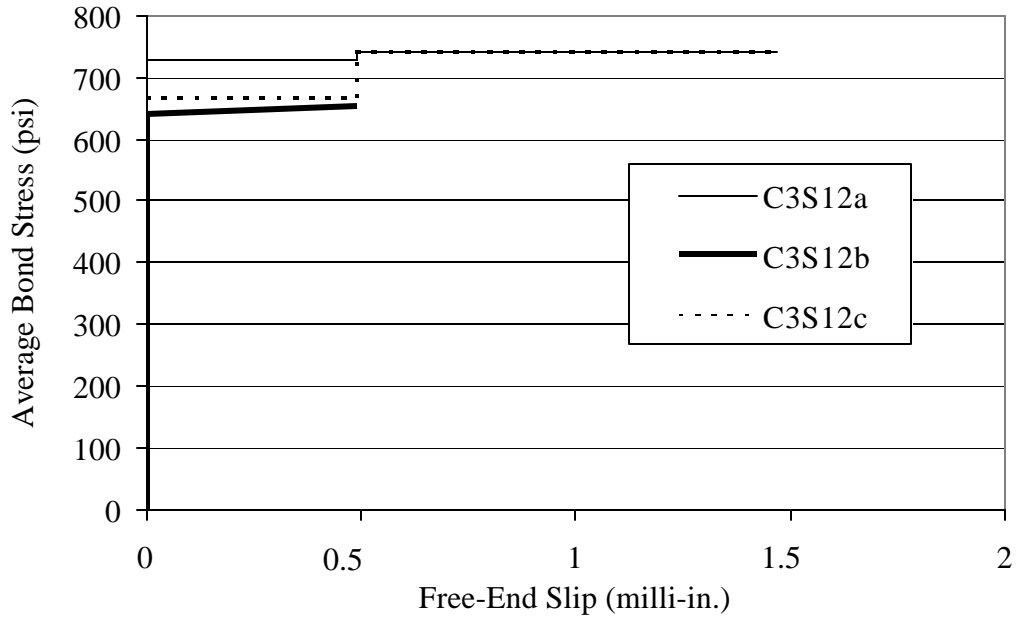


Figure 3.39. Average Bond Stress vs. Free-End Slip for Specimens C3S12a, C3S12b and C3S12c

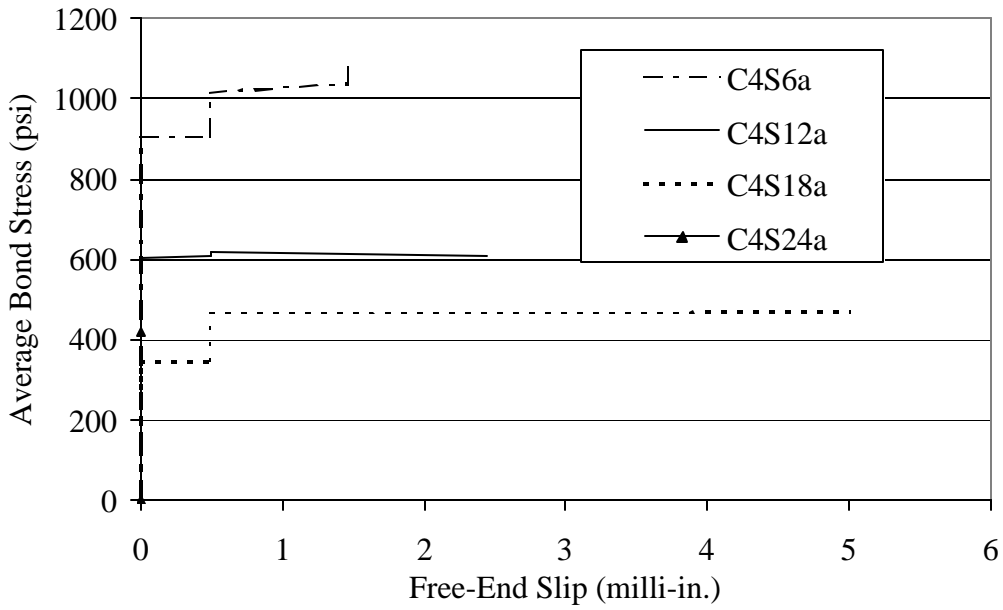


Figure 3.40. Average Bond Stress vs. Free-End Slip for Specimens C4S6a, C4S12a, C4S18a and C4S24a

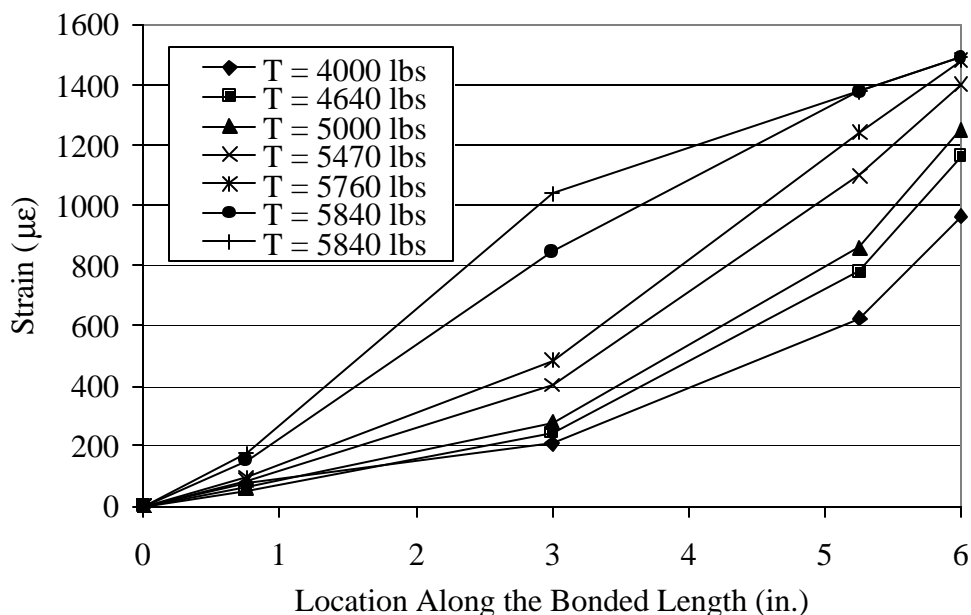


Figure 3.41. Strain vs. Location Diagram for Specimen C4S12a

3.8. DISCUSSION OF TEST RESULTS

3.8.1. Failure Modes. Three different failure modes were experienced during the experimental tests:

- splitting of the epoxy cover;
- cracking of the concrete surrounding the groove;
- pull-out of the FRP rod.

In some cases, a combined failure mode (splitting of the epoxy with cracking of the concrete, pull-out with some damage in the epoxy cover) was observed.

The failure mode by splitting of the epoxy cover is similar in its mechanics to splitting of the concrete cover for reinforcing rods embedded in concrete. Bond stresses have a longitudinal and a radial component, with the latter causing circumferential tensile stresses in the material around the bar. When the maximum tensile stress reaches the tensile strength of the material, the cover splits parallel to the rod. The load at which splitting failure develops is influenced by the surface characteristics of the rods, the tensile strength of the cover material and the thickness of the cover. Also the rod diameter has an

influence on the splitting failure load: according to the model of the thick-walled cylinder for concrete, the significant parameter for the splitting strength is actually the ratio cover thickness to bar diameter (Tepfers, 1979). The cover thickness of NSM rods depends in turn on the depth of the groove in which the rods are embedded.

Epoxy has typically a much higher tensile strength than the concrete: as indicated in Section 2.5, the epoxy paste used in this study has a nominal tensile strength of 2000 psi. However, the cover thickness of NSM reinforcement is very low compared to that of reinforcing bars in concrete, which makes this mode of failure critical for NSM reinforcement.

In specimen C3D12c, failure occurred by cracking of the concrete surrounding the NSM rod. This specimen had the largest value of the ratio cover thickness to rod diameter among all the specimens with deformed rods. In this specimen, the cover was thick enough to offer a higher resistance to splitting, so that the controlling failure mechanism shifted to cracking of the surrounding concrete. It could be observed that, when failure occurs by splitting of the epoxy cover, the ultimate load is expected to be independent from the concrete tensile strength. However, if the groove is deep enough to cause failure occur in the concrete, the concrete tensile strength becomes a significant parameter.

Some of the specimens with sandblasted rods failed by pull-out of the rod. In these cases, the degree of micro-deformation on the surface was not enough to provide mechanical interlocking and the rod was pulled out as soon as adhesion was lost. As previously illustrated (Section 3.7), after failure of these specimens the load dropped to a value smaller than the cracking load but greater than zero, which was due to the existence of friction between the rod and the epoxy.

3.8.2. Crack Pattern. Internal cracks in the epoxy paste were observed in all the specimens after failure. An example is presented in Figure 3.42, which refers to specimen C3S6a. These “secondary” cracks are perpendicular to the direction of the principal tensile stresses. They indicate the trajectories along which the compressive forces leave the surface of the bars and spread out into the concrete. Unlike in the case of reinforcing bars embedded in concrete, in NSM reinforcement these inclined cracks may form not only as secondary cracks in the internal surface of the epoxy paste, but also, due to the small cover thickness, as primary cracks that can lead to bond failure (Figure 3.43).

In the case of smooth rods, when load is first applied the inclination of the principal tensile stresses in the epoxy paste is 45 degrees. When the principal tensile stress reaches the tensile strength of the material, this angle changes and a radial stress between the rods and the surrounding material develops. In the case of deformed rods, radial stresses develop as soon as the deformations on the rod surface are brought into bearing. In both situations, the radial stress is balanced by circumferential tensile stresses which may lead to longitudinal splitting cracks, as shown in Figure 3.44 which is related to specimen C3D24b.



Figure 3.42. Internal Cracks in Specimen C3S6a



Figure 3.43. Crack Pattern in Specimen G4D24c After Failure



Figure 3.44. Crack Pattern in Specimen C3D24b After Failure

3.8.3. Effect of the Surface Configuration. Among the two different rod surface conditions examined in this experimental study, deformed and sandblasted, the former appeared to have a greater tendency to induce splitting failure, as expected. Since deformations on the rod surface increase the resistance of the rod to pull-out, the principal tensile stress becomes the controlling factor.

In the case of sandblasted rods, failure occurred in some specimens by pull-out, as previously stated. However, even in absence of macro-deformations on the rod surface, some splitting failures or mixed modes of failure (pull-out with some damage in the epoxy) were observed. This showed that sandblasting is effective in increasing the resistance of the rod to pull-out, so that splitting becomes the controlling mechanism.

Comparing the average bond strength of specimens with CFRP deformed and sandblasted rods having the same values of all the remaining parameters, it can be concluded that deformed rods are more efficient than sandblasted rods from the standpoint of the bond performance. The average bond strength of specimens C3D6a, C3D12a and C3D18a was higher than that of specimens C3S6a, C3S12a and C3S18a by 18.8%, 52.9% and 68.9%, respectively. The reason why this difference increases with the bonded length is that the average bond strength is approximately constant in the former specimens and decreases with increasing bonded length in the latter. This in turn depends on the distribution of the bond stresses along the bonded length at ultimate, uniform in the case of deformed rods and non-uniform in that of sandblasted rods.

3.8.4. Effect of the Groove Size. When failure was by splitting of the epoxy cover, increasing the groove size led to a higher bond strength. For specimens G4D12, the ultimate load increased 8% and 24% as the groove size increased from 5/8 in. to 3/4 in. and 1 in., respectively. For the specimens C3D12, the ultimate load increased 15% and 8% as the groove size increased from 0.5 in. to 3/4 in. and 1 in., respectively. The smaller increase in the second case corresponded to a different mode of failure, as previously discussed. As the groove size increases, the thickness of the epoxy cover increases, so offering a higher resistance to splitting. The ultimate load increases correspondingly, and failure may eventually shift from the epoxy to the surrounding concrete.

For specimens C3S12, increasing the groove size did not influence the failure load, since pull-out was the controlling mechanism. However, in specimens with longer bonded lengths splitting cracks developed and accelerated pull-out failure. Therefore, it is expected that increasing the groove size would have been beneficial also for specimens with sandblasted rods.

From the experimental results involving different groove sizes, the optimum groove sizes appear to be 3/4 in. and 1 in. for embedment of NSM rods No. 3 and No. 4,

respectively. This conclusion is based on testing of specimens with deformed rods. The effect of the groove size for specimens with sandblasted rods and bonded lengths greater than 12 rod diameters needs to be investigated.

3.8.5. Effect of the Bonded Length. The ultimate load increased, as expected, with the bonded length of the rod. For the specimens with GFRP No. 4 deformed and CFRP sandblasted rods, the average bond strength was found to decrease as the bonded length increased. On the contrary, for specimens with CFRP No. 3 deformed rods, the average bond strength resulted approximately constant with the bonded length, which indicates an even distribution of bond stresses along the bonded length at ultimate. This can be verified by means of the strain data obtained from the strain gages. Figure 3.30 presents the strain distribution along the bonded length in specimen C3D18a at different load levels. At ultimate, the strain varies almost linearly along the entire bonded length, which means that the bond stress has a constant value throughout.

In engineering applications, the bond stress generally is regarded as uniformly distributed along the bond length. However, the stress varies along the bond length. The nominal (average) bond stress is always an average of the maximum value over a short length, a reduced value over the portion where the slip has occurred, and, at lower loads, a zero stress over a portion of the length. This variation is very pronounced at low loads and increases with the bond length. The shorter the specimen, the more nearly the average bond stress approaches the ultimate value in adhesion; the longer the specimen, the lower is the average bond stress which can be obtained. At higher loads, the bond properties change in such a way as to approach a uniformly distributed bond stress. In the particular case of deformed bars, the slip near the loaded end gradually brings the lugs into bearing and thus raises the average bond stress. When principal tensile stresses are critical on the bond performance, there also may occur longitudinal cracking which increases the compliance of the bond between the bar and the surrounding material, thus enhancing uniform distribution of bond stress. However, the bond forces may split away the portion of the cover close to the rod loaded end (where the bond stress reaches the maximum value), without attaining the level at which the bond stresses become uniformly distributed. The average bond strength obtainable then decreases sharply with increase in length.

Redistribution of bond stresses as a result of splitting cracks happened in specimens with CFRP No. 3 deformed rods, that had larger values of the ratio between cover thickness and rod diameter. As a result, the average bond strength turned out to be approximately constant with the bonded length. In the case of specimens with GFRP No. 4 deformed rods, only partial redistribution of stresses could occur prior to failure. Similarly for sandblasted rods, failure occurred by either pull-out or a combination of pull-out and splitting, which did not allow for redistribution of the bond stresses along the whole bonded length prior to failure. Therefore, the bond stresses were not uniformly distributed at failure.

3.9. CONCLUSIONS

The following conclusions can be drawn from the experimental investigation on bond of NSM FRP reinforcement in concrete:

- the bond test method adopted in this experimental program appears to be an efficient protocol for investigation of bond. It gives reliable data while maintaining a manageable specimen size. Furthermore, specimen details as the saw cut and the top hinge at mid-span allow to analyze the data with accuracy. It is suggested as a possible new standard test method;
- three different failure modes were experienced during the experimental tests, namely, splitting of the epoxy cover, cracking of the concrete surrounding the groove and pull-out of the FRP rod. In some cases, combined failure modes were registered;
- the surface condition of the FRP rods influences the bond strength. Deformed rods appear to be more efficient than sandblasted rods from the standpoint of the bond performance;
- increasing the groove size, and thus the cover thickness, leads to higher bond strength when failure is controlled by splitting of the epoxy cover. Conversely, it does not have any effect when pull-out failure occurs;
- the only specimen that failed by cracking of the concrete surrounding the groove had the largest value of the ratio cover thickness to rod diameter among all the

specimens with deformed rods. When failure occurs by splitting of the epoxy cover or by pull-out of the rod, the ultimate load is expected to be independent from the concrete tensile strength. However, if the groove is deep enough to cause failure occur in the concrete, the concrete tensile strength becomes a significant parameter;

- from the experimental results involving different groove sizes, the optimum groove sizes appear to be 3/4 in. and 1 in. for embedment of NSM rods No. 3 and No. 4, respectively. This conclusion is based on testing of specimens with deformed rods. The effect of the groove size for specimens with sandblasted rods having bonded lengths greater than 12 rod diameters needs to be investigated;
- the distribution of bond stresses at ultimate is not uniform, except for the case of specimens with CFRP No. 3 deformed rods. Therefore, the development length has to be calculated by solving the differential equation of bond with the local bond stress – slip relationship of the NSM rods.

4. BOND OF NSM FRP RODS IN MASONRY

4.1. INTRODUCTION

4.1.1. Background and Problem Statement. Failure of masonry structures can be caused by structural weakness or overloading, dynamic vibrations, settlement, and in-plane and out-of-plane deformations. While most of the research conducted on the use of FRP composites has focused on the retrofitting and repairing of RC structures, current literature on masonry indicates that each of these causes can be prevented and lessened by using FRP composites. In previous works dealing with the use of FRP laminates, variables such as loading configurations/mechanisms, strengthening schemes, and anchorage systems have been evaluated (Hartley et al., 1996; Schwegler and Kelterborn, 1996; Velazquez, 1998).

Unreinforced masonry (URM) walls can be either load bearing or non-load bearing (infill) walls. Due to weak anchorage to adjacent concrete members (load bearing walls), or due to the absence of anchorage (infill walls), these walls may fail and collapse under out-of-plane loads generated by seismic forces. In URM walls, failure due to out-of-plane bending causes the majority of the material damages and loss of human life (TMS, 1994). Therefore, the development of effective strengthening techniques needs to be addressed.

Previous works on URM masonry walls strengthened with FRP laminates have shown remarkable increases in capacity and ductility. The fact that the anchorage of NSM rods into adjacent RC members (i.e. slabs, columns and beams) is a feasible task, makes attractive their use for increasing the flexural strength of masonry walls.

4.1.2. Objective. The objective of this section of the experimental program was to investigate bond between NSM FRP rods and concrete masonry blocks. Two different types of FRP rods, namely, CFRP sandblasted and GFRP deformed, were examined. The diameter of the rods was 3/8 in. (No. 3) and the size of the groove was 3/4 in. These test parameters were chosen taking into account the dimensions of the standard concrete blocks, already reported in Section 2.6. A groove size of 3/4 in. is believed to be the largest that can be possibly adopted without creating excessive damage in the blocks. For the same reason, it was decided to use only No. 3 rods.

4.2. DESCRIPTION OF THE SPECIMENS

Each specimen consisted of two standard hollow concrete blocks. The dimensions of the blocks have been already reported in Section 2.6 of this document. One NSM FRP rod was applied to each face of the blocks in the longitudinal direction, connecting the two blocks together.

Only one block was the test region, with the NSM FRP rod having a limited bonded length and being unbonded in the remaining part. Length and position of the bonded part were the same for both faces of the test block. The rod was fully bonded on the other block, to cause bond failure to occur in the test region.

In each block, the hole closer to the face where the load had to be applied was grouted with pre-mixed concrete, so to prevent crushing of the block face before failure of the bond.

Two different types of FRP rods, namely, CFRP sandblasted and GFRP deformed, were examined. The diameter of the rods was 3/8 in. (No. 3) and the size of the groove was 3/4 in. For each type of FRP rod, specimens with three different values of the bonded length were tested, equal to 6, 12 and 18 times the rod diameter. Table 4.1 presents the test matrix indicating the designation that will be used to identify the specimens. The specimen designation refers to the following parameters: type of FRP material – rod surface configuration – bonded length. As an example, CS18 refers to a specimen with a CFRP sandblasted rod, having a bonded length of 18 times the rod diameter.

Table 4.1. Description of the Specimens

Specimen Designation	Rod Size (No.)	Type of FRP Rod	Surface Configuration	Bonded Length (No. of d_b)
CS6	3	Carbon	Sandblasted	6
CS12				12
CS18				18
GD6	3	Glass	Deformed	6
GD12				12
GD18				18

4.3. SPECIMEN PREPARATION

The preparation of the specimens included: application of strain gages on the FRP rods, cutting of longitudinal grooves on the sides of the concrete blocks, grouting of the holes and positioning of the rods.

4.3.1. Application of Strain Gages. Strain gages were applied on the surface of the FRP rods prior to their application. The purpose was to monitor the strain distribution along the rod during the test. All the strain gages had a gage length of 1/2 in. to ensure localized strain measurement. The application of strain gages on the deformed rods required the removal of the surface deformations in the spots where the gages had to be placed. In each of these spots, two ribs were removed by means of a belt sander.

No strain gages were applied to the specimens with a bonded length of six diameters. On a short bonded length, the presence of strain gages would have significantly influenced the bond behavior, especially in the case of deformed rods where the superficial properties had to be modified prior to their application.

Figures 4.1 and 4.2 indicate the location of the strain gages on the FRP rods for the 12-diameters and 18-diameters bonded lengths. Three strain gages were placed within the bonded length and an additional one was applied in the unbonded region.

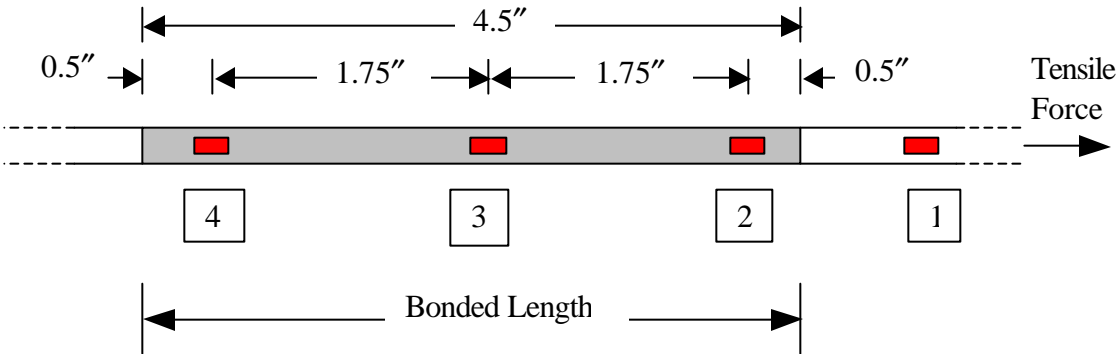


Figure 4.1. Position of the Strain Gages (Rods No. 3, Bonded Length 12 d_b)

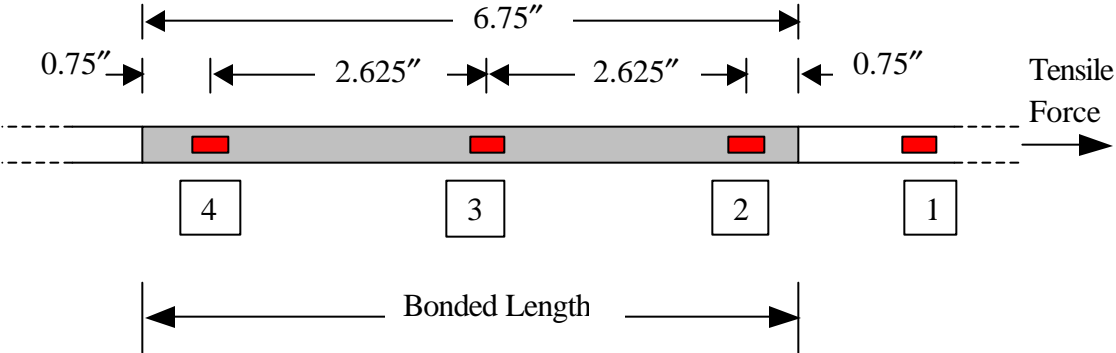


Figure 4.2. Position of the Strain Gages (Rods No. 3, Bonded Length $18 d_b$)

4.3.2. Cutting of the Grooves. Each of the specimens had two grooves cut on the two sides and oriented along the longitudinal axis, where the FRP rods had to be mounted. The grooves were cut using a concrete saw (Figure 4.3). All of them had square cross-section, with size of $3/4$ in.



Figure 4.3. Cutting of the Grooves on the Concrete Blocks

4.3.3. Application of the Grout. In each block, the hole closer to the face where the load had to be applied was grouted with Ash Grove pre-mixed concrete to prevent crushing of the block face before failure of the bond.

4.3.4. Application of the NSM Rods. Figure 4.4 shows some specimens before application of the rods. The grooves were air blasted to remove loose particles produced by the cutting process. Then the epoxy paste was prepared by mixing the two components (resin and

hardener) in 2:1 proportion by volume with a power mixer. The groove was filled half-way with the paste (Figure 4.5-a), the rod was then placed in the groove and lightly pressed (Figure 4.5-b). This forced the paste to flow around the bar and fill completely between the bar and the sides of the groove. The groove was then filled with more paste and the surface was leveled (Figure 4.5-c). Figure 4.5-d shows one side of the test block after preparation.



Figure 4.4. Concrete Blocks Before Preparation

4.4. TEST PROCEDURE

The test bed was a steel plate with dimensions 5 ft. by 2 ft. and thickness of 1/8 in. Five steel angles were bolted on the plate to delimitate the position where the concrete blocks had to be placed. The purpose of the plate was to ensure the proper positioning of the specimens during preparation and testing. A plastic sheet was placed between the plate and the bottom surface of the blocks, in order to minimize the friction between the two surfaces during testing.

The epoxy paste was allowed to cure for 15 days (full cure time at room temperature) prior to testing of the specimens. Load was applied by means of a 12-ton hydraulic jack connected to an hydraulic pump. The jack was placed horizontally between the two blocks, as indicated in Figure 4.6. Load was recorded by means of a Sensotek pressure transducer connected to the hydraulic jack. Slip at the end of the FRP rods in the test region was measured using two LVDTs. Load, slip

and strains were all recorded with a one-Hertz sampling rate by a LABTECH data acquisition system. Figures 4.7 through 4.9 illustrate the test setup.

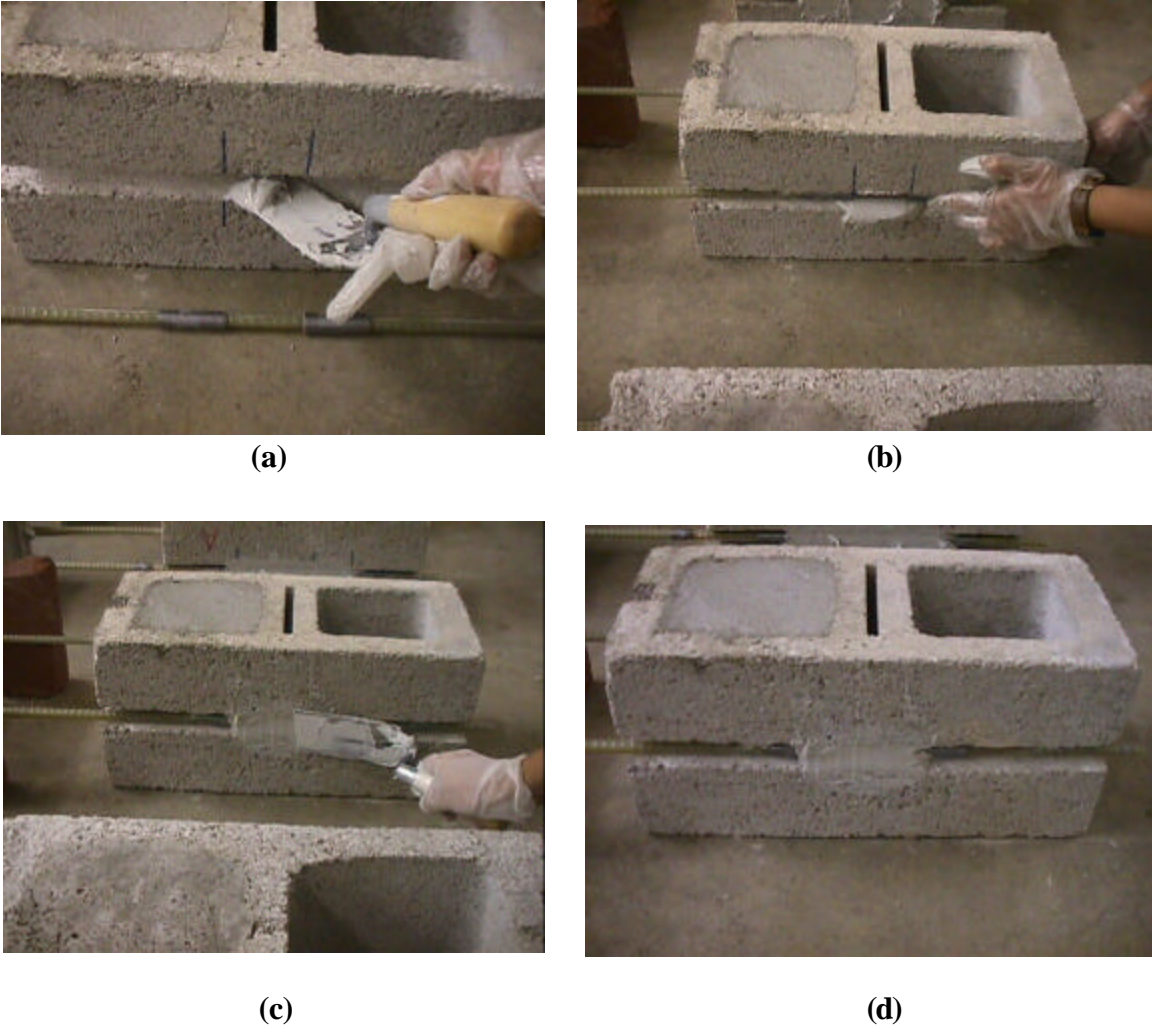


Figure 4.5. Specimen Preparation

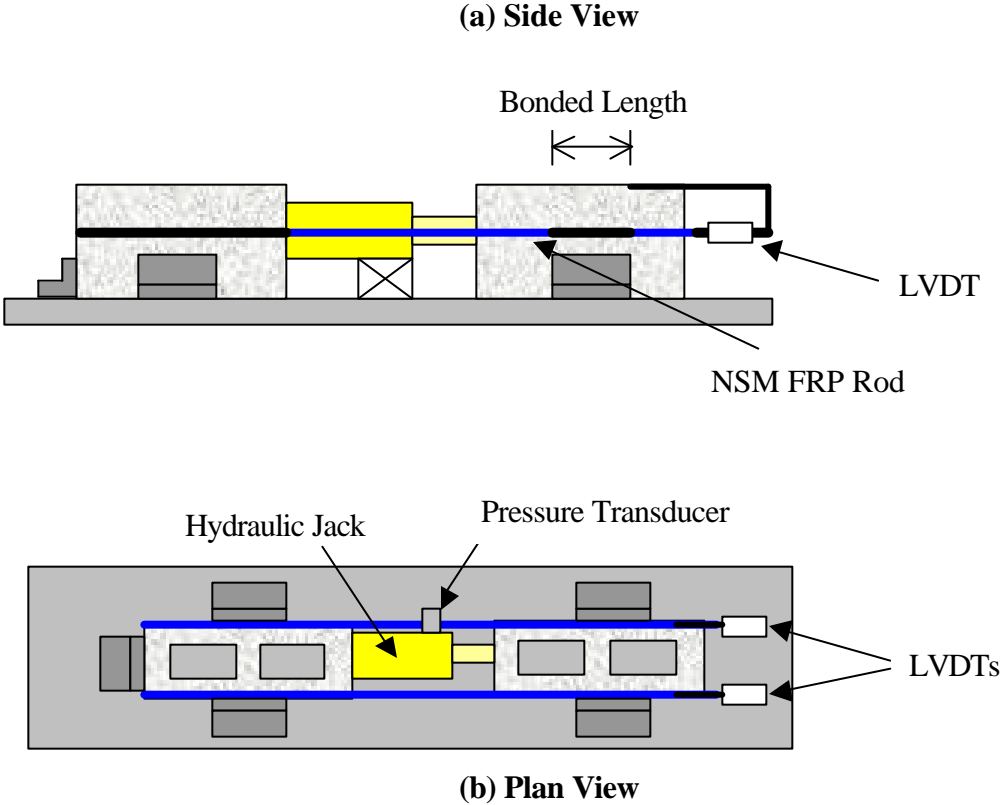


Figure 4.6. Scheme of the Test Setup



Figure 4.7. Test Setup



Figure 4.8. Detail of Hydraulic Jack and Pressure Transducer



Figure 4.9. Detail of the LVDTs

4.5. EXPERIMENTAL RESULTS

4.5.1. General Results. Test results in terms of ultimate load, average bond strength and failure mode are summarized in Table 4.2. The value of the ultimate load was obtained dividing by two the maximum load applied to the specimen by means of the hydraulic jack. The average bond strength was calculated using Equation 4.1:

$$t_{bu} = \frac{T_u}{p \cdot d_b \cdot l_b} \quad (4.1)$$

where T_u is the ultimate load, d_b the nominal diameter of the rod and l_b the bonded length.

Table 4.2. Test Results

Specimen Code	Ultimate Pull-Out Load (lbs)	Percentage of Ultimate Tensile Load (%)	Average Bond Strength (psi)	Failure Mode
CS6	2954	12	1114	PO
CS12	3303	13	623	PO
CS18	4082	16	513	PO
GD6	3491	26	1317	SOE+C
GD12	3759	28	709	SOE+C
GD18	6069	46	763	SOE+C

PO = Pull-Out;
 SOE = Splitting of Epoxy;
 C = Concrete Cracking.

4.5.2. Modes of Failure. As indicated in Table 4.2, two different failure modes were observed. In the specimens with deformed rods, failure occurred by splitting of the epoxy paste in which the NSM rods were embedded, accompanied by cracking of the concrete surrounding the groove. During testing, a crackling noise revealed the progressive cracking of the epoxy paste. Eventually, the epoxy cover was completely split and the load suddenly dropped. The concrete material surrounding the groove was also damaged, as shown in Figure 4.10.

Specimens with CFRP sandblasted rods all failed at the interface between epoxy and CFRP rod. This failure mode has been referred to as “pull-out” in Table 4.2. No sign of damage was visible in the test side of these specimens after failure (Figure 4.11).



Figure 4.10. Specimen After Splitting Failure

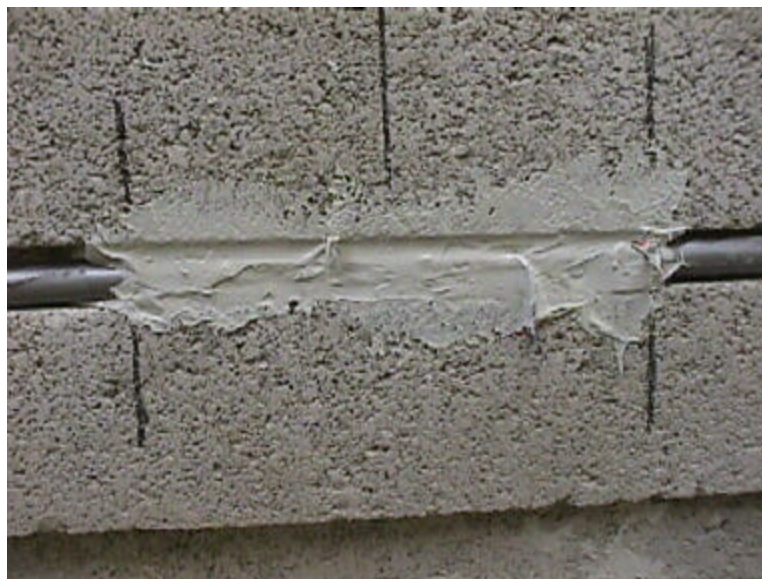


Figure 4.11. Specimen After Pull-Out Failure

4.5.3. Free-End Slip Data. Slip at the free end of the rods in the test side was measured by means of two LVDTs. No free-end slip prior to failure was recorded for any of the specimens, with the only exception of GD6. For this specimen, the average bond stress vs. free-end slip curves obtained by the two LDVTs are reported in Figure 4.12. The curves do not coincide due to the non perfect distribution of the applied load among the two rods on the two sides of the blocks.

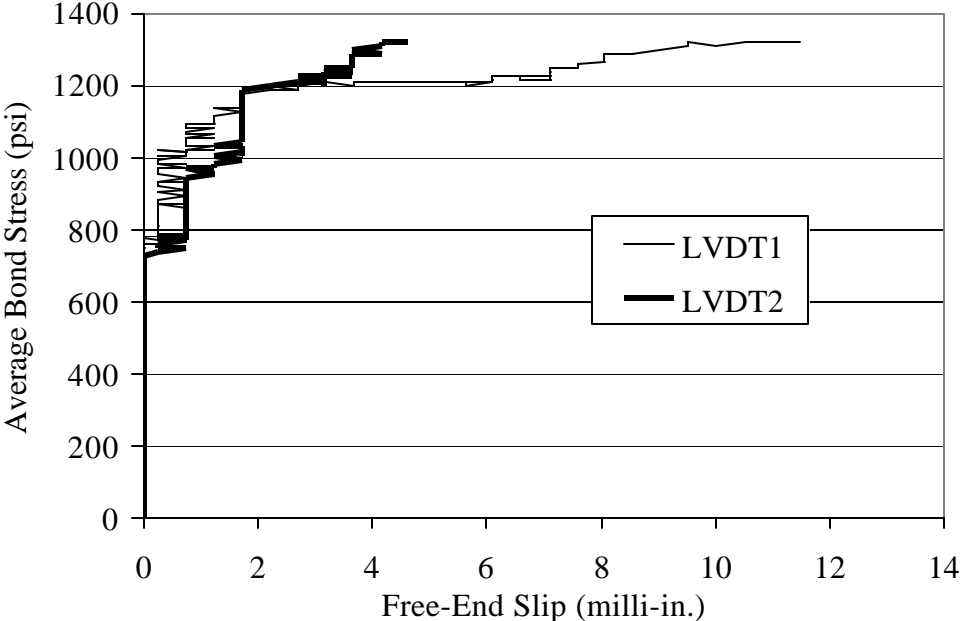


Figure 4.12. Average Bond Stress vs. Free-End Slip for Specimen GD6

4.5.4. Strain Data. Strain gages were applied at various locations (Figures 4.1 and 4.2) on the surface of the FRP rods to monitor the strain distribution along the rod during the test. A typical pull-out load vs. strain diagram is shown in Figure 4.13. The strain gages are numbered starting from the one in the unbonded region and proceeding toward the rod free end.

The data from the strain gages was used to plot strain vs. location graphs. In these graphs, the strain in the rod along the bonded length is plotted for different values of the pull-out load. All points were obtained from the readings of the strain gages, except for the strain at the end of the bonded length, which was assumed to be equal to zero. Figure 4.14 shows a typical strain vs. location diagram. The left end (location equal to zero) and the right end of the x axis correspond to the free end and to the loaded end of the bonded length, respectively.

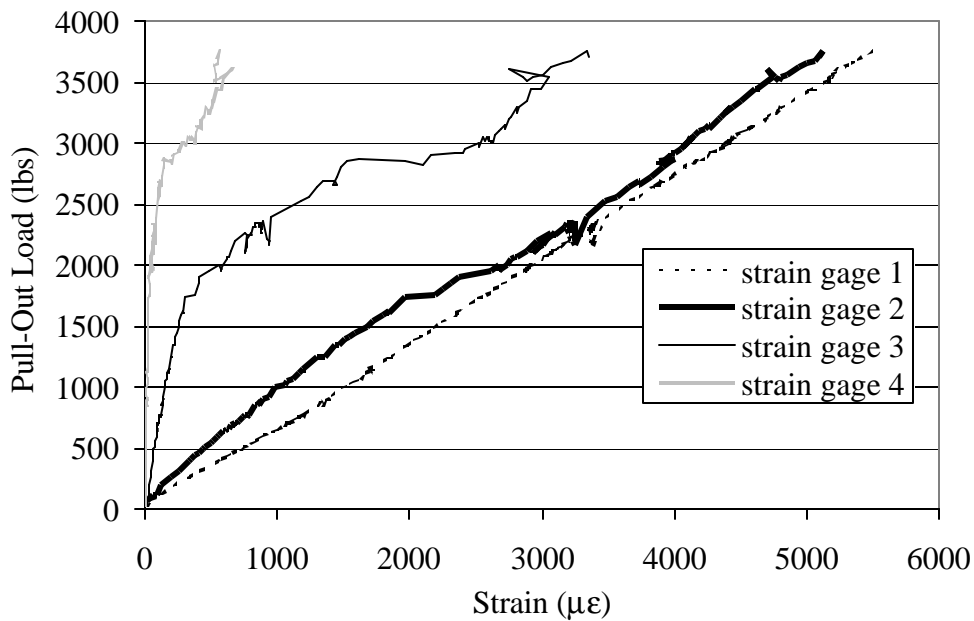


Figure 4.13. Pull-Out Load vs. Strain for Specimen GD12

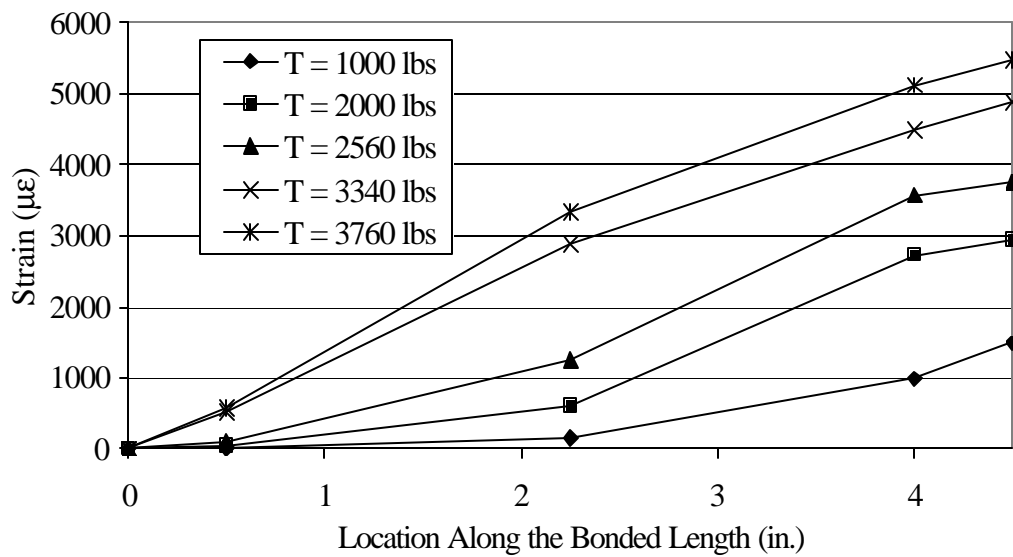


Figure 4.14. Strain vs. Location Diagram for Specimen GD12

4.6. DISCUSSION OF TEST RESULTS

Two different failure modes were experienced during the experimental tests:

- splitting of the epoxy cover accompanied by concrete cracking for specimens with GFRP deformed rods;
- pull-out of the rod for specimens with CFRP sandblasted rods.

The same considerations reported in Section 3.9 of this document for bond of NSM rods in concrete apply to bond of NSM rods in concrete masonry blocks. The failure mode by splitting of the epoxy cover is similar in its mechanics to splitting of the concrete cover for reinforcing rods embedded in concrete. As already outlined in Section 3.8, bond stresses have a longitudinal and a radial component, with the latter causing circumferential tensile stresses in the material around the bar. When the maximum tensile stress reaches the tensile strength of the material, the cover splits parallel to the rod. Unlike in the case of NSM rods in concrete, a noticeable level of damage was always induced in the portion of block surrounding the groove along with splitting of the epoxy cover, due to the lower tensile strength of the concrete masonry material with respect to the concrete used for the tests described in Section 3.

The specimens with sandblasted rods failed by pull-out of the rod. In these cases, the degree of micro-deformation on the surface did not provide sufficient mechanical interlocking and the rod was pulled out as soon as adhesion was lost.

The ultimate load increased, as expected, with the bonded length of the rod, but the average bond strength was found to decrease when the bonded length increased, as a result of the non uniform distribution of the bond stresses. Therefore, the local τ – slip relationship is needed in order to solve all problems related to the bond behavior, particularly, to calculate the development length of NSM FRP rods.

4.7. CONCLUSIONS

The following conclusions can be drawn from the experimental investigation on bond of NSM FRP reinforcement in concrete masonry blocks:

- two different failure modes were experienced during the experimental tests, namely, splitting of the epoxy cover combined with concrete cracking for the specimens with GFRP deformed rods and pull-out for those with CFRP sandblasted rods;

- unlike in the case of NSM rods in concrete, a noticeable level of damage was always induced in the portion of block surrounding the groove along with splitting of the epoxy cover, due to the lower tensile strength of the concrete masonry material;
- the distribution of bond stresses at ultimate is not uniform. Therefore, the development length has to be calculated by solving the differential equation of bond with the local bond stress – slip relationship of the NSM rods.

5. SHEAR STRENGTHENING OF RC BEAMS WITH NSM FRP RODS

5.1. INTRODUCTION

5.1.1. Background and Problem Statement. Shear failure of RC members is catastrophic and occurs with no advance warning of distress. In order to take full advantage of the ductility of an RC member, it is desirable to ensure that flexure rather than shear governs ultimate strength. Existing RC beams have been sometimes found to be deficient in shear and in need of strengthening. Deficiencies can occur as a result of several factors, such as insufficient shear reinforcement resulting from design or construction errors or use of outdated codes, reduction in the steel area due to corrosion, and increase in demand of service load.

In the last few years, it has been experimentally observed that externally bonded FRP laminates may be used to increase the shear capacity of reinforced concrete beams (Khalifa, 1999). Although only few studies have specifically addressed shear strengthening, the experimental tests carried out showed that even small amounts of FRP external reinforcement can provide considerable safety against brittle shear failures. Many different FRP shear reinforcement configurations can be used: continuous reinforcement, series of strips, configurations with mechanical anchorage. The fibers can be perpendicular to the beam axis or oriented at 45 degrees to best reinforce shear cracks, or it may be convenient to create pseudo-isotropy by orienting the fibers in two perpendicular directions.

The effectiveness of the strengthening reinforcement, that is, the ultimate load carried by the FRP, depends on its failure mechanism. As experimental tests showed, failure of the FRP reinforcement may occur either by peeling-off (debonding) at the concrete-FRP interface, or by tensile fracture at a stress which may be lower than the tensile strength of the composite material, because of stress concentrations (e.g. at rounded corners or at debonded areas). Which of the two mechanisms will occur depends on many factors, particularly on the bond conditions, the type of attachment at the FRP ends and others. In many cases, the actual failure mechanism is a combination of FRP debonding at certain areas and fracture at others.

As an alternative to externally bonded FRP laminates, NSM FRP rods can be used for shear strengthening of RC beams. This technique involves cutting vertical or inclined grooves on the side surfaces of the beam and embedding the FRP rods in the epoxy-filled grooves. The advantage of NSM rods with respect to FRP laminates in this application is that no surface preparation is required

in the former case, as opposed to the case of externally bonded laminates where adequate bond to the concrete surface has to be ensured to achieve an effective strengthening system.

Currently, there is no literature available on the shear reinforcement of RC beams using NSM rods. As this new technology emerges, an investigation on its possible applications is needed. The effectiveness of NSM FRP rods for shear strengthening of RC beams needs to be evaluated, in order to verify if this technique can represent a valid alternative to externally bonded FRP sheets.

5.1.2. Objective. The objective of this section of the experimental program was to evaluate the effectiveness of NSM FRP rods for the shear strengthening of RC beams. Eight full-scale RC beams with T-shaped cross-section were tested to investigate their performance and modes of failure. Some variables expected to influence the performance of the strengthening system were addressed, namely, spacing of the rods, inclination of the rods, end anchorage and presence of internal steel stirrups.

5.2. DESCRIPTION OF THE SPECIMENS

This part of the experimental program involved testing of eight full-scale RC beams with a T shaped cross-section and a total length of 10 ft. Six beams had no internal shear reinforcement. Two beams had internal steel stirrups at a spacing that did not satisfy the requirements of the ACI 318-95 Code (American Concrete Institute, 1995). The amount of steel flexural reinforcement was the same for all the beams and was designed in order to obtain a shear failure in spite of the envisioned shear capacity enhancement provided by NSM FRP rods. As a result, the beams had a flexural reinforcement of 2 steel rebars No. 9 (nominal area of 1.00 in²). The dimensions of the beam cross-section are given in Figure 5.1.

The specified concrete strength was 5000 psi. The actual concrete strength was determined as the average of three compression tests on standard concrete cylinders, as already indicated in Section 2.2. The actual concrete strength on the test day resulted to be 4560 psi. The internal steel flexural reinforcement was Grade 60, that is, had a nominal yield strength of 60 ksi. The actual yield strength as determined from standard tensile test of three specimens was 62.7 ksi. The internal steel shear reinforcement was Grade 50, with a nominal yield strength of 50 ksi. The actual yield strength as determined from standard tensile test of three specimens was 50.0 ksi.

The specimen details are indicated in Table 5.1 together with the identification codes to be used in the following.

Table 5.1. Description of the Specimens

Beam Code	Steel Stirrups		NSM FRP Rods			
	Arms/Size	Spacing (in.)	Arms/Size	Spacing (in.)	Angle (°)	Anchorage in the Flange
BV	-	-	-	-	-	-
B90-7	-	-	2 No.3	7	90	NO
B90-5	-	-	2 No.3	5	90	NO
B90-5A	-	-	2 No.3	5	90	YES
B45-7	-	-	2 No.3	7	45	NO
B45-5	-	-	2 No.3	5	45	NO
BSV	2 /No.3	14	-	-	-	-
BS90-7A	2 /No.3	14	2 No.3	7	90	YES

Beam BV (no internal stirrups and no external strengthening) was used as a baseline comparison to evaluate the enhancement in strength provided by the NSM FRP rods. Beam BSV, with internal stirrups and no external strengthening, was used to quantify the contribution to the shear strength provided by the NSM FRP rods in presence of steel shear reinforcement. In all the other beams, either vertical or 45-degrees grooves were saw-cut on the surface of both sides of the web. No. 3 CFRP deformed rebars supplied by Marshall Industries Composites Inc. were then embedded in the epoxy-filled grooves. The properties of these rods and of the epoxy paste have been already presented in Section 2.4.1 of this document. The specimen preparation will be described in more detail in Section 5.3.

The variables examined in the experimental test matrix were the following:

- spacing of the rods. Two different spacings were examined, equal to 7 in. and 5 in.;
- inclination of the rods with respect to the longitudinal axis of the beam. Vertical as well as 45-degrees rods were used;
- anchorage in the flange. In two beams (B90-5A and BS90-7A), the NSM rods were anchored in epoxy-filled holes drilled in the flange at the location of the web side grooves;
- presence of internal steel stirrups. Two beams (BSV and BS90-7A) had internal steel stirrups at a spacing of 14 in., that is, greater than the maximum value of $d/2$ (where d is the depth of the beam from the top fiber to the centroid of the longitudinal reinforcement) indicated by the ACI Code.

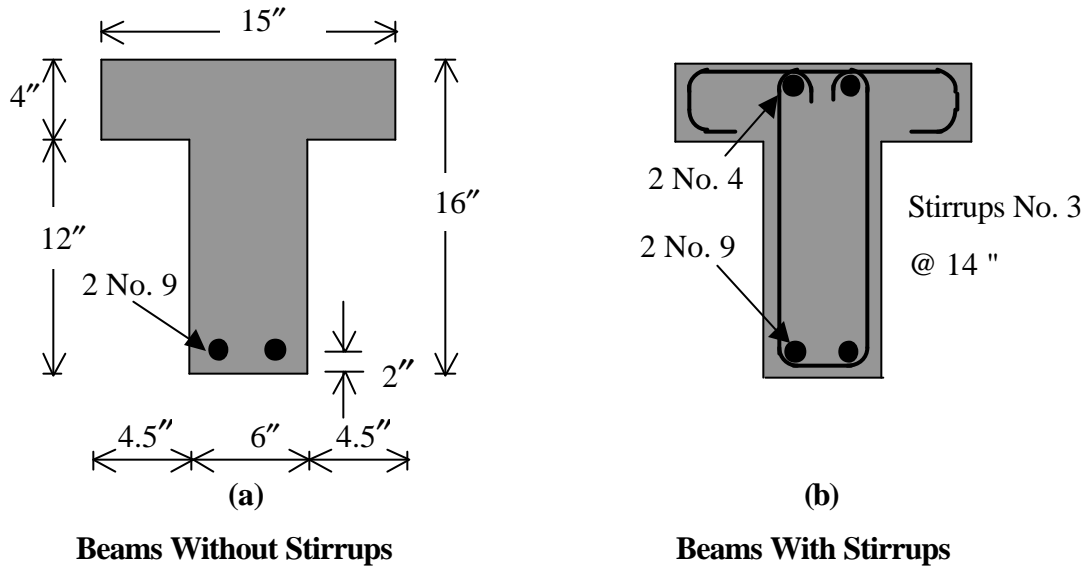


Figure 5.1. Cross-Section of the Beams

5.3. SPECIMEN PREPARATION

The preparation of the strengthened beams involved: cutting of the grooves on the sides of the beams, application of strain gages on the FRP rods and application of the NSM FRP rods.

5.3.1. Cutting of the Grooves. After the beams had cured properly, the grooves were cut from the contractor using a concrete saw. All the grooves had square cross-section, with size of 3/4 in.

5.3.2. Application of Strain Gages. Strain gages were applied on the surface of some FRP rods prior to their application. The purpose was to monitor the strain in the rods during the test at different locations. All the strain gages had a gage length of 1/2 in. to ensure localized strain measurement.

The application of strain gages on the deformed rods involved the removal of the surface deformations in the spots where the strain gages had to be placed. In each of these spots, two ribs were removed by means of a belt sander.

5.3.3. Application of the NSM Rods. The grooves were air blasted to remove the powdered concrete produced by the cutting process and all the possible loose material. Then the epoxy paste was prepared by mixing the two components (resin and hardener) in 2:1 proportion by volume with a power mixer. The groove was filled half-way with the paste (Figure 5.2-a), the rod was then placed

in the groove and lightly pressed (Figure 5.2-b). This forced the paste to flow around the bar and fill completely between the bar and the sides of the groove. The groove was then filled with more paste and the surface was leveled (Figure 5.2-c).

5.4. TEST PROCEDURE

The epoxy paste was allowed to cure for 15 days (full cure time at room temperature) prior to testing of the beams. The beams were loaded under four-point bending with a shear span of 42 in. This corresponded to an a/d ratio equal to 3.0, being a the shear span and d the depth of the cross-section from the top fiber to the centroid of the longitudinal reinforcement.

The test setup included two roller supports and a reaction frame. Load was applied by means of a 400-kip hydraulic jack connected to an electric pump and recorded with a 200-kip load cell. Each beam was instrumented with four LVDTs. Two LVDTs were placed at mid-span on the two sides of the beam to measure deflection. One LVDT was placed at each support to account for the support settlement. Strain gages were applied on the CFRP rods and on the steel stirrups at various locations. Figure 5.3 shows the position of NSM rods and steel stirrups in the tested beams except for beam BV, that did not have any shear reinforcement. The location of the strain gages is indicated together with the numbers that were used to identify them. Only the strain gages that were properly working have been reported.



(a)



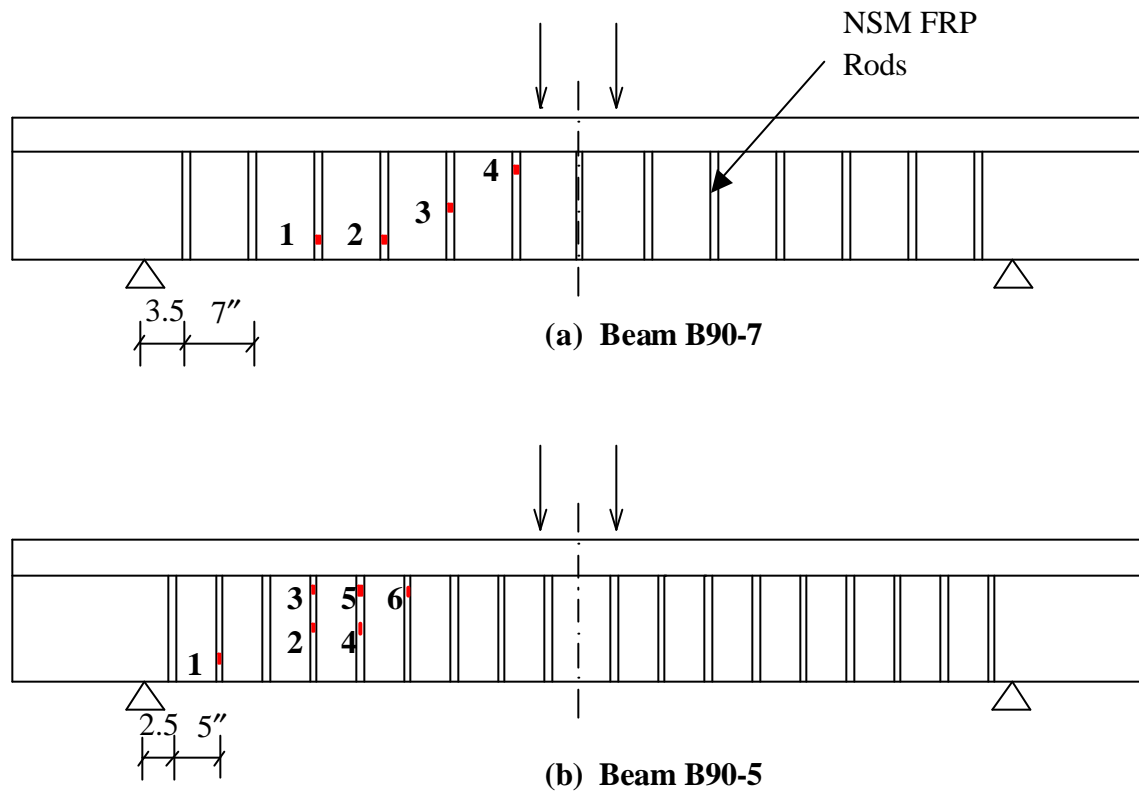
(b)



(c) (d)

Figure 5.2. Specimen Preparation

Beams B90-7 and B90-5 were externally strengthened with NSM rods along their whole length. Strain gages were placed symmetrically on both sides of these beams, in order to ensure that strain data would be collected at the side where shear failure would occur. In Figure 5.3, for simplicity, the strain gage location on these beams is reported only on one side. In all the other beams, half-beam was reinforced for shear with steel stirrups at a spacing of 7 in. and had no external strengthening with NSM rods. The spacing of the stirrups in this side of the beam was designed to ensure that failure would occur in the other side. The latter was the actual test side, and had the shear reinforcement previously described and indicated in Table 5.1. Only the test side needed to be instrumented with strain gages.



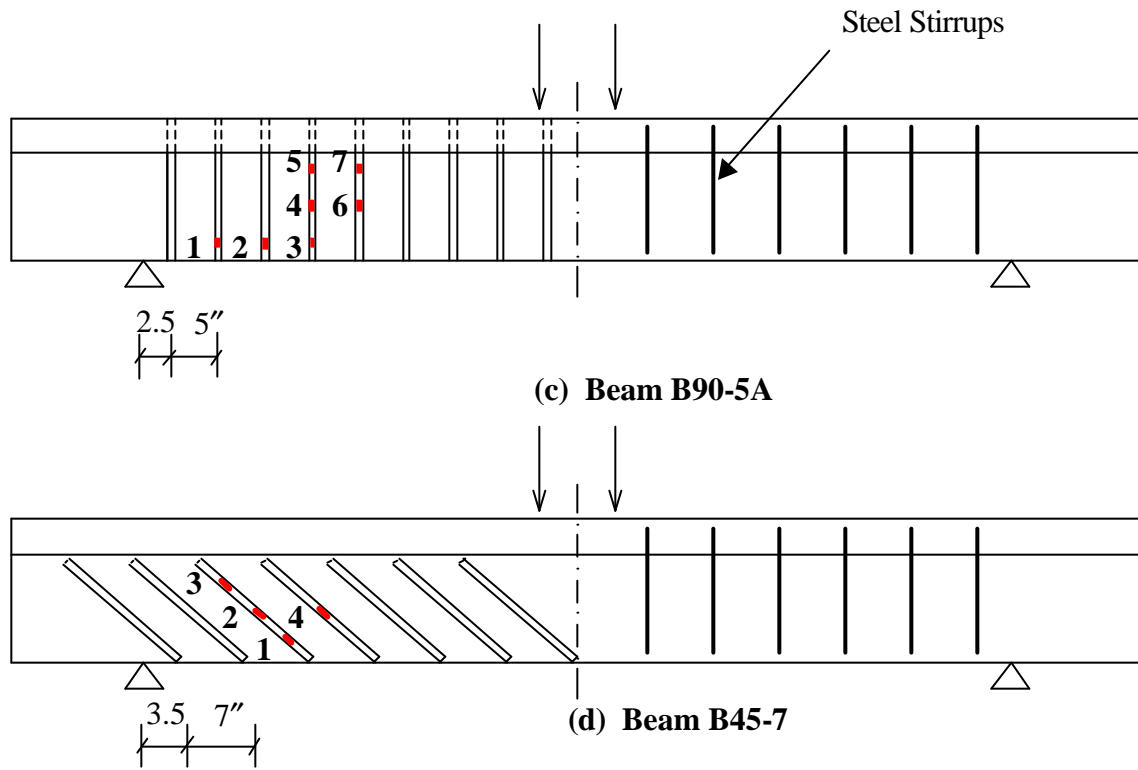
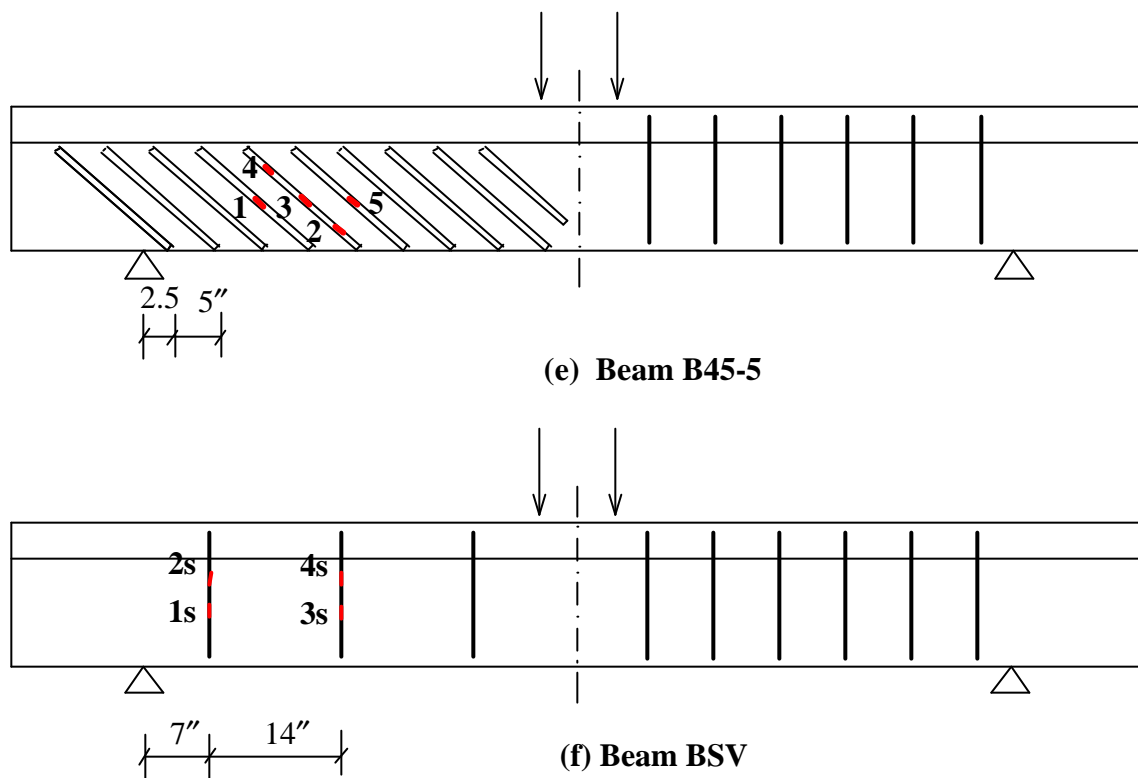


Figure 5.3. Location of Strain Gages



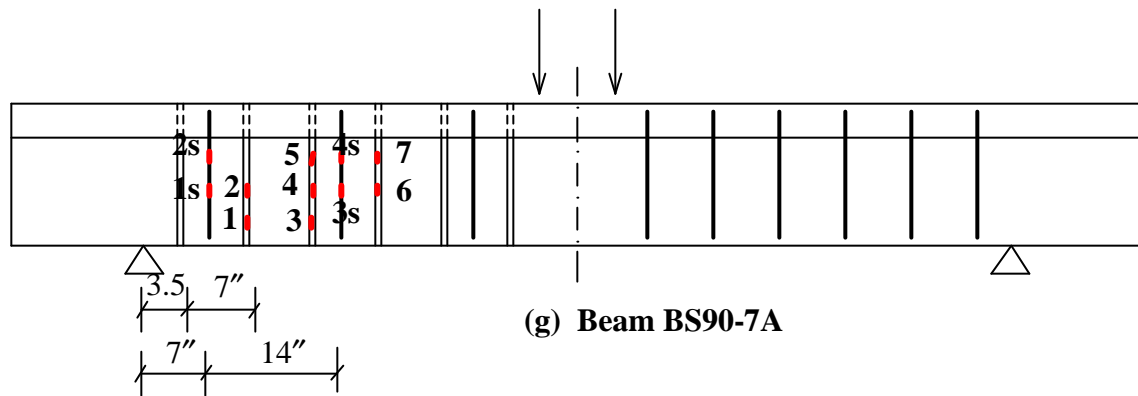


Figure 5.3 (cont'd). Location of Strain Gages

Load, deflections and strains were all recorded with a one-Hertz sampling rate by a LABTECH data acquisition system. Figures 5.4 and 5.5 illustrate the test setup.

Load was applied in cycles of loading and unloading, with the number of cycles depending on the maximum expected load. Applying the load by cycles allows to monitor the stability of the system and the proper working of the instrumentation. All the load vs. mid-span deflection and load vs. strain diagrams reported in the following are envelopes of those obtained from the data acquisition system.

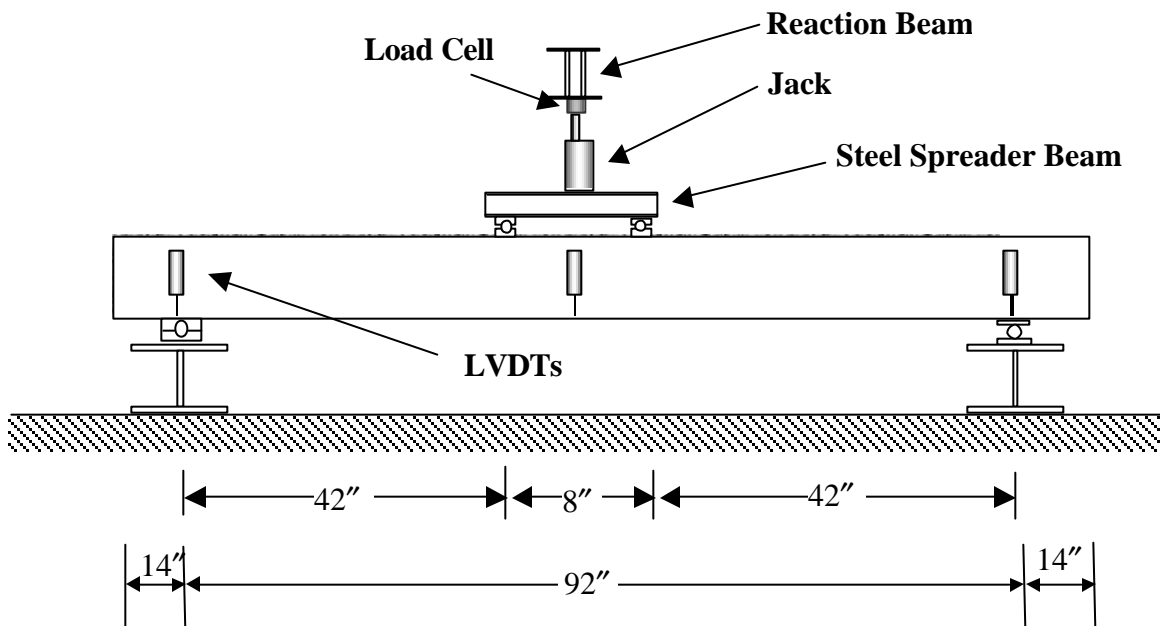


Figure 5.4. Test Setup



Figure 5.5. Test Setup of Beam B90-7

5.5. EXPERIMENTAL RESULTS

5.5.1. Beams Without Steel Stirrups. Beam BV was the control specimen, with no external strengthening. During loading of the beam, diagonal shear cracks formed at a load of 24.7 kips. The shear cracks initiated at the center of both shear spans almost simultaneously. The first shear crack was the critical crack in the specimen. As the load increased, this crack widened and propagated until failure resulted at a load of 40.6 kips. Figure 5.6 shows the specimen after failure.



Figure 5.6. Failure of Beam BV

In specimen B90-7, with NSM vertical rods at a spacing of 7 in., failure occurred at a load of 51.8 kips. This corresponded to an increase in capacity of 27.6% with respect to beam BV. Diagonal shear cracks formed also in this beam, widened and propagated as the applied load increased. A crackling noise revealed throughout the test the progressive cracking of the epoxy paste in which the CFRP rods were embedded. Failure eventually occurred by splitting of the epoxy cover in one of the NSM FRP rods intersected by the major shear crack (Figure 5.7). The crack pattern of beam B90-7 is illustrated in Figure 5.8. The applied load versus the vertical strain in the CFRP rods is plotted in Figure 5.9. The highest vertical strain in the rods was recorded at 3 in. from a diagonal crack and was approximately equal to $850 \mu\epsilon$. It must be pointed out that this strain value and all those herein reported are not necessarily maximum values. They are strictly related to the location of the gages relatively to that of the shear cracks.



Figure 5.7. Failure of Beam B90-7

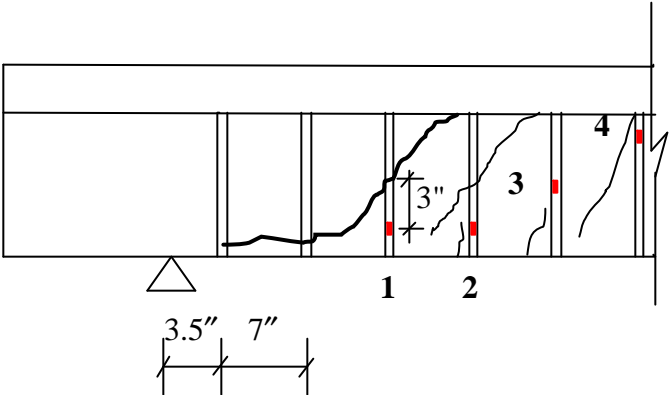
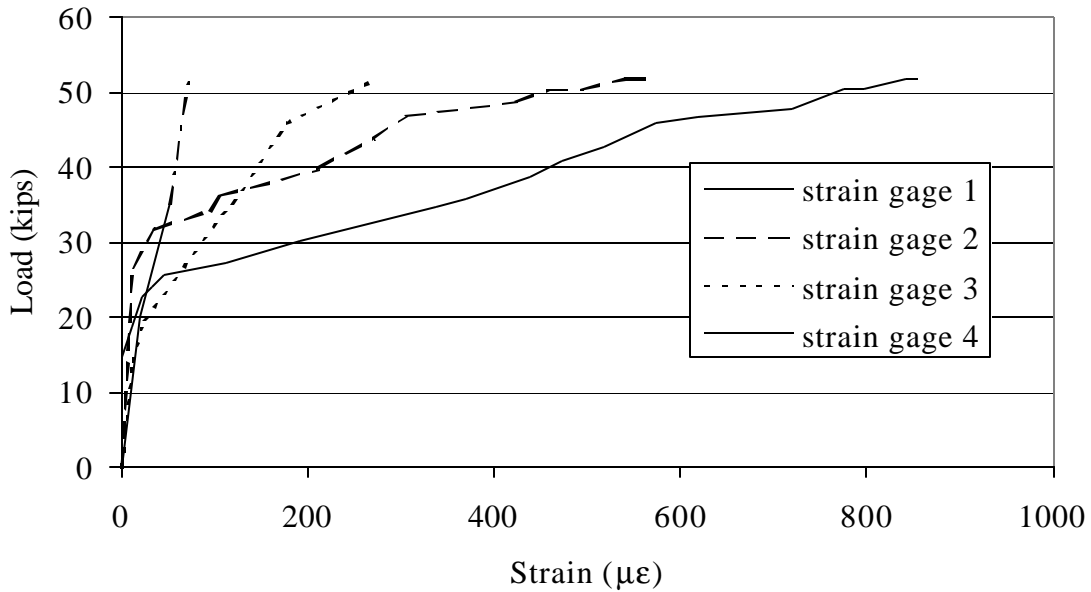


Figure 5.8. Crack Pattern of Beam B90-7



Figure

5.9. Load vs. Strain Diagram of Beam B90-7

Same behavior and failure mode were registered from testing of beam B90-5, which differed from B90-7 only for the closer spacing of the CFRP rods (5 in.). The ultimate load was 57.4 kips, corresponding to an increase in capacity of 41.4% over the control beam and of 10.8% over specimen B90-7. Figure 5.10 is a picture of the failure mode. The crack pattern is illustrated in Figure 5.11. The load versus strain diagram is plotted in Figure 5.12. Strain gage 2, located at 0.5 in. from the major shear crack, recorded a maximum vertical strain approximately equal to 3000 $\mu\epsilon$. This value corresponds to 16.8% of the ultimate strain of the CFRP rods, as reported in Section 2.4 of this document.

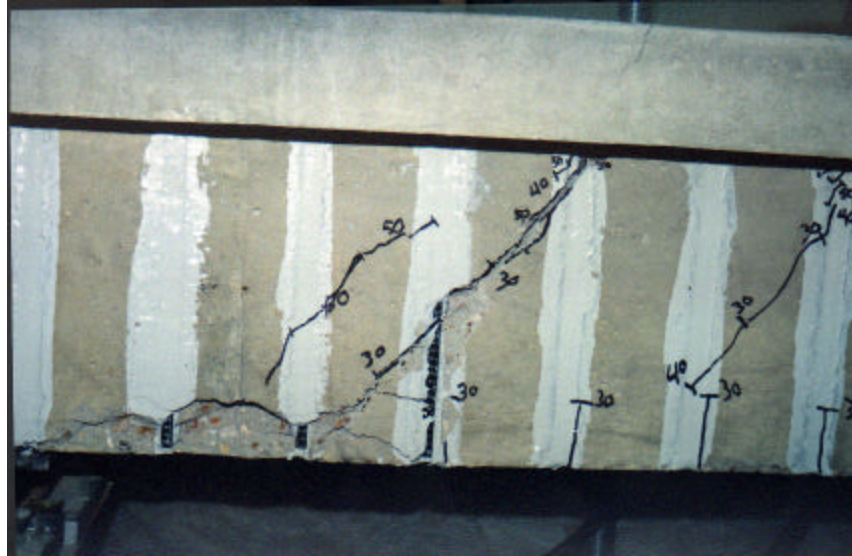


Figure 5.10. Failure of Beam B90-5

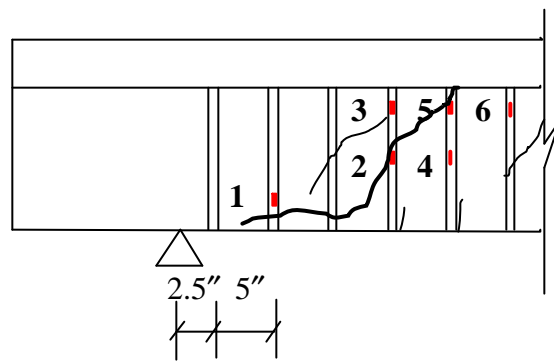


Figure 5.11. Crack Pattern of Beam B90-5

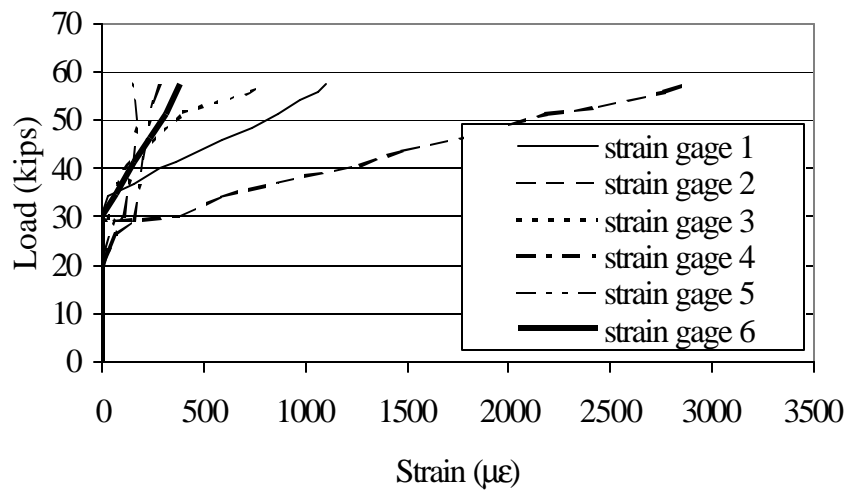


Figure 5.12. Load vs. Strain Diagram of Beam B90-5

Specimen B90-5A was identical to specimen B90-5, except that the CFRP rods were anchored in epoxy-filled holes drilled through the flange. This led to a change in the failure mode and to a substantial increase in the beam capacity. The ultimate load was 83.5 kips, indicating an increase of 105.7%, 61.2% and 45.5% compared to beams BV, B90-7 and B90-5, respectively. The first diagonal shear cracks became visible at a load level approximately equal to 40 kips. As the load increased, more shear cracks formed throughout the shear span, widened and propagated. At higher load levels, secondary cracks formed in the concrete at the level of the longitudinal steel reinforcement as a result of splitting forces developed by the deformed steel bars and of dowel action forces in the longitudinal bars transferring shear across the cracks. Failure eventually occurred in a sudden fashion by loss of the concrete cover of the longitudinal reinforcement (Figure 5.13).

The crack pattern is illustrated in Figure 5.14. The strain data recorded from the strain gages is reported in Figure 5.15. A maximum strain in the FRP of approximately 2300 $\mu\epsilon$ was observed. Most of the recorded strains were found to increase with load up to a certain point, beyond which they started decreasing and then showed an irregular behavior up to failure. The drop in strain can be explained as a result of slippage of the NSM rods. The curves in Figure 5.15 indicate that slippage started in two rods at a load level between 50 and 60 kips, that is, close to the failure load of beam B90-5. At higher load levels, also the other rods started slipping. In B90-5A, anchoring the rods in the flange was effective in preventing failure of the bond between the NSM rods and the epoxy, so allowing the beam to carry additional load also after onset of slip. As a result, the controlling failure mechanism shifted to splitting of the concrete cover.

Specimen B45-7 had NSM rods at a spacing of 7 in. inclined at 45 degrees with respect to the longitudinal axis of the beam. Failure occurred at 74.4 kips, corresponding to an increase in capacity of 83.3% over the control beam. As expected, 45-degree inclined rods were more effective than vertical rods at the same spacing, as showed by the 43.6% increase in capacity of B45-7 with respect to B90-7. Failure, as in B90-7, was controlled by splitting of the epoxy cover that occurred simultaneously in two of the NSM FRP rods intersected by the major shear crack (Figure 5.16). The crack pattern is illustrated in Figure 5.17. The strain data recorded from the strain gages is reported in Figure 5.18. The maximum recorded strain was equal to approximately 4600 $\mu\epsilon$, corresponding to 25.7% of the ultimate strain.



(a)



(b)

Figure 5.13. Failure of Beam B90-5A

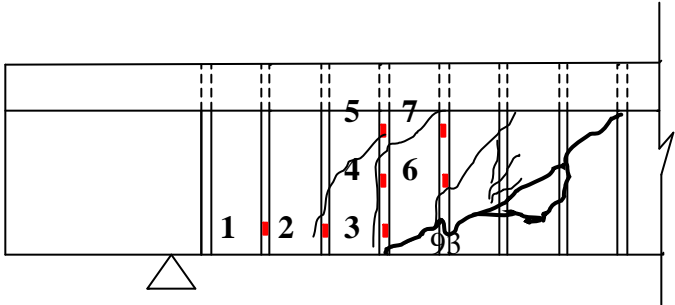


Figure 5.14. Crack Pattern of Beam B90-5A

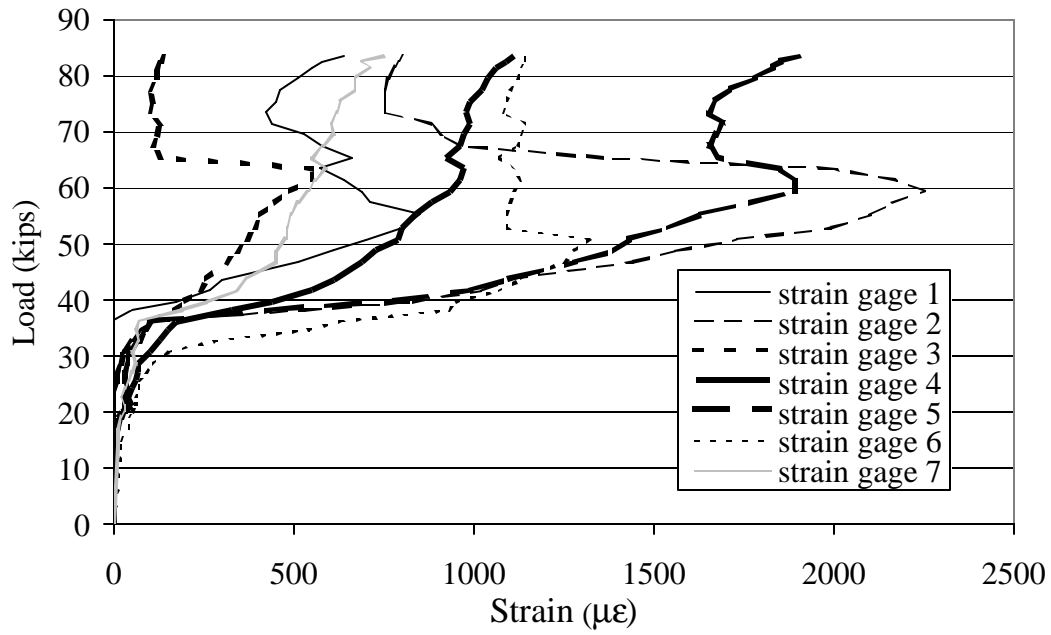


Figure 5.15. Load vs. Strain Diagram of Beam B90-5A

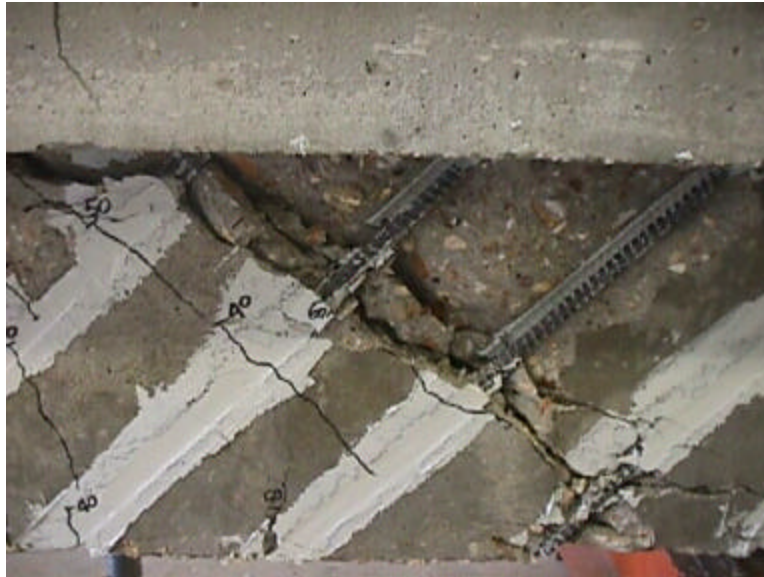


Figure 5.16. Failure of Beam B45-7

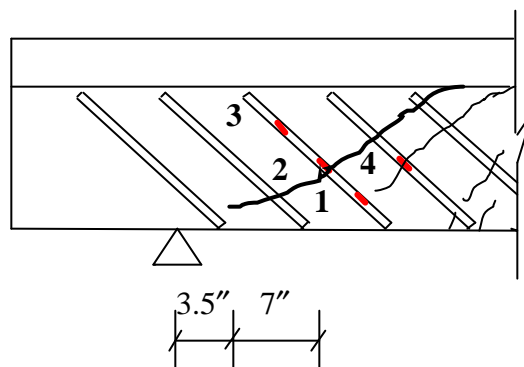


Figure 5.17. Crack Pattern of Beam B45-7

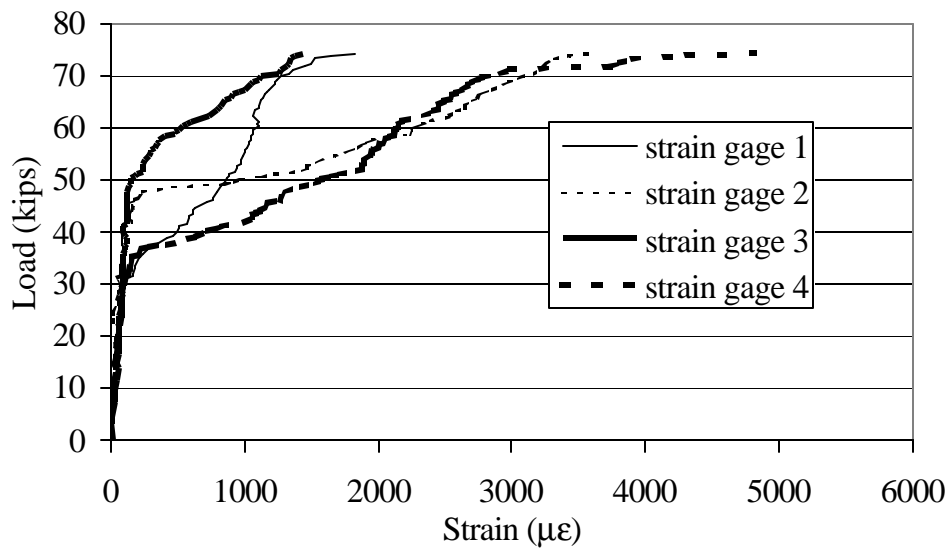


Figure 5.18. Load vs. Strain Diagram of Beam B45-7

Specimen B45-5 differed from B45-7 for the spacing of the rods, equal to 5 in. Failure occurred at a load level of 80 kips, showing an increase in capacity of 97%, 7.5% and 39.4% over BV, B45-7 and B90-5, respectively. The failure mode was the same previously described for specimen B90-5A, that is, formation of splitting cracks along the longitudinal reinforcement and eventual loss of the concrete cover (Figure 5.19).



(a)



(b)

Figure 5.19. Failure of Beam B45-5

Figure 5.20 shows the load vs. net mid-span deflection diagrams of the six beams described so far, none of which had steel shear reinforcement. As previously mentioned, two LVDTs were placed at mid-span on the two sides of the beam to measure deflection. and one LVDT was placed at

each support to account for the support settlement. The net mid-span deflection was computed subtracting the average of the two readings at the supports from the average of the two readings at mid-span. The data appears to be very consistent in terms of stiffness between the different specimens. In each beam, a decrease in stiffness occurred when the failure load was approached. Although beam B90-5A failed at the highest load, it experienced a decrease in stiffness at a lower load level than beams B45-7 and B45-5. This phenomenon occurred after 60 kips of applied load, which corresponds to onset of slip of the NSM rods, as previously inferred from the load vs. strain diagram.

Table 5.2 is a summary of the test results, in terms of ultimate load and failure mode.

Table 5.2. Summary of Test Results

Beam Code	Ultimate Load (kips)	Failure Mode
BV	40.6	SC
B90-7	51.8	BF
B90-5	57.4	BF
B90-5A	83.5	SP
B45-7	74.4	BF
B45-5	80.0	SP
BSV	68.9	SC
BS90-7A	93.0	SP + FF

SC = Shear-Compression;
 BF = Bond Failure of NSM Rods;
 SP = Splitting of the Concrete Cover;
 FF = Flexural Failure.

5.5.2. Beams With Steel Stirrups. In beam BSV, with steel stirrups of Grade 50 steel at a spacing of 14 in., shear cracks widened and propagated up to the flange as the load increased. Failure resulted at 68.9 kips (Figure 5.21). Two strain gages were applied on each of the first two stirrups in the test side, whose location is shown in Figure 5.3. The crack pattern is illustrated in Figure 5.22. Only the strain gages on the first stirrup worked properly, and recorded very low values of strain (Figure 5.23) due to their distance from the location of the crack.

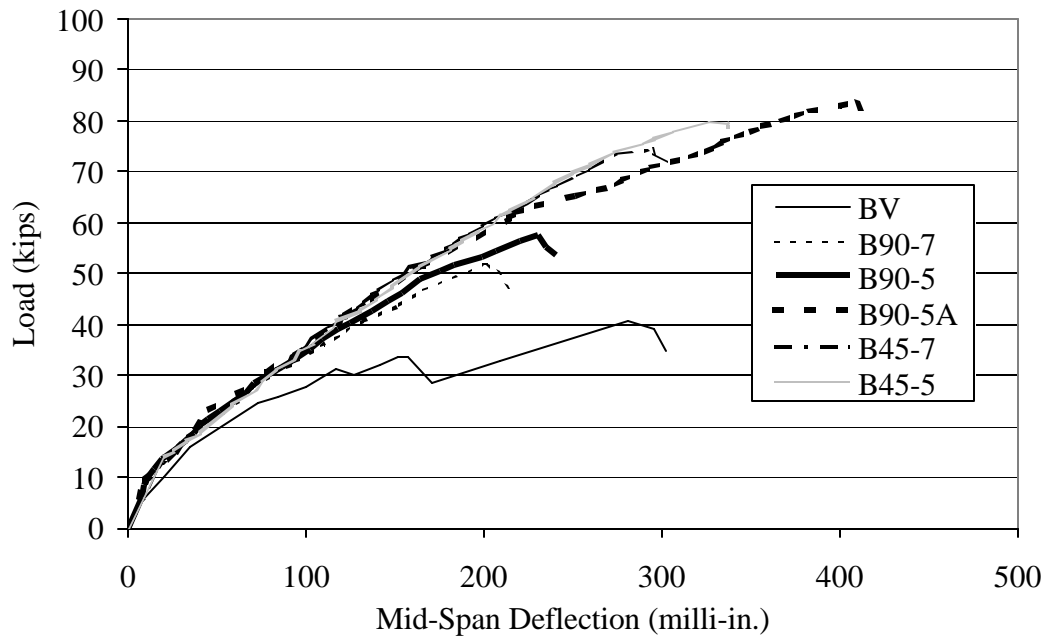


Figure 5.20. Load vs. Mid-Span Deflection of the Beams Without Steel Stirrups



Figure 5.21. Failure of Beam BSV

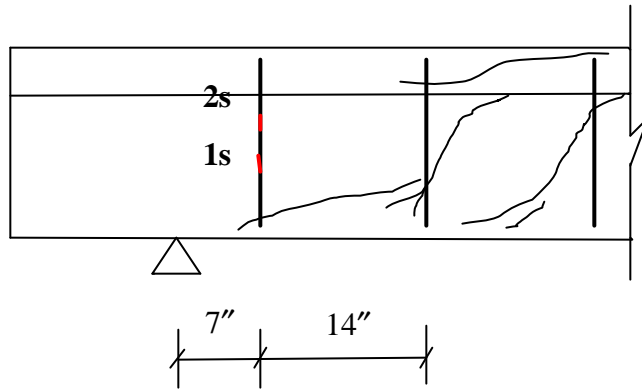


Figure 5.22. Crack Pattern of Beam BSV

Beam BS90-7A had the same steel shear reinforcement as BSV, and was externally strengthened with NSM vertical rods at a spacing of 7 in. anchored in the flange. The ultimate load was 93.0 kips, that is, 35% larger than the capacity of beam BSV. The final failure mode was splitting of the concrete cover as previously described for beam B90-5A (Figure 5.24-a). In this case, however, it occurred when flexural failure was already ongoing, as evident from the crushing line in the concrete top fiber at mid-span (Figure 5.24-b) and from the load vs. mid-span deflection diagram. Another difference with respect to failure of beams B90-5A and B45-5 is that the concrete cover did not spall completely, due to the restraining action of the steel stirrups. The crack pattern is illustrated in Figure 5.25. Figures 5.26 and 5.27 show the strain data recorded from the strain gages on the steel stirrups and on the FRP rods, respectively. Of the strain gages on the steel stirrups, strain gage 4s recorded the highest value, very close to the yielding strain of the steel stirrups ($1724 \mu\epsilon$). As in the case of beam B90-5A, the inversion point in some of the load vs. FRP-strain curves reveals the occurrence of slip of the FRP rods.

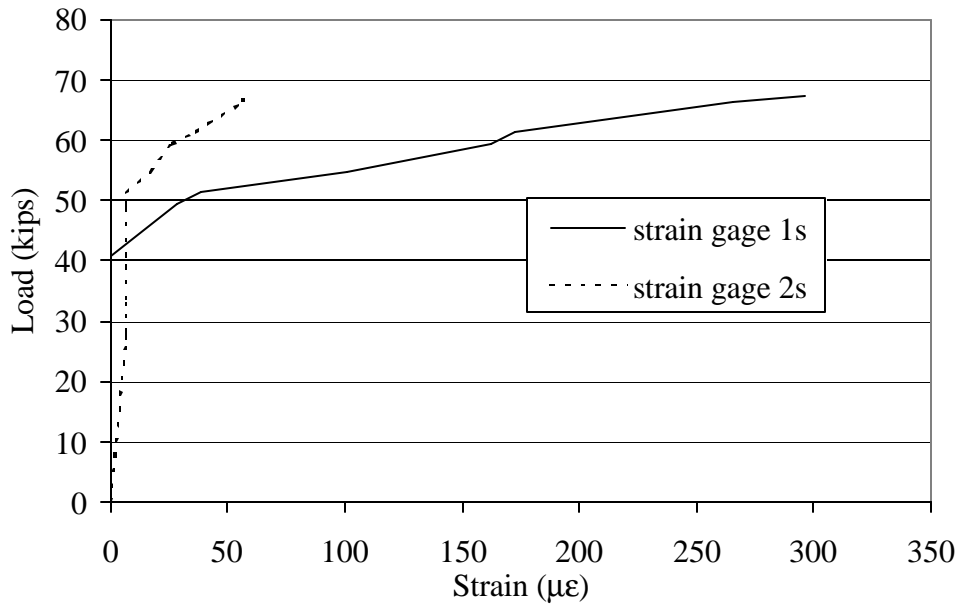


Figure 5.23. Load vs. Strain Diagram of Beam BSV



(a)

Figure 5.24. Failure of Beam BS90-7A



(b)

Figure 5.24 (cont'd). Failure of Beam BS90-7A

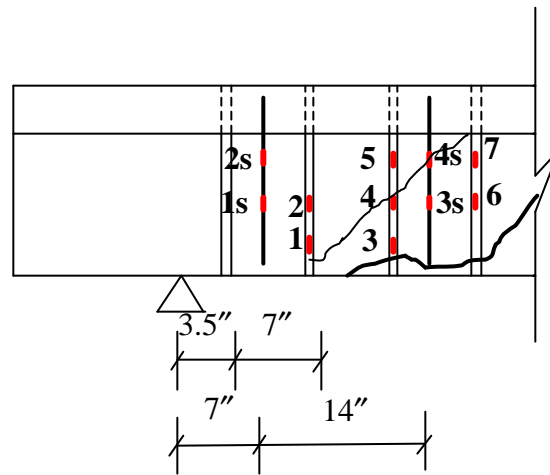


Figure 5.25. Crack Pattern of Beam BS90-7A

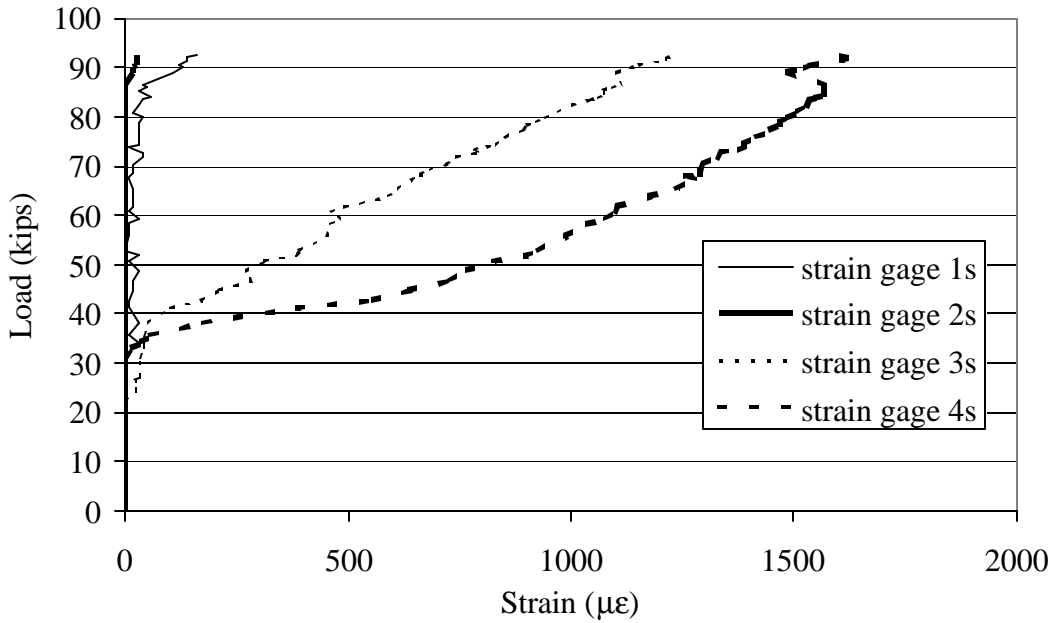
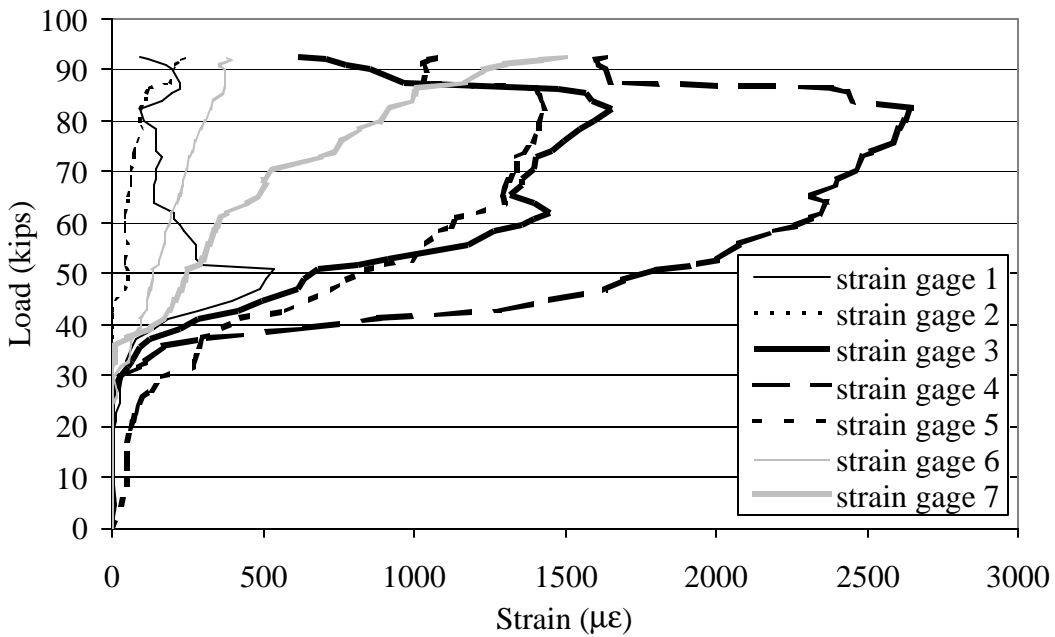


Figure 5.26. Load vs. Strain Diagram of Beam BS90-7A (Steel Stirrups)



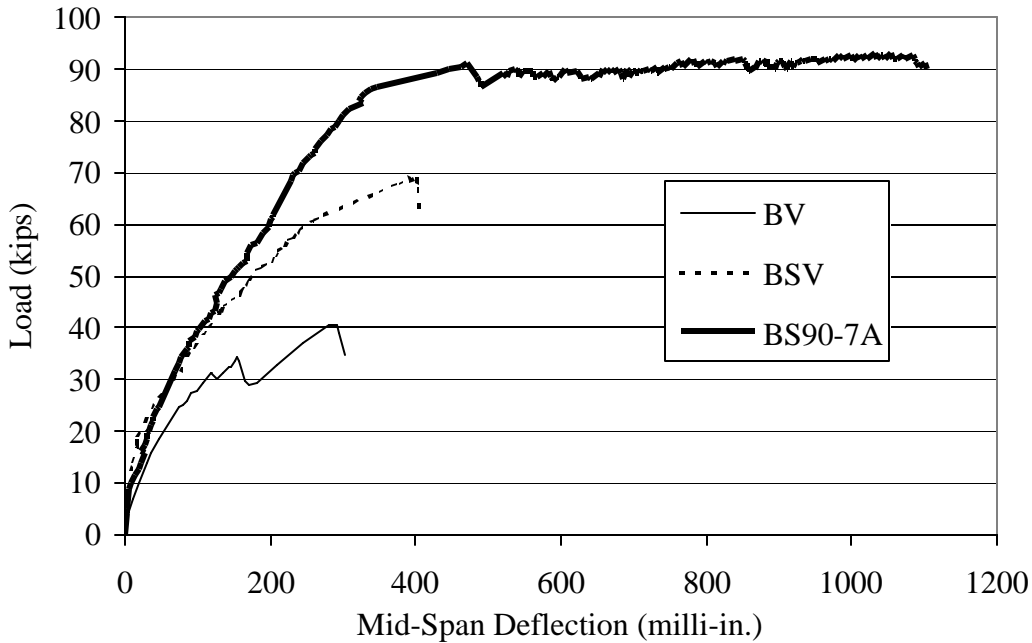
5.27. Load vs. Strain Diagram of Beam BS90-7A (CFRP Rods)

Figure

Figure 5.28 shows the load vs. net mid-span deflection diagrams of the beams with steel shear reinforcement, including beam BV for reference. The net mid-span deflection was computed as previously illustrated for Figure 5.20.

5.6. DISCUSSION OF TEST RESULTS

Test results show that the use of NSM FRP rods is an effective technique to enhance the shear capacity of RC beams. In absence of steel stirrups, an increase in capacity as high as 105.7% with respect to the control beam could be obtained. Of the two beams with steel stirrups below the ACI requirements, the strengthened one showed an increase in capacity of 35% over the unstrengthened one.



Figure

5.28. Load vs. Mid-Span Deflection of the Beams With Steel Stirrups

The shear capacity of the strengthened beams can be increased by either decreasing the spacing of the NSM rods, or anchoring the rods into the flange, or changing the inclination of the rods from vertical to 45 degrees. These three methods have different degrees of efficiency. Decreasing the spacing of the rods from 7 in. to 5 in., which corresponds to a 40% increase in the amount of FRP material, led to an increase in capacity of 10.8% and 7.5% in the case of vertical and

45-degree rods, respectively. Substituting the vertical rods with 45-degree rods, which corresponds to a 41.4 % increase in the material quantity, enhanced the shear capacity by 43.6% and 39.4%, for the cases of 7-in. and 5-in. spacing, respectively. Anchoring the rods through the flange (33% more FRP material) increased the capacity by 45.5%. These comparisons seem to indicate that the most efficient way to increase the shear capacity of an RC Tbeam is using NSM rods anchored into the flange. Using inclined rods rather than vertical rods is also efficient, while decreasing the spacing between the rods does not produce a remarkable increase in the shear capacity.

Two failure mechanisms were observed, namely, debonding of one or more FRP rods and splitting of the concrete cover. Test results seem to indicate that the first mechanism can be prevented by either anchoring the NSM rods in the beam's flange or using 45-degree rods at a sufficiently close spacing, which provides a larger bond length. Both beams having the FRP rods anchored in the flange presented an inversion point in the load vs. strain curves, which indicated slip of the NSM rods. After onset of slip, the anchorage in the flange was effective in preventing bond failure and allowed the beam to carry additional load. Once this failure mode was prevented, splitting of the concrete cover of the longitudinal steel reinforcement became the controlling factor. All beams whose ultimate load was equal to or greater than 80 kips failed by this mechanism, that appears to be critical in beams strengthened for shear with NSM FRP rods. This can be explained with the difference in configuration between internal stirrups and NSM reinforcement. Internal steel stirrups contribute to the shear strength of an RC beam through three primary mechanisms (ASCE-ACI Committee 426, 1973):

- they carry part of the shear;
- they restrict the growth of the diagonal cracks and thereby help maintain the interface shear transfer;
- they hold the longitudinal bars and increase their dowel capacity. If a stirrup happens to be near the bottom of a major diagonal crack, it is very effective in maintaining the dowel force and restraining the splitting failure, provided that the stirrups are of sufficient size, well anchored and spaced close enough.

In the case of NSM shear reinforcement, while the first two mechanisms are still valid, the third one does not apply for evident reasons. The dowel forces, not restrained by stirrups, give rise to tension stresses in the surrounding concrete and these in combination with the wedging action of the bar

deformations produce splitting cracks along the longitudinal reinforcement which eventually lead to failure of the beam.

5.7. PROPOSED DESIGN APPROACH

5.7.1. Background. The experimental results obtained in the present study suggest that, in RC beams strengthened in shear with NSM FRP rods, one of the controlling failure mechanism is related to bond of the FRP shear reinforcement. Results of the shear tests are consistent with those of the bond tests in that bond failure appears to be controlled by splitting of the epoxy paste cover. However, it should be noted that the obtained results are related to the materials used in this experimental study. The use of FRP rods having different properties, especially in terms of surface configuration, and also the use of epoxy paste having a different tensile strength may lead to different results. The other controlling failure mechanism is splitting of the concrete cover as a result of splitting forces developed by the steel flexural reinforcement and of dowel action forces in the longitudinal bars transferring shear across the cracks. This mechanism is related to many different factors, among which the concrete tensile strength, the thickness of the concrete cover, the number and size of the longitudinal steel bars, the presence of stirrups and their size and spacing.

It is very well known that the behavior of RC beams failing in shear is very complex to be analyzed, due to the large number of variables that influence the behavior and the failure mode, and therefore the ultimate capacity of the beam. An even greater complexity is associated with the analysis of RC beams externally strengthened to enhance their shear capacity. New variables are introduced in the problem, related to the properties of the adopted strengthening system and to the way it interacts with the pre-existing reinforcement.

Most of the studies on RC beams strengthened for shear with FRP sheets model the FRP contribution to the shear capacity in analogy with the case of traditional shear reinforcement with steel stirrups. However, the stress in the FRP at failure is assumed to be less than the FRP tensile strength, and equal to a maximum allowable stress which has been evaluated by means of analytical as well as experimental investigations. Results obtained by different authors are sometimes contradictory. Design algorithms for computing the shear contribution of FRP sheets are still under scrutiny.

Currently, there is no literature available on the shear reinforcement of RC beams using NSM rods. Before a comprehensive design approach able to address all the significant variables is

obtained, an extensive experimental investigation needs to be carried out. In the following, a simple design approach to compute the contribution of NSM FRP rods to the shear capacity of an RC beam is proposed. Of the two failure mechanisms previously described, only the first one has been taken into account. On the basis of the results obtained as part of the present study regarding the behavior of bond of NSM FRP rods (Section 3 of this document) the proposed approach is then applied to the tested beams. The predicted values of the ultimate load are finally compared with the ones obtained experimentally.

5.7.2. Shear Strength of RC Beams Strengthened with FRP. The nominal shear strength of an RC beam may be computed by the basic design equation presented in ACI 318-95 (American Concrete Institute, 1995):

$$V_n = V_c + V_s \quad (5.1)$$

In this equation the nominal shear strength is given by the sum of the shear strength of the concrete and the shear strength provided by the steel shear reinforcement. In the case of beams externally strengthened with FRP, the nominal shear strength can be computed by adding a third term to account for the contribution of the FRP reinforcement (Khalifa et al., 1998):

$$V_n = V_c + V_s + V_{FRP} \quad (5.2)$$

The design shear strength is obtained by applying a strength reduction factor, ϕ , to the nominal shear strength. When proposing a design procedure for RC beams strengthened in shear with externally bonded FRP sheets, Khalifa et al. (1998) suggested to maintain the reduction factor of $\phi = 0.85$ given in ACI 318-95 for the concrete and steel terms, and to apply a more stringent reduction factor ($\phi = 0.70$) to the FRP contribution, to account for the novelty of this strengthening technique. The same reasoning should be applied to shear strengthening with NSM FRP rods.

Limits on the value of V_{FRP} and of the sum ($V_s + V_{FRP}$) have been also proposed (Khalifa, 1999):

$$V_{FRP} \leq 4\sqrt{f'_c}b_wd \quad (5.3)$$

$$V_s + V_{FRP} \leq 8\sqrt{f'_c}b_wd \quad (5.4)$$

The first limit on the maximum amount of additional shear strength that may be achieved is placed in terms of the shear strength of the concrete. This limit is imposed primarily to establish a basis for judging when the use of FRP is not suitable for shear reinforcement. Furthermore, this limit maintains the use of FRP as supplemental reinforcement. The second limit is a modification of ACI

provision in Section 11.5.6.8, which attempts to guard against excessive crack width by limiting the maximum shear transmitted by the stirrups. Since (5.3) and (5.4) are based on a reasoning that does not depend on the specific strengthening system, they should be applied also to strengthening with NSM FRP rods.

5.7.3. Contribution of NSM FRP Rods to Shear Capacity. To compute the nominal shear strength given by (5.2), the contribution of NSM FRP rods to the shear capacity needs to be quantified. Although several parameters are believed to exert an influence on this contribution, it is not possible yet to develop a comprehensive design approach including all the significant parameters. No experimental data on RC beams strengthened in shear with NSM FRP rods other than the ones herein presented are available to date. This preliminary design approach includes two equations that may be used to obtain V_{FRP} and suggests taking the lower of the two results as the contribution of NSM FRP rods to the shear capacity. This is proposed as a protocol to be followed also when further experimental data will be made available, so allowing a better calibration.

The first equation computes the FRP shear strength contribution related to bond-controlled shear failure, V_{IF} . The second equation calculates the shear resisted by NSM FRP rods when the maximum strain in the rods is equal to $4,000 \mu\epsilon$, V_{2F} . This limit is suggested to maintain the shear integrity of the concrete (Khalifa et al., 1998). At higher levels of strain, the shear crack width would be such that aggregate interlock would be lost and the shear capacity of the concrete compromised.

It is proposed that, in the calculations, a reduced value is used for the height of the cross-section containing shear reinforcement in the form of NSM rods:

$$d_{net} = d_r - 2 \cdot c \quad (5.5)$$

where d_r is the height of the shear-strengthened part of the cross-section and c is the concrete cover of the internal longitudinal reinforcement. In the case of vertical NSM rods, d_r coincides with the length of the FRP rods.

5.7.4. Calculation of V_{IF} . V_{IF} is the FRP shear strength contribution related to bond-controlled shear failure. It is computed using the following assumptions:

- inclination angle of the shear cracks constant and equal to 45° ;
- even distribution of bond stresses along the FRP rods at ultimate;
- the ultimate bond strength is reached in all the rods intersected by the crack at ultimate.

The first assumption can be easily removed. However, the error it may produce is not significant if considered in the context of approximation of this preliminary model.

The validity of the second assumption is related to the bond behavior of the NSM FRP rods and to the depth of the beam. For the CFRP rods used in this study, the bond stress distribution at ultimate resulted to be approximately constant even for the longest of the examined bonded lengths (24 diameters, corresponding to 9 in.). On the other hand, the depth of the tested beams is such that the longest bonded length considered in the calculations was less than 24 rod diameters.

The bond stress distribution for longer bonded lengths can be analytically obtained once the local bond stress – slip relationship is drawn. When other types of FRP rods are used, the bond behavior can be substantially different and the assumption of constant bond stresses at ultimate may result inadequate. In this case, the value of the average bond strength would depend on the bonded length (which in turn, for application in shear strengthening, depends on the beam depth) and could be computed from the local bond stress – slip relationship of the given type of FRP rod.

The shear force resisted by the FRP may be computed as the sum of the forces resisted by the FRP rods intersected by a shear crack. Each rod intersected by a crack may be ideally divided in two parts at the two sides of the crack. The force in each of these rods can be calculated as the product of the average bond strength and the surface area of the shortest part, that from now on will be referred to as effective length of the rod. Therefore:

$$V_{1F} = 2 \cdot \sum A_i f_i = 2 \cdot \mathbf{p} \cdot d_b \cdot \mathbf{t}_b \cdot L_{tot} \quad (5.6)$$

where A_i is the nominal cross-sectional area of the rods, f_i the tensile stress in the rod and summation is extended to all the rods intersected by a 45-degree crack. L_{tot} is the sum of the effective lengths of all the rods crossed by the crack. L_{tot} has to be calculated in the most unfavorable crack position, that is the position in which it is minimum. Therefore:

$$V_{1F} = 2 \cdot \mathbf{p} \cdot d_b \cdot \mathbf{t}_b \cdot L_{tot\min} \quad (5.7)$$

The value of $L_{tot\min}$ depends on d_{net} , on the spacing s of the rods and on their inclination.

Three cases have been considered for vertical rods:

- **CASE 1:** $\frac{d_{net}}{2} < s < d_{net}$
- **CASE 2:** $\frac{d_{net}}{3} < s < \frac{d_{net}}{2}$

- **CASE 3:** $\frac{d_{net}}{4} < s < \frac{d_{net}}{3}$

These three ranges have been chosen based on physical/practical considerations. A spacing s greater than d_{net} would not result in an effective strengthening. On the other hand, adopting s less than $d_{net}/4$ would not be convenient from a practical standpoint.

These cases are illustrated in Figures 5.29 through 5.31. The coordinate x , with $0 \leq x \leq s$, indicates the position of the crack with respect to the rods. As already stated before, each rod intersected by the crack may be ideally divided in two parts at the two sides of the crack. The part considered in the calculations is the shortest of the two. The length of the shortest part, or effective length of the rod, has been indicated with L_i , where the subscript i indicates the i th of the rods intersected by the shear crack. Since L_i is a function of the coordinate x , the sum L_{tot} of the effective lengths of all the rods intersected by the shear crack is also a function of x . These functions have been determined on the basis of simple geometric calculations and plotted in Figures 5.32 through 5.34. As an example, in Figure 5.32-a, L_1 and L_2 are plotted as functions of x . If x increases from 0 to $s-d/2$, only one rod is intersected by the crack and its effective length L_1 increases from $d-s$ to $d/2$. When x increases from $s-d/2$ to $2s-d$, L_1 decreases correspondingly from $d/2$ to $d-s$. For x greater than $2s-d$, two rods are intersected by the shear crack, their effective lengths are L_1 and L_2 and they vary with x as illustrated. Figure 5.32-b presents L_{tot} , that is the summation of L_1 and L_2 , plotted as a function of x .

For case 1, the single effective lengths and their sum L_{tot} have been plotted in two separate diagrams for clarity. In Figures 5.33 and 5.34, effective lengths and L_{tot} have been reported in the same diagram as functions of x . The two figures refer to cases 2 and 3, respectively.

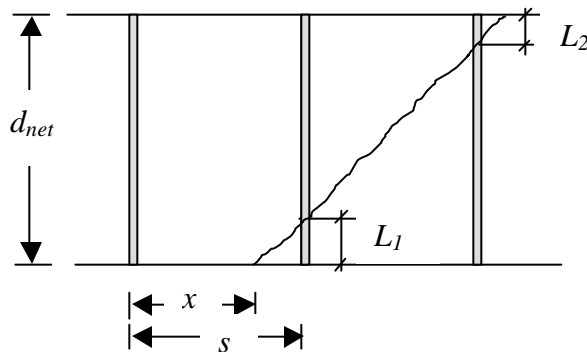


Figure 5.29. Case 1 ($\frac{d_{net}}{2} < s < d_{net}$)

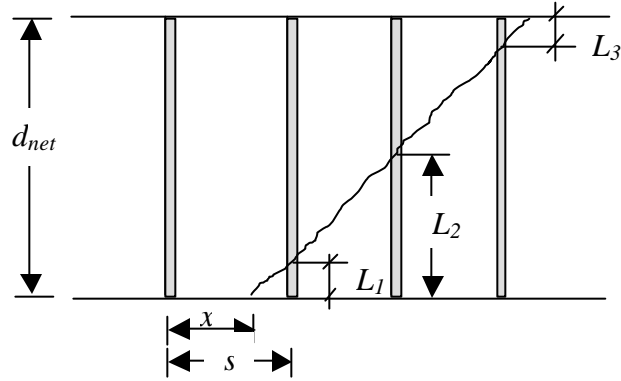


Figure 5.30. Case 2 ($\frac{d_{net}}{3} < s < \frac{d_{net}}{2}$)

It resulted that, for vertical rods:

$$L_{tot\min} = d_{net} - s \quad \text{if} \quad \frac{d_{net}}{3} < s < d_{net} \quad (5.8a)$$

$$L_{tot\min} = 2 \cdot d_{net} - 4 \cdot s \quad \text{if} \quad \frac{d_{net}}{4} < s < \frac{d_{net}}{3} \quad (5.9a)$$

It may be noted that cases 1 and 2 resulted in the same value of $L_{tot\min}$, so they have been unified in Equation 5.8-a.

The same procedure has been applied to the case of 45-degree inclined rods, obtaining the following results:

$$L_{tot\min} = (2d_{net} - s) \frac{\sqrt{2}}{2} \quad \text{if} \quad \frac{2d_{net}}{3} < s < 2d_{net} \quad (5.8b)$$

$$L_{tot\min} = 2\sqrt{2}(d_{net} - s) \quad \text{if} \quad \frac{d_{net}}{2} < s < \frac{2d_{net}}{3} \quad (5.9b)$$

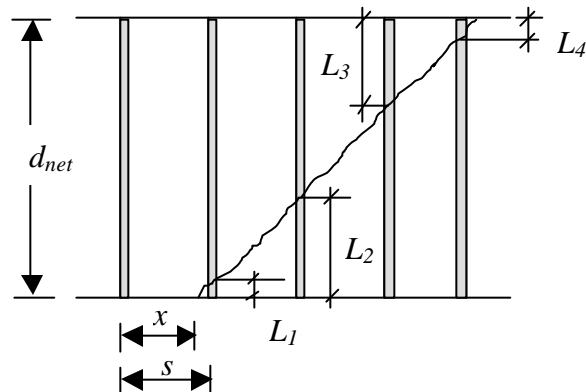


Figure 5.31. Case 3 ($\frac{d_{net}}{4} < s < \frac{d_{net}}{3}$)

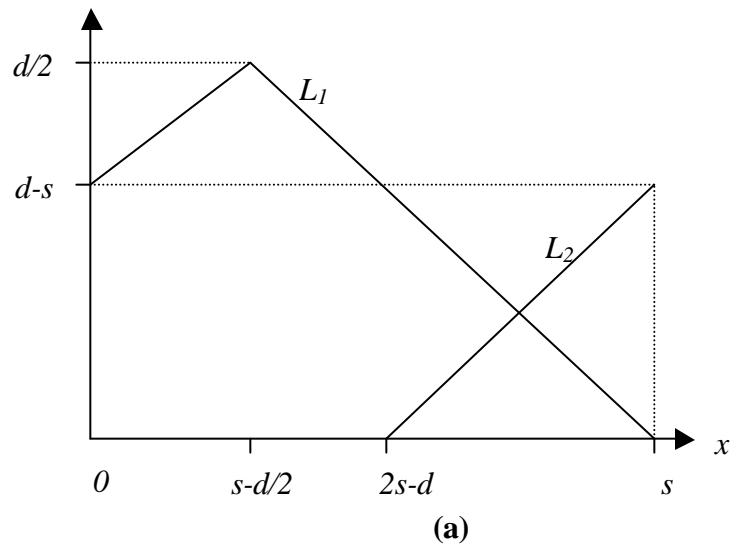


Figure 5.32. Calculation of L_{totmin} for Case 1

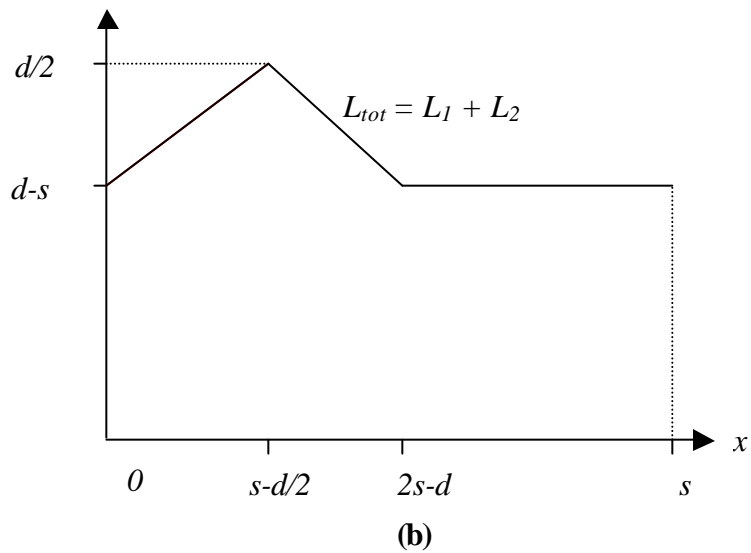


Figure 5.32 (cont'd). Calculation of L_{totmin} for Case 1

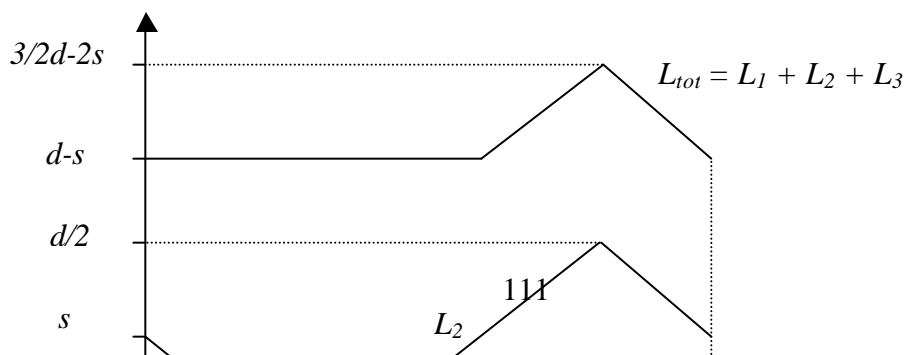


Figure 5.33. Calculation of L_{totmin} for Case 2

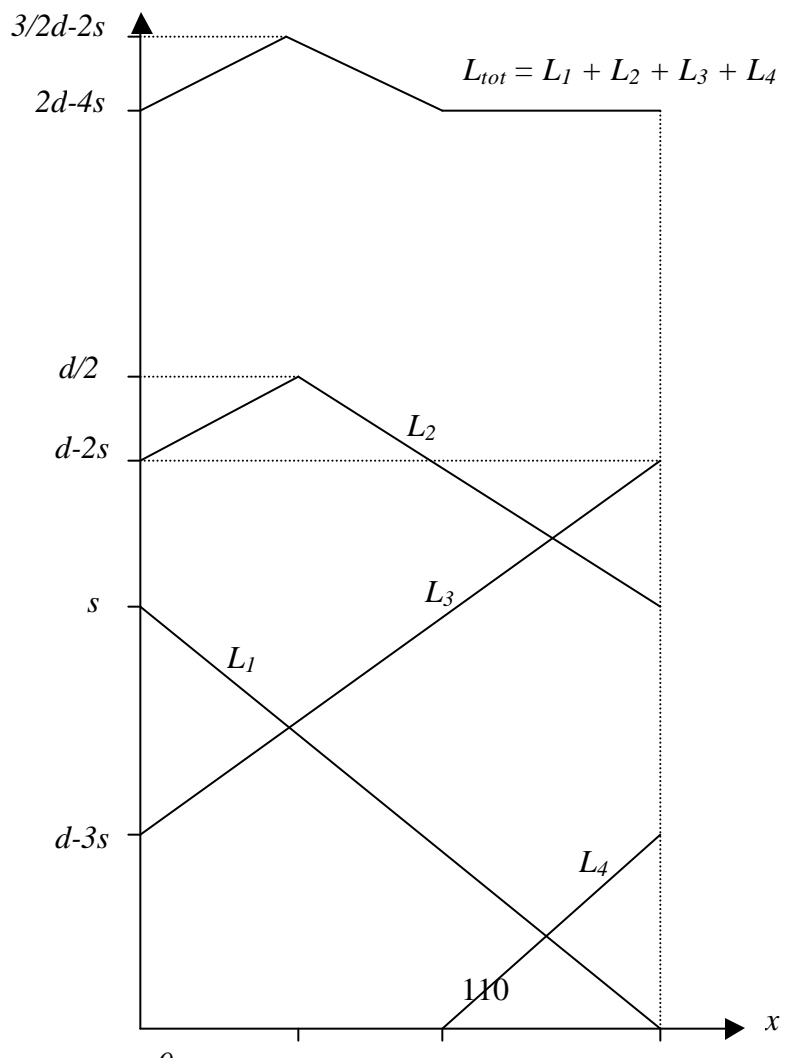


Figure 5.34. Calculation of L_{totmin} for Case 3

5.7.5. Calculation of V_{2F} . V_{2F} is the FRP shear strength contribution corresponding to a maximum FRP strain of 4,000 $\mu\epsilon$. The effective length of an FRP rod crossed by the crack corresponding to a strain of 4,000 $\mu\epsilon$ is:

$$\bar{L}_i = 0.001 \frac{d_b \cdot E_b}{t_b} \quad (5.10)$$

The maximum effective length of an FRP rod crossed by the crack is:

$$L_{i \max} = \frac{d_{net}}{2} \quad (5.11a)$$

for vertical rods, and:

$$L_{i \max} = \frac{d_{net}}{\sqrt{2}} \quad (5.11b)$$

for 45-degree rods. If $L_{i \max} < \bar{L}_i$, that is, if:

$$d_{net} < 0.002 \frac{d_b \cdot E_b}{t_b}, \quad (5.12a)$$

or:

$$d_{net} < \sqrt{2} \cdot 0.001 \frac{d_b \cdot E_b}{t_b}, \quad (5.12b)$$

for vertical and 45-degree rods, respectively, calculation of V_{2F} is not necessary. If (5.12) is not satisfied, V_{2F} has to be computed.

The average bond stress in the longest effective length corresponding to a strain of 4,000 $\mu\epsilon$ is:

$$t_{bred} = \frac{d_b}{4} \cdot \frac{E_b (0.004)}{L_{i \max}} = 0.001 \cdot \frac{d_b E_b}{L_{i \max}} = \frac{\bar{L}_i}{L_{i \max}} \cdot t_b \quad (5.13)$$

where $L_{i \max}$ is the longest effective length of the rods intersected by the crack. Assuming that tensile stresses in the rods are proportional to their effective lengths, it is:

$$V_{2F} = 2 \cdot \mathbf{p} \cdot d_b \cdot \mathbf{t}_{bred} \cdot \sum L_i = 2 \cdot \mathbf{p} \cdot d_b \cdot \mathbf{t}_b \cdot \bar{L}_i \frac{\sum L_i}{L_{i \max}} \quad (5.14)$$

where L_i is the effective length of the rod and summation is extended to all the rods crossed by the crack.

V_{2F} has to be computed in the most unfavorable crack position, that is the position in which it is minimum. It can be shown that, for vertical rods, the minimum value is:

$$V_{2F} = 2 \cdot \mathbf{p} \cdot d_b \cdot \mathbf{t}_b \cdot \bar{L}_i \quad \text{if} \quad \frac{d_{net}}{2} < s < d_{net} \quad (5.15a)$$

$$V_{2F} = 2 \cdot \mathbf{p} \cdot d_b \cdot \mathbf{t}_b \cdot \bar{L}_i \cdot \frac{3 \cdot d_{net} - 4 \cdot s}{d_{net}} \quad \text{if} \quad \frac{d_{net}}{4} < s < \frac{d_{net}}{2} \quad (5.16a)$$

In the case of 45-degree rods, it is:

$$V_{2F} = 2 \cdot \mathbf{p} \cdot d_b \cdot \mathbf{t}_b \cdot \bar{L}_i \quad \text{if} \quad d_{net} < s < 2d_{net} \quad (5.15b)$$

$$V_{2F} = 2 \cdot \mathbf{p} \cdot d_b \cdot \mathbf{t}_b \cdot \bar{L}_i \cdot \frac{3 \cdot d_{net} - 2 \cdot s}{d_{net}} \quad \text{if} \quad \frac{d_{net}}{2} < s < d_{net} \quad (5.16b)$$

5.7.6. Summary of the Proposed Design Procedure. The proposed design equations for computing the shear capacity of RC beams strengthened in shear with NSM FRP rods are summarized below.

1. Compute d_{net} using (5.5);
2. Compute the FRP contribution to the shear capacity based on bond strength in the most unfavorable crack position, V_{IF} , through (5.7), (5.8) and (5.9);
3. If necessary, compute the FRP contribution to the shear capacity based on FRP maximum strain equal to $4000 \mu\epsilon$, V_{2F} , through (5.15) or (5.16);
4. Compute $V_{FRP} = \min(V_{IF}, V_{2F})$;
5. Check that (5.3) and (5.4) are satisfied.
6. Compute the shear capacity of the beam as:

$$fV_n = 0.85(V_c + V_s) + 0.70V_{FRP} \quad (5.17)$$

5.7.7. Comparison with the Experimental Results. This procedure was applied to predict the shear capacity of the tested beams. The value of \mathbf{t}_b was taken equal to 1 ksi (6.9 MPa), based on results obtained from the bond tests. Calculated and experimental values of V_c , V_s , V_{FRP} and V_n are reported in Table 5.3. V_c has been computed in two different ways, using the ACI formula (11-3) in Section 11.3.1.1:

$$V_c = 2\sqrt{f'_c} \cdot b_w \cdot d \quad (5.18) \quad \text{and using}$$

the upper limit indicated in Section 11.3.2.1:

$$V'_c = 3.5\sqrt{f'_c} \cdot b_w \cdot d \quad (5.19)$$

where f'_c is the concrete compressive strength in psi, b_w is the web width in inches and d the distance from the extreme compression fiber of the cross-section to the centroid of the longitudinal reinforcement, in inches. Expression (5.19) gives a value closer to the experimental value, so that calculated and experimental values of the shear strength can be compared focusing on the FRP contribution. ACI formula (11-5) in Section 11.3.2.1 has not been used. Given present geometry, the value of V_c it gives is very close to that given by (11-3) (Equation 5.18).

Table 5.3. Summary of Experimental and Theoretical Results

Beam Code	Experimental			
	V_c (kips)	V_s (kips)	V_{FRP} (kips)	V_n (kips)
BV	20.3	-	-	20.3
B90-7	20.3*	-	5.6	25.9
B90-5	20.3*	-	8.4	28.7
B90-5A	20.3*	-	21.5	41.8
B45-7	20.3*	-	16.9	37.2
B45-5	20.3*	-	19.7	40.0
BSV	20.3*	14.2	-	34.5
BS90-7A	20.3*	14.2**	12	46.5

Beam Code	Theoretical						
	V_c (kips)	V'_c (kips)	V_s (kips)	V_{FRP} (kips)	V_n (kips)	V'_n (kips)	fV_n *** (kips)
BV	11.3	19.9	-	-	11.3	19.9	9.6
B90-7	11.3	19.9	-	2.4	13.7	22.3	11.3
B90-5	11.3	19.9	-	7.1	18.4	27.0	14.6
B90-5A	11.3	19.9	-	16.5	27.8	36.4	21.2
B45-7	11.3	19.9	-	15.1	26.4	35.0	20.2
B45-5	11.3	19.9	-	20	31.3	39.9	23.6
BSV	11.3	19.9	11.0	-	22.3	30.9	19.0
BS90-7A	11.3	19.9	11.0	11.8	34.1	42.7	27.2

* Shear capacity of beam BV

** V_s of beam BSV

*** Note that the reduction factor 0.5 for V_c due to the absence of steel shear reinforcement has not been applied.

The contribution of the steel shear reinforcement has been computed according to Section 11.5.6.2 of the ACI code:

$$V_s = \frac{A_v f_y d}{s} \quad (5.20)$$

The following notation has been used:

$$V_n = V_c + V_s + V_{FRP} \quad (5.2)$$

$$V_n' = V_c' + V_s + V_{FRP} \quad (5.21)$$

$$\phi V_n = 0.85(V_c + V_s) + 0.70V_{FRP} \quad (5.17)$$

The experimental values of V_{FRP} are plotted versus the predicted values in Figure 5.35. The solid line represents perfect agreement between the two set of values. It can be noted that, except for one, all the plotted points fall on the left side of the line, which indicates that the proposed approach leads to a conservative estimate of the FRP contribution to the shear strength.

Experimental and predicted values of the shear capacity are reported in Figure 5.36. The calculated values of V_n' show a good agreement with the experimental shear capacity of the tested beams, the maximum error being 13.9% and the average error being 7.4%. Furthermore, all the predictions are conservative. Using (5.18) to compute the concrete contribution to the shear capacity leads to very conservative predictions. As a result, the calculated values of V_n are considerably smaller than the experimental shear strengths. Finally, the design values of the shear strength after application of the reduction factor are plotted.

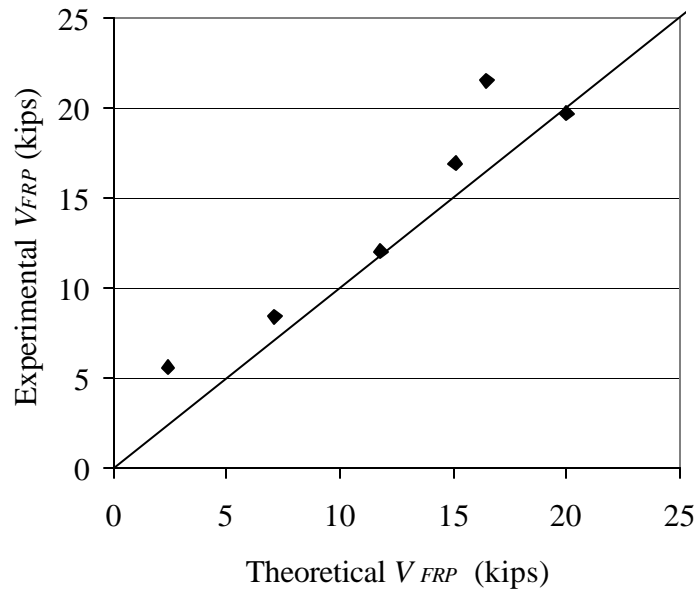


Figure 5.35. Comparison of Experimental and Theoretical V_{FRP}

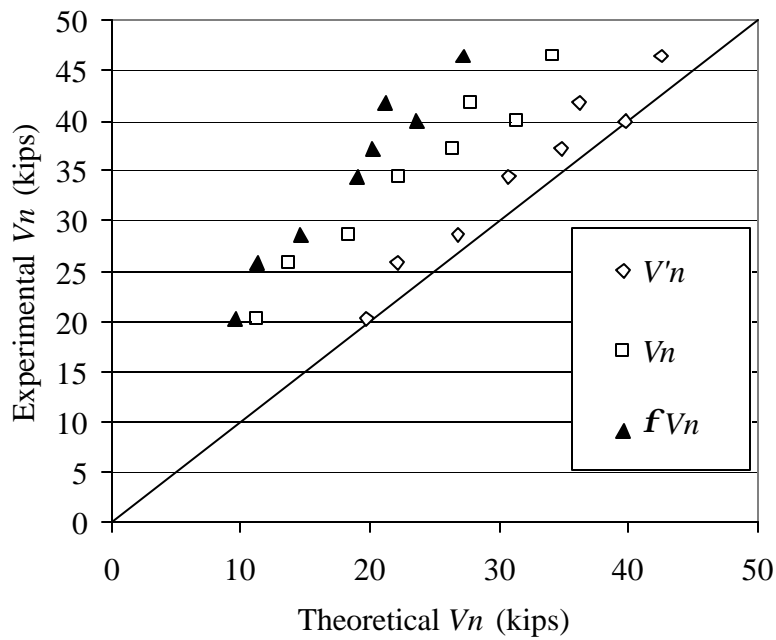


Figure 5.36. Comparison of Experimental and Theoretical V_n

5.8. CONCLUSIONS

From the experimental study presented in this section, the following conclusions can be drawn:

- the use of NSM FRP rods is an effective technique to enhance the shear capacity of RC beams. In absence of steel stirrups, an increase in capacity as high as 106% with respect to the control beam could be obtained;
- of the two beams with steel stirrups below the ACI requirements, the strengthened one showed an increase in capacity of 35% over the unstrengthened one. Therefore, it appears that the contribution of the NSM rods can be significant also in presence of internal shear reinforcement;
- one of the observed failure modes was debonding of one or more FRP rods due to splitting of the epoxy cover. Test results seem to indicate that this mechanism can be prevented by providing a larger bond length with either anchoring the NSM rods in the beam flange or using 45-degree rods at a sufficiently close spacing;
- once debonding of the rods is prevented, splitting of the concrete cover of the longitudinal reinforcement may become the controlling factor. This mechanism can be explained with the difference in configuration between internal stirrups and NSM reinforcement. Unlike internal steel stirrups, NSM rods are not able to exert any restraining action on the longitudinal reinforcement subjected to dowel forces. These forces, in conjunction with the wedging action of the deformed reinforcement, give rise to tensile stresses in the surrounding concrete which may eventually lead to cover delamination and loss of anchorage;
- the proposed design approach to compute the shear capacity of RC beams strengthened with NSM FRP rods appears to be reasonable and conservative. Further research is needed to incorporate in the design formulae the influence of all the significant variables.

6. CONCLUSIONS AND RECOMMENDATIONS FOR FURTHER RESEARCH

6.1. CONCLUSIONS

From the experimental investigation reported in this document, the following conclusions could be drawn.

Bond of NSM FRP rods to concrete:

- the bond test method for NSM rods in concrete adopted in this experimental program appears to be an efficient protocol for investigation of bond. It gives reliable and consistent data while maintaining a manageable specimen size. Furthermore, specimen details as the saw cut and the top hinge at mid-span allow to analyze the data with more accuracy. It is recommended as a possible new standard test method;
- three different failure modes were observed during the bond tests of NSM rods in concrete, namely, splitting of the epoxy cover, cracking of the concrete surrounding the groove and pull-out of the FRP rod. In some cases, combined failure modes were observed;
- the surface condition of the FRP rods influences the bond strength. Deformed rods appear to be more efficient than sandblasted rods from the standpoint of the bond performance;
- increasing the groove size, and thus the cover thickness, leads to higher bond strength when failure is controlled by splitting of the epoxy cover. Conversely, it does not have any effect when pull-out failure occurs;
- the only specimen that failed by cracking of the concrete surrounding the groove had the largest value of the ratio cover thickness to rod diameter among all the specimens with deformed rods. When failure occurs by splitting of the epoxy cover or by pull-out of the rod, the ultimate load is expected to be independent from the concrete tensile strength. However, if the groove is deep enough to cause failure occur in the concrete, the concrete tensile strength becomes a significant parameter;
- from the experimental results involving different groove sizes, the optimum groove sizes appear to be 3/4 in. and 1 in. for embedment of NSM rods No. 3 and No. 4, respectively. This result is valid for the types of bar herein investigated and is based on testing of specimens with deformed rods. The effect of the groove size for specimens with sandblasted rods having bonded lengths greater than 12 rod diameters needs to be investigated;

- the distribution of bond stresses at ultimate is not uniform, except for the case of specimens with CFRP No. 3 deformed rods. Therefore, the development length has to be calculated by solving the differential equation of bond with the local bond stress – slip relationship of the NSM rods.

Bond of NSM FRP rods to concrete masonry blocks:

- two different failure modes were observed during the bond tests of NSM rods in concrete masonry blocks, namely, splitting of the epoxy cover accompanied by concrete cracking for the specimens with GFRP deformed rods and pull-out for those with CFRP sandblasted rods;
- unlike in the case of NSM rods in concrete, a noticeable level of damage was always induced in the portion of block surrounding the groove along with splitting of the epoxy cover, due to the lower tensile strength of the concrete masonry material;
- also in this case, the distribution of bond stresses at ultimate is not uniform.

Shear strengthening of RC beams with NSM FRP rods:

- the use of NSM FRP rods is an effective technique to enhance the shear capacity of RC beams. In absence of steel stirrups, an increase in capacity as high as 106% with respect to the control beam could be obtained;
- of the two beams with steel stirrups below current ACI requirements, the strengthened one showed an increase in capacity of 35% over the unstrengthened one. Therefore, it appears that the contribution of the NSM rods can be significant also in presence of internal shear reinforcement;
- one of the observed failure modes was debonding of one or more FRP rods due to splitting of the epoxy cover. Test results seem to indicate that this mechanism can be prevented by either anchoring the NSM rods in the beam flange or using 45-degree rods at a sufficiently close spacing, which provides a larger bond length;
- once debonding of the rods was prevented, splitting of the concrete cover of the longitudinal reinforcement became the controlling factor. This mechanism appears to be critical in beams strengthened for shear with NSM FRP rods. This can be explained with the difference in configuration between internal stirrups and NSM reinforcement. Unlike internal steel stirrups, NSM rods are not able to exert any restraining action on the longitudinal reinforcement subjected to dowel forces. These forces, in conjunction with the wedging action of the deformed reinforcement, give rise to tensile stresses in the surrounding concrete which may eventually lead to failure of the beam;

- the proposed design approach to compute the shear capacity of RC beams strengthened with NSM FRP rods appears to give reasonable and conservative results, based on the limited database of experimental results available to date.

6.2. RECOMMENDATIONS FOR FURTHER RESEARCH

The overall objective of the present study was to carry out a preliminary investigation on NSM FRP rods as a structural strengthening system. Due to its novelty, extensive experimental and analytical work is needed to characterize and predict the structural behavior of RC and masonry members externally strengthened with this technique. The ultimate goal is to develop design formulae and construction specifications, since these are the means through which an experimental technology can become accepted field practice.

Experimental investigations on the flexural strengthening of full-size RC beams with NSM FRP rods have been recently conducted at the University of Missouri – Rolla. Testing of strengthened masonry walls subjected to in-plane and out-of-plane loading are also currently ongoing.

As far as the results presented in this document are concerned, slip and strain data collected from the bond testing of NSM FRP rods in concrete and masonry need to be analyzed and a suitable analytical model needs to be developed, in order to calculate the development length of the rods.

Further experimental tests and analytical investigations are needed to assess the validity of the proposed shear design approach and to incorporate in the design formulae the influence of all the significant variables.

Once structural static performance is defined, investigations should be directed towards other behavioral aspects such as performance under repeated, sustained, dynamic and thermal loads and under aggressive environments.

REFERENCES

- American Concrete Institute (1995), *Building Code Requirements for Structural Concrete (ACI 318-95) and Commentary (ACI 318R-95)*, ACI Committee 318, Detroit, MI, 369 pp.
- ASCE-ACI Committee 426 (1973), *"The Shear Strength of Reinforced Concrete Members – Chapters 1 to 4"*, Proceedings ASCE, Journal of the Structural Division, Vol. 99, No. ST6, June, pp. 1091-1187.
- Alkhrdaji, T.; Nanni, A.; Chen, G.; and Barker, M. (1999), *"Upgrading the Transportation Infrastructure: Solid RC Decks Strengthened with FRP,"* Concrete International, American Concrete Institute, Vol. 21, No. 10, October, pp. 37-41.
- Al-Zahrani, M.M. (1995), *Bond Behavior of Fiber Reinforced Plastic (FRP) Reinforcements with Concrete*, PhD. Thesis, Department of Civil and Environmental Engineering, The Pennsylvania State University, University Park, PE, pp. 263.
- Asplund, S.O. (1949), *"Strengthening Bridge Slabs with Grouted Reinforcement"*, Journal of the American Concrete Institute, Vol. 20, No. 6, January, pp. 397-406.
- Bakis, C.E.; Uppuluri, V.S.; Nanni, A.; and Boothby, T.E. (1998), *"Analysis of Bonding Mechanics of Smooth and Lugged FRP Rods Embedded in Concrete,"* Composite Science and Technology, Vol. 58, pp. 1307-1319.
- Benmokrane, B. (1998), *Standard Test Methods for FRP Rod and Sheet*, Published by Intelligent Sensing for Innovative Structures (ISIS)-Canada, University of Manitoba, Winnipeg, Canada, 61 pp.
- Cosenza, E.; Manfredi, G.; and Realfonzo, R. (1997), *"Behavior and Modeling of Bond of FRP Rebars to Concrete"*, Journal of Composites for Construction, Vol. 1, No. 2, pp. 40-51.
- Crasto, A.; Kim, R.; and Ragland, W. (1999), Private Communication.
- Dolan, C.W.; Rizkalla, S.; and Nanni, A., Editors (1999), Proceedings of the Fourth International Symposium on Fiber Reinforced Polymer Reinforcement for Reinforced Concrete Structures, American Concrete Institute SP-188, 1182 pp.
- Dye, W.K.; Bakis, C.E.; and Nanni, A. (1998), *"Accelerated Testing of Carbon FRP Tendon-Anchor Systems for Post-Stressed Concrete Applications"*, Proc. First Intl. Conf. On Durability of Composites for Construction, B. Benmokrane, and H. Rahman, Eds., 5-7 Aug., Sherbrooke, Quebec, Canada, pp. 463-473.

- Drysdale, R.G.; Hamid, A.A.; and Baker, L.R. (1994), *Masonry Structures: Behavior and Design*, Prentice-Hall, Inc., Upper Saddle River, NJ
- Eligehausen, R.; Popov, E. P.; and Bertero, V. V. (1983), *Local Bond Stress – Slip Relationships of Deformed Bars Under Generalized Excitations*, Report No. 83/23, EERC, University of California, Berkeley, CA, 162 pp.
- Focacci, F. (1999), *Armature di “FRP-Material” per il Rinforzo Attivo e Passivo del Calcestruzzo*, PhD. Thesis, School of Engineering, University of Lecce, Italy, 177 pp. (in Italian).
- Focacci, F; Nanni, A.; and Bakis, C.E. (2000), “*Local Bond-Slip Relationship for FRP Reinforcement in Concrete*”, *Journal of Composites for Construction*, Vol. 4, No. 1, pp. 1-9.
- Goto, Y. (1971), “*Cracks Formed in Concrete Around Deformed Tension Bars*”, *ACI Journal, Proceedings*, American Concrete Institute, Vol. 68, No. 4, April, pp. 244-251.
- Hartley, A.; Mullins, G.; and Sen, R. (1996), “*Repair of Concrete Masonry Block Walls using Carbon Fiber*,” *Advanced Composite Materials in Bridges and Structures*, Montreal, Quebec, pp. 795-802.
- Hogue, T.; Cornforth, R.C.; and Nanni, A. (1999), “*Myriad Convention Center Floor System Reinforcement*”, *Proceedings of the Fourth International Symposium on Fiber Reinforced Polymer Reinforcement for Reinforced Concrete Structures*, C.W. Dolan, S. Rizkalla and A. Nanni, Editors, American Concrete Institute SP-188, pp. 1145-1161.
- Japan Society of Civil Engineers (JSCE) (1997), *Recommendation for Design and Construction of Concrete Structures Using Continuous Fiber Reinforcing Materials*, Concrete Engineering Series, No. 23, 325 pp.
- Jirsa, O.J.; Lutz, L.A.; and Gergeley, P. (1979), “*Rational for Suggested Development, Splices and Standard Hook Provisions for Deformed Bars in Tension*,” *Concrete International: Design and Construction*, Vol. 1, No. 7, July, pp. 47-61.
- Khalifa, A. (1999), *Shear Performance of Reinforced Concrete Beams Strengthened with Advanced Composites*, PhD. Thesis, Department of Structural Engineering, University of Alexandria, Egypt, 155 pp.
- Khalifa, A.; Gold, W.J.; Nanni, A.; and Abdel Aziz, M. I. (1998), “*Contribution of Externally Bonded FRP to Shear Capacity of RC Flexural Members*”, *Journal of Composites for Construction*, Vol. 2, No. 4, pp. 195-202.

- Lutz, L.A. (1970), "Analysis of stress in concrete near a reinforcing bar due to bond and transverse cracking", ACI Journal, Proceedings, American Concrete Institute, Vol. 67, No. 10, October, pp. 778-787.
- Lutz, L.A. and Gergeley, P. (1967), "Mechanics of Bond and Slip of Deformed Bars in Concrete", ACI Journal, Proceedings, American Concrete Institute, Vol. 64, No. 11, November, pp. 711-721.
- MacGregor, J. C. (1997), *Reinforced Concrete – Mechanics and Design*, 3rd Edition, Prentice-Hall, Inc., Upper Saddle River, NJ, 939 pp.
- Marshall Industries Composites Inc. (1998), "*C-Bar™ Reinforcing Rods for Concrete Reinforcement*".
- Master Builders Technologies Inc. (1996), "*Concresive® Paste LPL – Long Pot Life Concrete Bonding Adhesive*".
- Miller, B. (1999), *Bond Between Carbon Fiber Reinforced Polymer Sheets and Concrete*, MSc. Thesis, Department of Civil Engineering, University of Missouri – Rolla, Rolla, MO, pp. 138.
- Nanni, A., Ed. (1993), *Fiber-Reinforced-Plastic (FRP) Reinforcement for Concrete Structures: Properties and Applications*, Developments in Civil Engineering, Vol. 42, Elsevier, Amsterdam, The Netherlands, pp. 450.
- Nanni, A. (1998), Private Communication.
- Orangun, C.; Jirsa, J.O.; and Breen, J.E. (1977), "A Reevaluation of Test Data on Development Length and Splices," ACI Journal, Proceedings, American Concrete Institute, Vol. 74, No. 3, March, pp. 114-122.
- Schwegler, G. and Kelterborn P. (1996), "*Earthquake Resistance of Masonry Structures Strengthened with Fiber Composites*," Eleventh World Conference on Earthquake Engineering, Acapulco, Mexico.
- Tepfers, R. (1973), *A Theory of Bond Applied to Overlapped Tensile Reinforcement Splices for Deformed Bars*, Publication 73:2, Division of Concrete Structures, Chalmers University of Technology, Gothenburg, Sweden, 328 pp.
- Tepfers, R. (1979), "*Cracking of Concrete Cover Along Anchored Deformed Reinforcing Bars*", Magazine of Concrete Research, Vol. 31, No. 106, Cement and Concrete Association, Wexham Springs, Slough, England, pp. 3-12.
- Tepfers, R. (1998), *Bond Between FRP-Bars and Concrete*, Publication 98:3, Division of Building Technology, Chalmers University of Technology, Gothenburg, Sweden, 16 pp.

- Thomas, J. (1998), ‘*FRP Strengthening – Experimental or Mainstream Technology?*’ Concrete International, American Concrete Institute, Vol. 20, No. 6, June, pp. 57-58.
- Tighiouart, B.; Benmokrane, B.; and Gao, D. (1998), ‘*Investigation of the Bond of Fiber Reinforced Polymer (FRP) Rebars in Concrete,*’ Proceedings of the Second International Conference on Composites in Infrastructure (ICCI-98), Tucson, AZ, pp. 102-112.
- Tinazzi D., Modena C., Nanni A. (2000). ‘*Strengthening of Masonry Assemblages with Fiber Reinforced Polymer Rods and Laminates*’. Advancing with Composites 2000, Milan, Italy.
- TMS (1994), ‘*Performance of Masonry Structures in the Northridge California Earthquake of January 17, 1994,*’ The Masonry Society.
- Tumialan, G.; Tinazzi, D.; Myers, J.; and Nanni, A. (1999), *Field Evaluation of Masonry Walls Strengthened With FRP Composites at the Malcolm Bliss Hospital*, Report CIES 99-8, Center for Infrastructure Engineering Studies, University of Missouri-Rolla, Rolla, MO.
- Velazquez J.I. (1998), *Out-of-Plane Cyclic Behavior of URM Walls Retrofitted with Fiber Composites*, Ph.D. Thesis, Department of Civil Engineering and Engineering Mechanics, The University of Arizona, AZ.
- Warren, G.E. (1998), *Waterfront Repair and Upgrade, Advanced Technology Demonstration Site No. 2: Pier 12, NAVSTA San Diego*, Site Specific Report SSR-2419-SHR, Naval Facilities Engineering Service Center, Port Hueneme, CA.
- Yan, X.; Miller, B.; Nanni, A.; and Bakis, C.E. (1999), ‘*Characterization of CFRP Bars Used as Near-Surface Mounted Reinforcement*’, Proceedings 8th International Structural Faults and Repair Conference, M.C. Forde, Ed., Engineering Technics Press, Edinburgh, Scotland, 1999, 10 pp., CD-ROM version.